

AD656466

4942.5-E

AN INTERFEROMETRIC STUDY OF THE EFFECTS OF CORONA DISCHARGE
ON THE TEMPERATURE PROFILES ON A FLAT, UNIFORM
TEMPERATURE PLATE IN FORCED CONVECTION

Richard D. Godfrey

Henry R. Velkoff

Technical Report

Contract No. DA-31-124-ARO-D-246

U. S. Army Research Office - Durham
Box CM, Duke Station
Durham, North Carolina 27706

Distribution of this document is unlimited.

The findings in this report are not to be construed as an official
Department of the Army position, unless so designated by other
authorized documents.

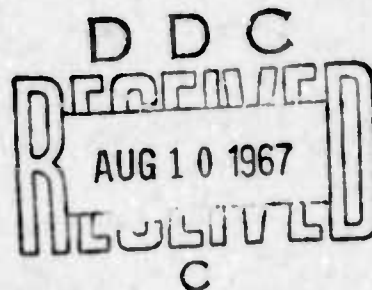
June, 1967

The Ohio State University Research Foundation
Columbus, Ohio 43212

RECEIVED

AUG 21 1967

CFSTI



Disclaimer

The findings in this report are not to be construed as an official Department of the Army position.

The citation of trade names and names of manufacturers in this report is not to be construed as official Government endorsement or approval of commercial products or services rendered.

Distribution of this document is unlimited.

ACCESSION for	
CFSTI	WHITE SECTION <input checked="" type="checkbox"/>
DDC	BUFF SECTION <input type="checkbox"/>
UNANNOUNCED	<input type="checkbox"/>
JUSTIFICATION	
BY <i>BM</i>	
DISTRIBUTION/AVAILABILITY CODES	
DIST.	AVAIL. and/or SPECIAL
1	

RF Project.....1864

Report No.....4

TECHNICAL

REPORT

By

THE OHIO STATE UNIVERSITY
RESEARCH FOUNDATION

1314 KINNAR RD.
COLUMBUS, OHIO 43212

To..... U. S. Army Research Office - Durham
Box C.M., Duke Station
Durham, North Carolina 27706
Contract No. DA-31-124-ARO-D-246
Project Nos. 2001050B700, 1D12, 40A142

On..... AN INTERFEROMETRIC STUDY OF THE EFFECTS OF CORONA
DISCHARGE ON THE TEMPERATURE PROFILES ON A FLAT,
UNIFORM TEMPERATURE PLATE IN FORCED CONVECTION

Submitted by..... Richard D. Godfrey and Henry R. Velkoff
Department of Mechanical Engineering

Date..... June 1967

FOREWORD

This report presents essentially the same material as the Master's Thesis, "An Interferometric Study of the Effects of Corona Discharge on the Temperature Profiles on a Flat, Uniform Temperature Plate in Forced Convection" by R. D. Godfrey. The thesis was presented in partial fulfillment of the requirements for the Master of Science degree in Mechanical Engineering at The Ohio State University.

The junior author would like to express his thanks to Dr. Velkoff for his advice and guidance throughout the research program. Thanks are also extended to Mr. E. R. Pejack for his aid and advice and to Mr. I. Anderson for his aid in collecting data. Finally the financial support given by the United States Army Research Office - Durham, which allowed this research to be undertaken is gratefully acknowledged.

ABSTRACT

The purpose of this thesis was to study the effects of corona discharge on flow past a flat plate at zero incidence. In a previous exploratory investigation into the effects of ionization on the gas in channel flow, interesting results were observed. Pressure drops and heat transfer coefficients were found to double. The velocity profile was distorted.

In an attempt to explain the phenomenon, Velkoff hypothesized an induced electric field component in opposition to the flow. An analytical solution for laminar flow with a uniform charge density in the boundary layer was developed by extending the Rossow solution for MHD flows. The corona effect was predicted to retard the flow and thicken the boundary layer.

An experimental program was initiated to study this phenomenon by observing changes in the temperature profiles on a flat, uniform temperature plate in forced convection with a Mach-Zender interferometer. A series of tests were run with a constant plate to ambient temperature difference but different free stream velocities and corona currents. At a 62.5 foot per second free stream velocity, a 1000 μ ampere corona current did not effect the flow. At lower velocities, the effects observed were opposite to those predicted. It was found that the boundary layer was turbulent at the 62.5 foot per second test. Also it was noted that

5.9 foot per second test with corona discharge was similar to the 62.5 foot per second test. The body force hypothesized by Velkoff does not appear to describe the corona effect. A possible mechanism that would account for the observed result is that the corona discharge induces an instability in the flow.

CONTENTS

	Page
ACKNOWLEDGEMENT	11
ABSTRACT	111
CONTENTS	v
LIST OF ILLUSTRATIONS	vi
LIST OF TABLES	x
NOMENCLATURE	xi
INTRODUCTION	1
THEORETICAL ANALYSIS	3
TEST SET-UP	14
TEST PROCEDURE	28
EVALUATION OF INTERFEROGRAMS	31
DISCUSSION OF RESULTS	83
CONCLUSIONS	93
REFERENCES	94
APPENDIX I. TABULATION OF SOLUTION FROM ROSSOW.	96
APPENDIX II. ADJUSTMENT OF THE MACH-ZENDER INTERFEROMETER.	99
APPENDIX III. METHOD USED TO ANALYZE INTERFERENCE DATA.	105
APPENDIX IV. REFRACTION ERROR.	110

ILLUSTRATIONS

Figure Number	Title	Page
1	Sketch of boundary layer on a flat plate at zero incidence under the action of a transverse electric field.	4
2	Velocity distribution on a flat plate for various values of mz .	11
3	Boundary layer thickness on a flat plate at zero incidence for various values of mz .	12
4	The test section.	15
5	The test section.	16
6	The test section.	17
7	The test set-up outside of the building.	19
8	The heated plate.	22
9	Instrumentation and power supply.	23
10	The lower beam.	24
11	The upper beam.	24
12	The test set-up.	26
13	Reference photos.	29
14	The gaertner comparator.	32
15	Interferometer pictures of free convection heat transfer on a vertical flat plate.	34

ILLUSTRATIONS (Continued)

Figure Number	Title	Page
16	Experimental points for the free convection test plotted against Pohlhausen's solution.	35
17	Schematic diagram of the light path through boundary layer.	38
18	Interference photos taken at two different object planes.	40
19	Pitot-static pressure profile at the test site (P2).	41
20	Velocity calibration curve.	44
21	Electric flux lines of wire and ground.	47
22	Schematic of the temperature profile near the surface of the plate.	50
23	A non-dimensional plot showing the effect of corona discharge at various free stream velocities.	52
24	Effects of corona discharge on the temperature profile on a flat plate in forced convection.	53
25	Effects of corona discharge on the temperature profile 7 inches from the leading edge.	54

ILLUSTRATIONS (Continued)

Figure Number	Title	Page
26	Effects of corona discharge on the temperature profile 8 inches from the leading edge.	55
27	Same as 24.	56
28	Same as 25.	58
29	Same as 26.	59
30	Same as 24.	60
31	Same as 25.	62
32	Same as 26.	63
33	Same as 24.	64
34	Same as 25.	66
35	Same as 26.	67
36	Same as 24.	68
37	Same as 25.	70
38	Same as 26.	71
39	Same as 24.	72
40	Same as 25.	73
41	Same as 26.	74
42	Temperature profiles for various values of m_z .	75
43	Same as 42.	76
44	Same as 42.	77
45	Same as 42.	78

ILLUSTRATIONS (Continued)

Figure Number	Title	Page
46	Same as 42.	79
47	Same as 42.	80
48	Same as 42.	81
49	Same as 42.	82
50	Temperature profiles for different amounts of corona current.	86
51	Same as 50.	87
52	Experimental temperature profiles plotted against the Blasius solution.	88
53	Same as 52.	89
54	Temperature profiles.	90
55	Experimental points for the test run at 5.9 feet per second free stream velocity plotted against the Pohlhausen solution for free convection.	91
56	Schematic of interferometer optical system.	101
57	Schematic illustrating method used to analyze interference data.	106

TABLES

Table Number	Title	Page
1	Values of $\frac{n}{y}$ for various tests and positions.	46
2	Values of mz for various test conditions.	49

NOMENCLATURE

Symbol	Definition	Units*
A	Surface area of plate under wire grid	L^2
C	General dimensional constant	variable
D	Twice h^*	L
E	Electric field strength	ML/T^2C
F	Fraction of distance across plate	1
F_e	Induced electric force	ML/TL^3
H_0	Magnetic field strength	M/TC
I	Current	C/T
J	Current flux	C/TL^2
K^+	Ion mobility	TC/M
L	Spacing between wires across plate	L
N	Number of wavelengths	1
N_u	Nusselt's number	1
N_{Re}	Charge number	1
P	Pressure	M/T^2L
R	Radius of grid wires	L
R_e	Reynold's number	1
T	Temperature	Θ
V	Grid voltage	ML^2/T^2C
V	Non-dimensional velocity perpendicular to plate	1

* System of units used mass (M), length (L), time (T), Temperature (Θ), and charge (C).

NOMENCLATURE (Continued)

Symbol	Definition	Units
W	Non-dimensional velocity in direction of flow	1
Y	Non-dimensional distance above plate	1
Z	Non-dimensional distance along plate	1
c_p	Specific heat at constant pressure	$L^2/T^2\theta$
f	Denotes a function	
g	Gravitational constant	L/T^2
h	Local film heat transfer coefficient	$M/T^3\theta$
h^*	Height of wire above plate	L
k	Thermal conductivity	$ML/T^3\theta$
l	Characteristic length	L
m	$\frac{\alpha}{u_{\infty}}$	$1/L$
m_z	Charge number x 1/Reynold's number	1
n	Index of refraction	1
u	Velocity component	L/T
v	Velocity perpendicular to plate	L/T
w	Velocity along plate	L/T
x	Coordinate direction	L
y	Coordinate direction perpendicular to plate	L
z	Coordinate direction along plate	L
ψ	Stream function	L^2/T
α	$\frac{p_c}{QK^+}$	$1/T$

NOMENCLATURE (Continued)

Symbol	Definition	Units
β	Coefficient of expansion	$1/\theta$
β^*	$\frac{\epsilon \lambda}{L(n-1)}$	1
δ	Boundary layer thickness	L
δ'	Intersection of subtangent with distance coordinate	L
ϵ	Permittivity	$C^2 T^2 / ML^3$
η	Transform	
θ	Angle	1
λ	Wavelength	L
μ	Viscosity	M/LT
μ'	Permeability (magnetic)	ML/C^2
ν	Kinematic viscosity	L^2/T
ρ	Density	M/L^3
ρ_c	Charge density	C/L^3
ρ_l	Charge density per length	C/L
σ	Electrical conductivity	ML^2/TC^2
γ	Thickness of glass	L
ξ	Number of fringe shifts	1

NOMENCLATURE (Continued)

Subscripts

Symbol	Definition
D	Drift
Q	Focal plane
e	Exit
g	Glass
i	Initial
o	At outer edge
r	Refractive
w	Wall
IND	Induced
$\{max$	Maximum free convective
δ	At edge of boundary layer
∞	Ambient
0, 1, 2, ...	Indexing subscript

INTRODUCTION

In a previous exploratory investigation into the effects of ionization on the gas flow in a channel, interesting results were observed. Complete details of that investigation may be found in Reference 1. Here we shall only briefly describe these observations.

Air was passed through a $1\frac{1}{4}$ -inch-diameter pipe in which a 0.004-inch-diameter wire was located concentrically. A high voltage applied to the wire gave rise to corona discharge which provided ions in the air stream. Under the action of the field, pressure drops were observed to be doubled, velocity profile distorted and heat transfer doubled. Similar phenomenon was also observed in a $5/8$ inch x 5 inch x 12 foot long rectangular channel in which ten parallel thin wires were located longitudinally on the center plane of the channel.

In an attempt to explain the nature of the phenomenon, a hypothesis was put forth by Velkoff in Reference 2. According to this hypothesis, an electric field component in the direction opposite to the flow is induced, giving rise to a retarding electrostatic body force. The induced field was found to be

$$E_{IND} = -\frac{u}{K^*}$$

where u is the flow velocity and K^* is the ion mobility in the gas under consideration. Application of this hypothesis

to channel flows was carried out in great detail in Reference 2. The close agreement of theoretical values predicted by the hypothesis with test data aroused interest in extending the investigation to external flows.

An analytical solution for laminar flow with a uniform charge density in the boundary layer was developed by extending the Rossow solution for MHD flows. The corona effect was predicted to retard the flow and thicken the boundary layer.

An experimental program was initiated to study this phenomenon by observing changes in the temperature profiles on a flat, uniform temperature plate in forced convection with a Mach-Zender interferometer. This technique is applicable because the flow conditions satisfy Reynold's analogy. Thus the shape of the hydrodynamic, and thermal boundary layers are identical. A series of tests were run with a constant plate to ambient temperature difference but different free stream velocities and corona currents.

THEORETICAL ANALYSIS

In this section the effect of a transverse electric field on laminar boundary layer over a flat plate are investigated analytically.* The geometrical configuration of the problem is shown in Figure 1. Let the yz-plane be taken as the plane of the boundary layer flow with axis of z along, and that of y perpendicular to the plane wall. If ρ denotes the density and μ the viscosity of the fluid, the boundary layer equation for incompressible flow in the absence of an external electric field is (Reference 4).

$$v \frac{\partial \omega}{\partial y} + \omega \frac{\partial \omega}{\partial z} = \frac{\mu}{\rho} \frac{\partial^2 \omega}{\partial y^2} \quad (1)$$

Now suppose the fluid is positively charged through the action of corona discharge or the injection of positive ions from external sources. The charge density in fluid under the action of a transverse electric field (E_y) is ρ_c . By the hypothesis postulated by Velkoff, an electric field E_x opposing the flow is induced and is given by

$$E_x = - \frac{\omega}{K^+} \quad (2)$$

Thus the contribution of the transverse electric field to fluid flow is in the form of a retarding electrostatic

* This section follows the derivation of Reference 3.

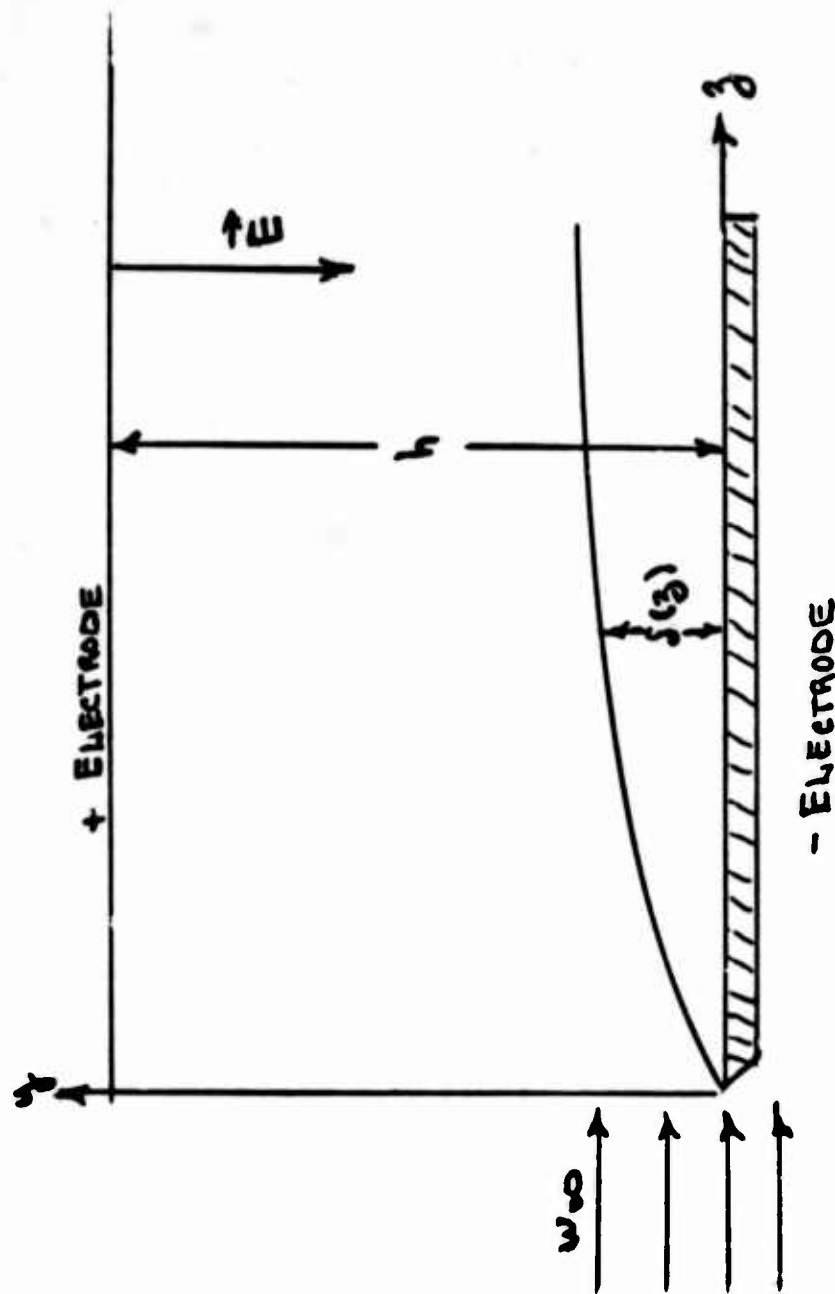


Fig. 1. Sketch of boundary layer on a flat plate at zero incidence under the action of a transverse electric field.

force. This force is found to be

$$F_e = \rho_c E_x = -\rho_c \frac{w}{k^+} \quad (3)$$

Incorporating this force in the boundary layer equation (1), we obtain a modified boundary layer equation for the case under consideration.

$$v \frac{\partial w}{\partial y} + w \frac{\partial w}{\partial z} = \frac{\mu}{\rho} \frac{\partial^2 w}{\partial y^2} - \frac{\rho_c}{\rho} \frac{w}{k^+} \quad (4)$$

This equation together with the continuity equation

$$\frac{\partial v}{\partial y} + \frac{\partial w}{\partial z} = 0$$

describes the boundary layer flow over a flat plate under the action of a transverse electric field.

The charge density, ρ_c , is related to the distribution of electric field through the electrostatic equation

$$\nabla \cdot \vec{E} = \frac{\rho_c}{\epsilon}$$

and is in general, a function of position. To obtain a first approximation of what effects the additional term, $-\frac{\rho_c}{\rho} \frac{w}{k^+}$, will have on the boundary layer, let us simplify the problem by assuming that the charge density is constant.

Under this assumption, equation (4) can be rewritten as

$$v \frac{\partial \omega}{\partial y} + w \frac{\partial \omega}{\partial z} + \alpha \omega = \gamma \frac{\partial^2 \omega}{\partial y^2} \quad (5)$$

where $\alpha = \frac{\rho_c}{\rho k}$ is a constant and $\gamma = \frac{\mu}{\rho}$ is kinematic viscosity of the fluid.

The form of equation (5) is similar to an equation obtained for the flow of an electrically conducting fluid over a flat plate in the presence of a transverse magnetic field in magnetohydrodynamic boundary layer flows. The equation, as was derived by Rossow (Reference 5), is

$$v \frac{\partial \omega}{\partial y} + w \frac{\partial \omega}{\partial z} + \frac{\sigma \mu'^2}{\rho} H_0^2 \omega = \gamma \frac{\partial^2 \omega}{\partial y^2} \quad (6)$$

where σ = electrical conductivity of the fluid

μ' = permeability of the fluid

and H_0 = externally applied constant magnetic field.

By comparison, we see that the constant $\frac{\rho_c}{k}$, corresponds to $\sigma \mu'^2 H_0^2$ in MHD case.

Equation (6) was first solved by Rossow. He developed an approximate solution. Following Rossow, equation (5) is solved as follows.

Let us introduce the transformation

$$\eta = y \sqrt{\frac{\omega_\infty}{\gamma z}}$$

and define the stream function as

$$\Psi = \sqrt{\omega_{\infty} \delta_3} \left[f_0 + \sqrt{m_3} f_1 + m_3 f_2 + (m_3)^{3/2} f_3 + (m_3)^2 f_4 + \dots \right]$$

where ω_{∞} is the upstream velocity, $m = \frac{\alpha}{\omega_{\infty}} = \frac{\rho c}{\rho K \omega_{\infty}}$ and $f_0, f_1, f_2, f_3, f_4, \dots$ are functions of η only. From the definition of stream function, i.e. $\omega = \frac{\partial \Psi}{\partial y}$ and $v = -\frac{\partial \Psi}{\partial z}$, $v, \omega, \frac{\partial \omega}{\partial y}$ and $\frac{\partial^2 \omega}{\partial y^2}$ can all be expressed in terms of f 's and η . This enables equation (5) to be expressed in powers of m_3 . Equating the coefficients of equal powers of m_3 on both sides of the equation, a set of ordinary differential equations for the f 's are obtained:

$$2 f_0''' = -f_0'' f_0 \quad (7)$$

$$2 f_1''' = f_0' f_1' - f_0 f_1'' - 2 f_1 f_0'' \quad (8)$$

$$2 f_2''' = 2 f_0 f_2' + f_1' f_1' - f_0 f_2'' - f_1 f_1'' - 3 f_2 f_0'' + 2 f_0' \quad (9)$$

$$2 f_3''' = 2 f_0' f_3' + 3 f_2' f_1' - f_0 f_3'' - 2 f_1 f_2'' - 3 f_2 f_1'' - 4 f_3 f_0'' + 2 f_1 \quad (10)$$

$$2 f_4''' = 4 f_0' f_4' + 3 f_1' f_3' + 2 f_2' f_2' + f_3' f_1' - f_0' f_4'' - 2 f_1 f_3'' - 3 f_2 f_2'' - 4 f_3 f_1'' - 5 f_4 f_0'' + 2 f_2' \quad (11)$$

The boundary conditions, $v = \omega = 0$ At $y = 0$ and $v = \frac{\partial \omega}{\partial y} = 0$ At $y = 0$ when written in terms of f 's and η , assume the form

$$f_0 = f_1 = f_2 = f_3 = f_4 = \dots = 0 \quad \text{at } \eta = 0$$

$$f_0' = f_1' = f_2' = f_3' = f_4' = \dots = 0 \quad \text{at } \eta = 0$$

$$f_0' = 1, \quad f_2' = -1 \quad \text{at } \eta = \infty$$

$$f_1' = f_3' = f_4' = f_5' = \dots = 0 \quad \text{at } \eta = \infty$$

From the boundary conditions and equations (8) and (10), f_1 and f_3 can be taken to be zero throughout the flow field. Equations (9) and (11) then become

$$f_2''' = f_0' f_2' - \frac{1}{2} f_0 f_2'' - \frac{3}{2} f_0 f_0'' + f_0' \quad (12)$$

$$f_4''' = 2 f_0' f_4' + f_2' f_2' - \frac{1}{2} f_0 f_4'' - \frac{3}{2} f_2 f_2'' - \frac{5}{2} f_4 f_0'' + f_2' \quad (13)$$

Equation (7) is the Blasius equation and equation (12) was solved numerically using Runge Kutta method. The solutions were tabulated in Reference 5 and are reproduced in Appendix 1.

It should be noted that in the above analysis m_3 plays the role of a determining factor. To investigate its physical significance, let us non-dimensionalize equation (5) by introducing the following dimensionless variables

$$Z = \frac{z}{l} \quad ; \quad Y = \sqrt{Re} \frac{y}{l}$$

$$V = \sqrt{Re} \frac{u}{u_\infty} \quad ; \quad W = \frac{w}{u_\infty}$$

where l is a characteristic length and $Re = \frac{u_\infty l}{\nu}$ is the Reynolds number. In terms of these non-dimensional variables equation (5) becomes

$$V \frac{JW}{JY} + W \frac{JW}{JZ} = \frac{J^2 W}{JY^2} - \frac{\rho c l}{\rho K u_\infty} W \quad (14)$$

Since all other quantities in the above equation are non-dimensional, the quantity $\frac{\rho_c l}{\rho K^* \omega_\infty}$ must also be non-dimensional and can be considered as the products of two non-dimensional parameters.

$$\frac{\rho_c l}{\rho K \omega_\infty} = \frac{\rho_c l^2}{\mu K} \cdot \frac{\mu}{\rho \omega_\infty l}$$

We readily recognize that $\frac{\rho \omega_\infty l}{\mu}$ is the Reynolds number. It is obvious that $\frac{\rho_c l^2}{\mu K}$ is a new non-dimensional parameter and is called the charge number, $N_{\rho c}$ (Reference 2). Now,

$$m_3 = \frac{\alpha}{\omega_\infty} z = \frac{\rho_c z}{\rho K^* \omega_\infty} = \frac{\rho_c z^2}{K^* \mu} \cdot \frac{\mu}{\rho \omega_\infty z}$$

If we let

$$Re_3 = \frac{\rho \omega_\infty z}{\mu} \quad \text{AND} \quad N_{\rho c 3} = \frac{\rho_c z^2}{\mu K^*}$$

m_3 is just the product of Re_3^{-1} and $N_{\rho c 3}$. Further analysis (Reference 2) indicates that the charge number is physically the ratio of the electrostatic force to the viscous force. Meanwhile the Reynolds number, Re , is known to represent the ratio of the inertia force to the viscous force. Thus, m_3 measures the ratio of the electrostatic force to the inertia force.

To the first approximations, the velocity distributions is given by

$$w = w_\infty (f_0' + m_3 f_2') \quad (15)$$

Divided through by w_0 , the free stream velocity (i.e.) the velocity at the edge of the boundary layer on both sides of the equation, equation (15) becomes

$$\frac{w}{w_0} = \frac{w_\infty}{w_0} (f_0' + m_3 f_2')$$

In Figure 2, $\frac{w}{w_0}$ is plotted against η for several values of m_3 . The figure indicates that increase in m_3 tends to retard the flow. It is predicted that further increase in m_3 will decrease the velocity gradient at the wall; $\frac{dw}{d\eta}|_{\eta=0}$. When $\frac{dw}{d\eta}|_{\eta=0}$ reaches zero, separation will occur. It may be concluded that if the foregoing hypothesis and analysis is valid, an increase in electric field will finally cause separation.

If it is desired to define the boundary layer thickness as that distance for which

$$\frac{w}{w_0} = 0.99, \text{ then}$$

$$\frac{\delta}{z} = \frac{\eta_\delta}{\sqrt{Re_z}} \quad \text{where } \eta_\delta \text{ is the value of } \eta \text{ evaluated at } y = \delta$$

In Figure 3, the ratio $\frac{\delta}{z}$ is plotted against Re_z . For a given value of z , the boundary layer thickness, δ , increases with increase in m . In other words, the field tends to thicken the boundary layer. This can also be seen from Figure 2.

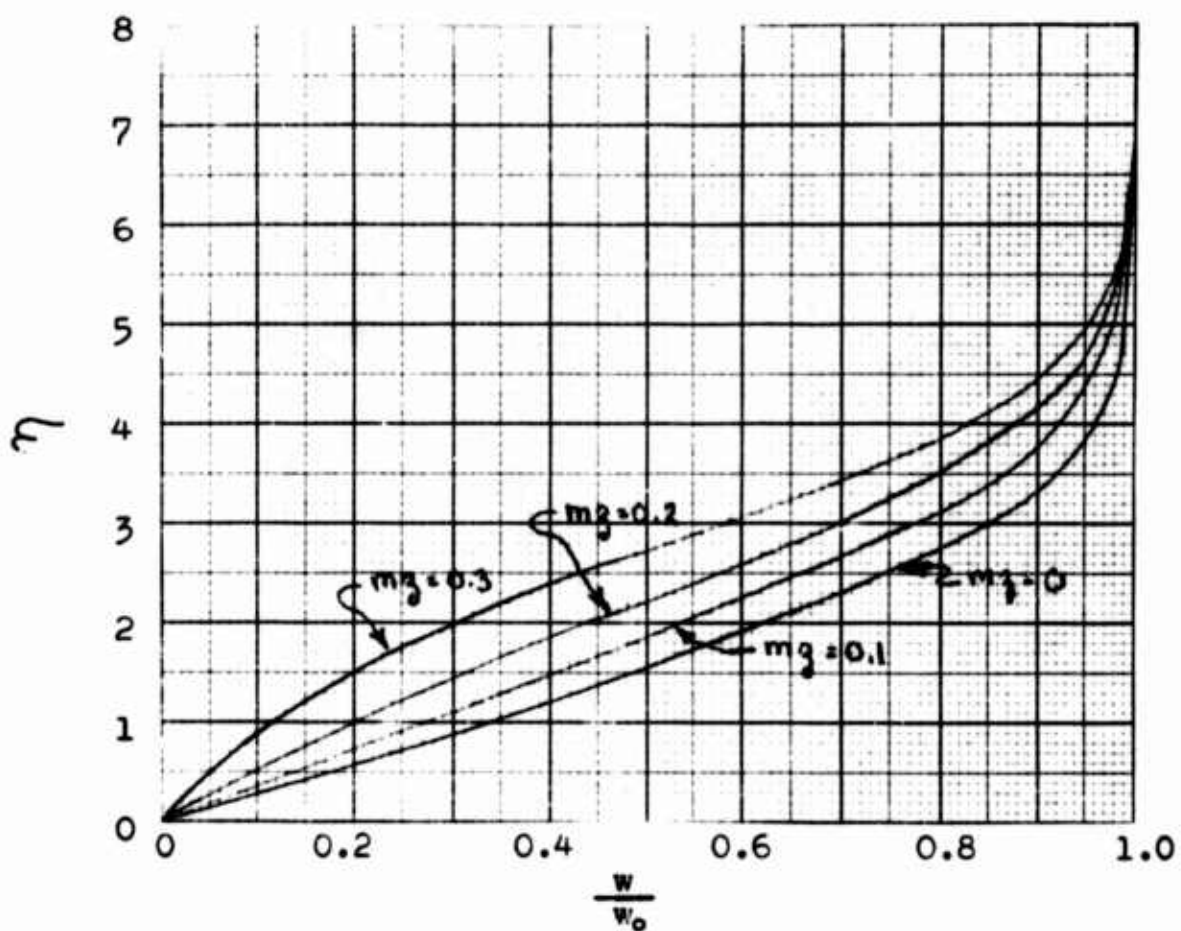


Fig. 2. Velocity distribution on a flat plate for various values of m_2 .

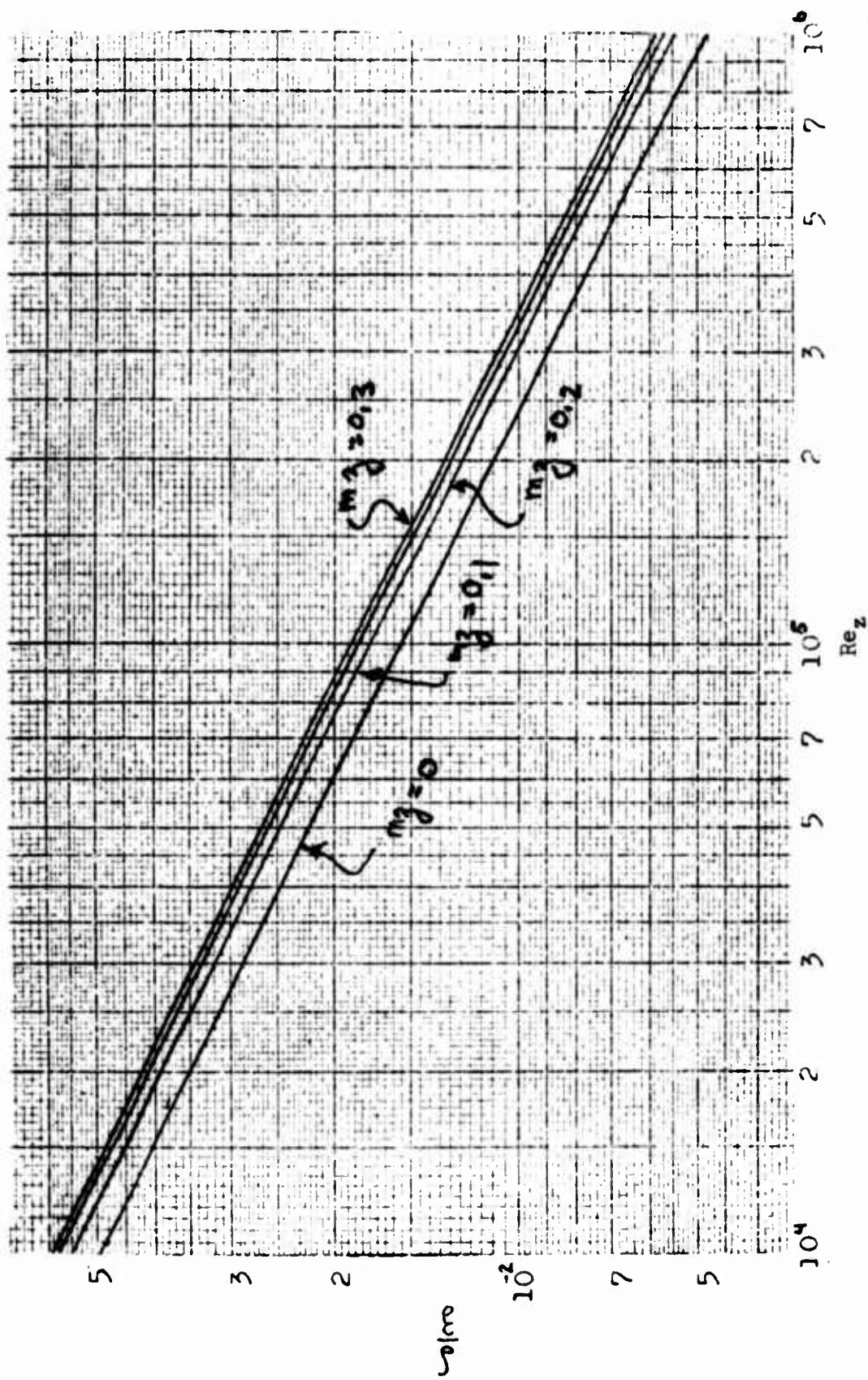


Fig. 3. Boundary layer thickness on a flat plate at zero incidence for various values of m_2 .

If Reynold's analogy is applicable to the flow conditions under consideration a flat, uniform surface temperature plate can be utilized so that the flow can be measured without disturbance with a Mach-Zender interferometer. The conditions necessary for application of Reynolds analogy are that the buoyant forces and frictional heating effects be neglectable, (Reference 4). In addition the fluid properties ρ , μ , R and c_p must be constant and the dimensionless group $\frac{\mu g c_p}{R}$ Prandtl's number must equal unity. For these conditions, the velocity component (w) and the temperature (T) become identical in the momentum (16) and energy (17) equations respectively.

$$\rho \left(w \frac{\partial w}{\partial z} + v \frac{\partial w}{\partial y} \right) = \mu \frac{\partial^2 w}{\partial y^2} + \rho g w \beta (T - T_\infty) \quad (16)$$

$$\rho g c_p \left(w \frac{\partial T}{\partial z} + v \frac{\partial T}{\partial y} \right) = R \frac{\partial^2 T}{\partial y^2} + \mu \left(\frac{\partial w}{\partial y} \right)^2 \quad (17)$$

Their solution for $\frac{w}{w_\infty}$ and $\frac{T - T_w}{T_\infty - T_w}$ are identical in algebraic form. For air Prandtl's number is approximately 0.73 and nearly constant for up to 100°F above ambient. This is sufficiently close to unity that the analogy holds making it possible to infer the velocity by measuring the temperature. The results of an experimental investigation based upon this technique are reported in the following sections.

TEST SET-UP

The objective of the test was to measure with the Mach-Zender interferometer variations in the boundary layer on a heated flat plate due to positive corona discharge at various free stream velocities. To accomplish these objectives the set-up shown in Figure 4 was designed.

The flow channel was an open loop, drawing supply air from the building and discharging it from the blowers outside the building. Air entered the flow channel just below the test section and moved upward through a set of 14x18 mesh screens spaced 1 inch apart. A vertical test section was chosen so that free convective effects acted in the same direction as the free stream. A settling chamber, (Figure 4-A) 24"x30" in cross section and 4" deep followed the screens and preceded a convergent nozzle. The nozzle, (Figure 4-B), was designed to give a high rate of change in area at its entrance and a low rate at its exit. The curves chosen were quadrants of ellipses with minor diameters of 20" and 16" for long and short dimension respectively. The major diameter for both was 24". The nozzle was made of 22 gauge sheet metal. Joints were lapped and welded exteriorly. Interior intersections were filed smooth.

The nozzle was rigidly joined to the test section, (Figures 5 and 6), which was 8"x10" in cross section and 22" long. Ports, 8" in diameter (Figure 5-A), for the optical flats were located 12" downstream on the 8" wall.

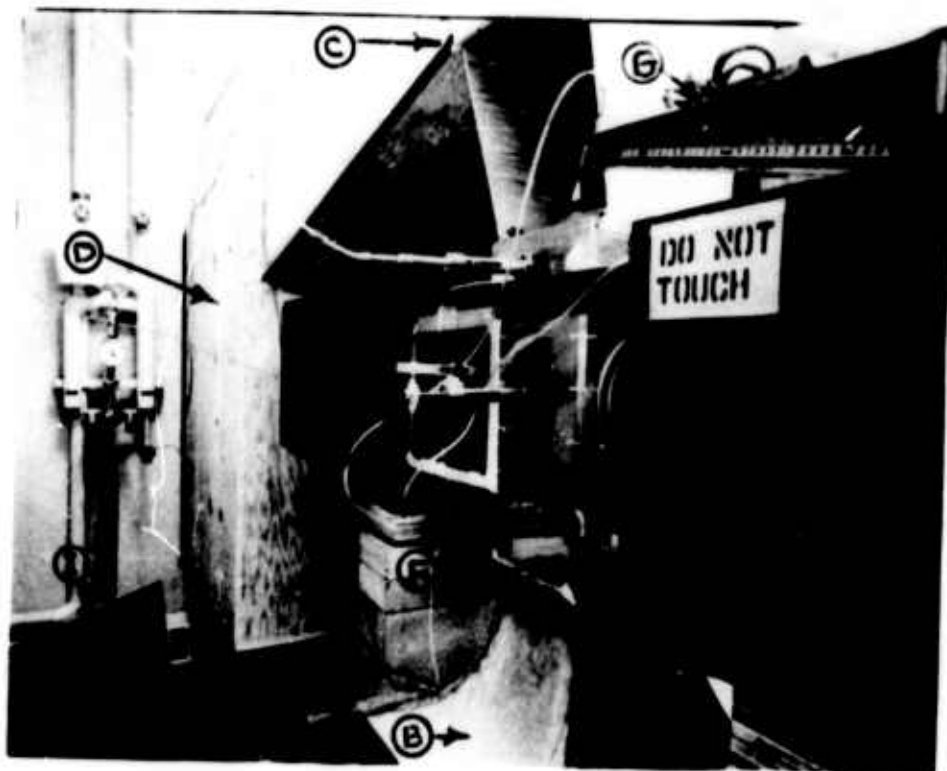


Fig. 4. The test section. A.) settling chamber, B.) nozzle, C.) hinged diffuser walls, D.) acoustic isolation chamber, E.) nylon cord, F.) pitot-static tube, G.) inclined manometer, H.) free stream thermocouple, I.) damping screen.

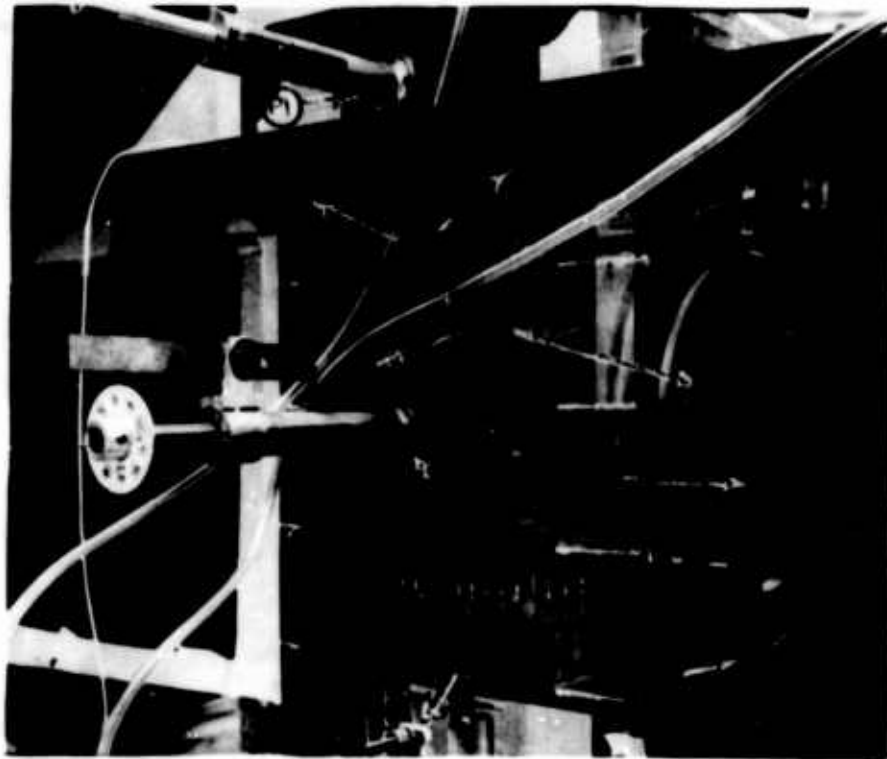


Fig. 5. The test section. A.) optical flats, B.) plate supports, C.) vertical axis adjustment, D.) reference length "T", P1 P2 and P3.) pressure tap locations.

Provisions were made in 1" thick plexiglass walls to support (Figure 5-B) the heated plate above and below the optical flats. The nozzle-test section unit was supported by an angle iron frame tied into the interferometer. Four bolts span the 1/8" space between the test section and frame. Adjusting of these bolts (Figure 5-C) allowed the plate to be made parallel to the light beam by rotation of the test section about its vertical axis.

Air leaving the test section entered a diffuser. This connection was made flexible to mechanically isolate the test section from the rest of the ducting. The walls of the diffuser were hinged to the turning box above to allow easy access to the test section, (Figure 4-C). Beyond the turning vanes, the channel diverged to a 22"x30" cross section and emptied into a "S" turn acoustical isolation chamber, (Figure 4-D). The 1/2" thick plywood walls of the acoustic isolation chamber were lined with Owens Corning fiber glass board to reduce noise from the blowers. Air was drawn from the lower chamber through two nozzles, (Figure 7-A), into 8" diameter flexible hoses, (Figure 7-B), that linked the acoustical isolation chamber to two PW-14 Hartzell radial blade blowers, (Figure 7-C).

The blowers were mounted on a cart so they could be easily moved into position outside the window when needed. The blowers were powered by Lincoln Electric 5 H.P. motors with a synchronous speed of 3600 RPM. The pressure across

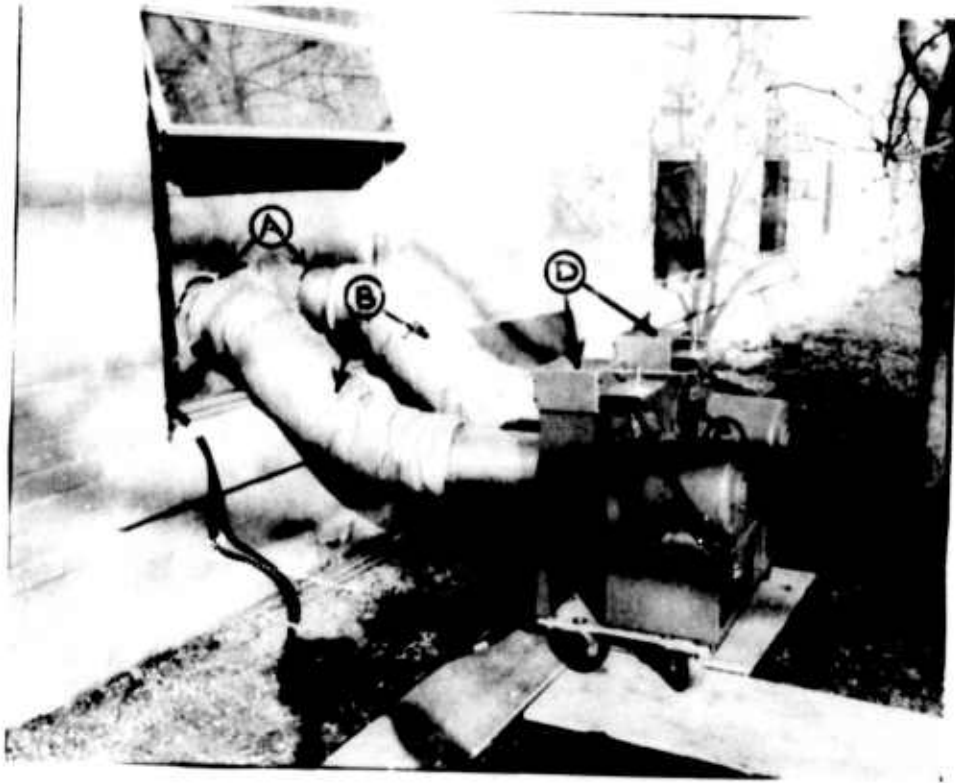


Fig. 7. The test set-up outside of the building. A.) nozzles, B.) flexible hoses, C.) blowers, D.) valves.

the blower was controlled with a sliding door valve (Figure 7-D) on the exit of the blowers allowing a variable flow rate from zero to 1830 C.F.M.

The heated test plate (Figure 8) was made of aluminum 19" long and 9 7/8" wide. The top surface was flat within ± 0.005 overall with a sand blasted finish. The leading edge (Figure 8-A) had a 1/8" Rad. tangent to both the top surface and the 30° slope of the bottom cover plate. The body (Figure 8-B) was 1/4" thick. Twenty-five iron-constantan thermocouples were potted into drilled holes on the bottom surface of the top plate in rows of five with Sauerisen electric heater cement. Their positions are shown in Figure 8. The thermocouple leads left the plate at the rear (Figure 11-A). The space between the heating element and the body was filled with a mixture of Sauerisen cement and copper powder to improve heat transfer.

The heating element was made of Nichrome alloy wire, size 11, B. and S. No. 29 with soft temper and a resistance of 5.3 ohms per foot. The heater contained eight separate 46.4 ohms circuits (Figure 8) giving a total heater flux of 1100 watts at 80 volts R.M.S. over an area of 1 square foot per side. The wire zigzagged across the element every 5/32" in Sauerisen cement laid between sheets of asbestos paper resulting in a 1/8" total thickness. The heater was cemented in place behind the thermocouple lead space. Copper leads to the rear of the plate were provided for

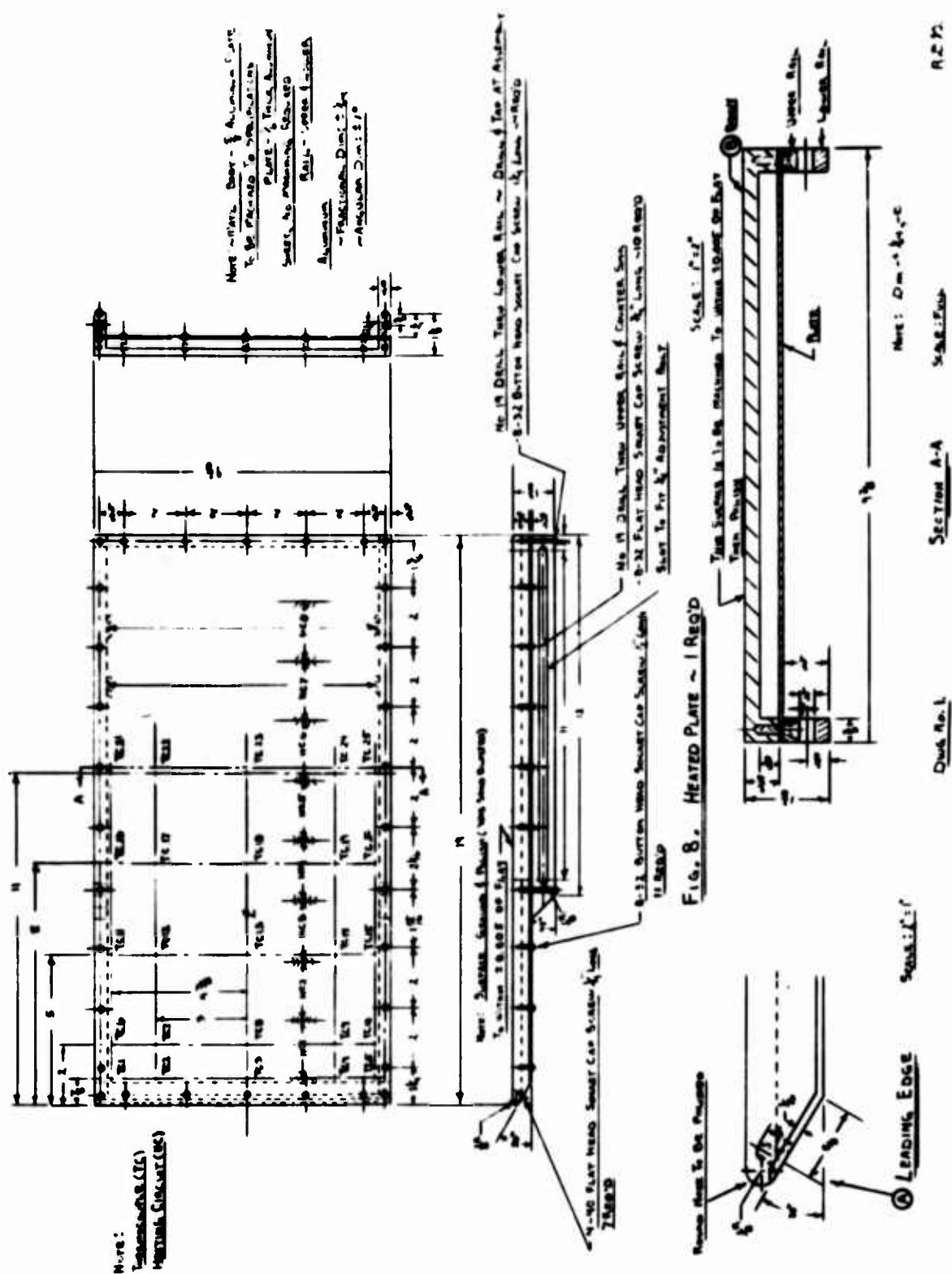
connection of the heating elements to the external power supply (Figure 11-B). The remaining space to the bottom cover plate was filled with asbestos paper and Sauerisen cement.

Side rails (Figure 8) fitted to the bottom cover plate were slotted to allow adjustment of the plate so it could be viewed at different positions up to 14" from the leading edge (Figure 5).

The plate power was controlled by a combination of variacs and variable resistors. The overall power was controlled by a 20 amp. variac (Figure 4-A). Four 10 amp. variacs (Figure 9-B) in series with the 20 amp. variac supplied power to every two adjacent circuits. Fine heater circuit adjustment was accomplished with 8 variable resistors (Figure 9-C).

The plate temperature was monitored by a Leeds and Northrup millivolt potentiometer (Figure 9-D) using an ice bath (Figure 9-E) for reference. A 24 way switch (Figure 9-F) allowed rapid reading of the thermocouples.

A grid of 0.006" diameter stainless steel wires running parallel to the plate in the direction of flow was supported by two plexiglass beams. The lower beam (Figure 10) was located in the settling chamber. Sliding engagement with two steel tension rods perpendicular to the aerodynamic beam provided gross grid-plate spacing adjustment. The upper beam (Figure 11) located at the top of the test section was



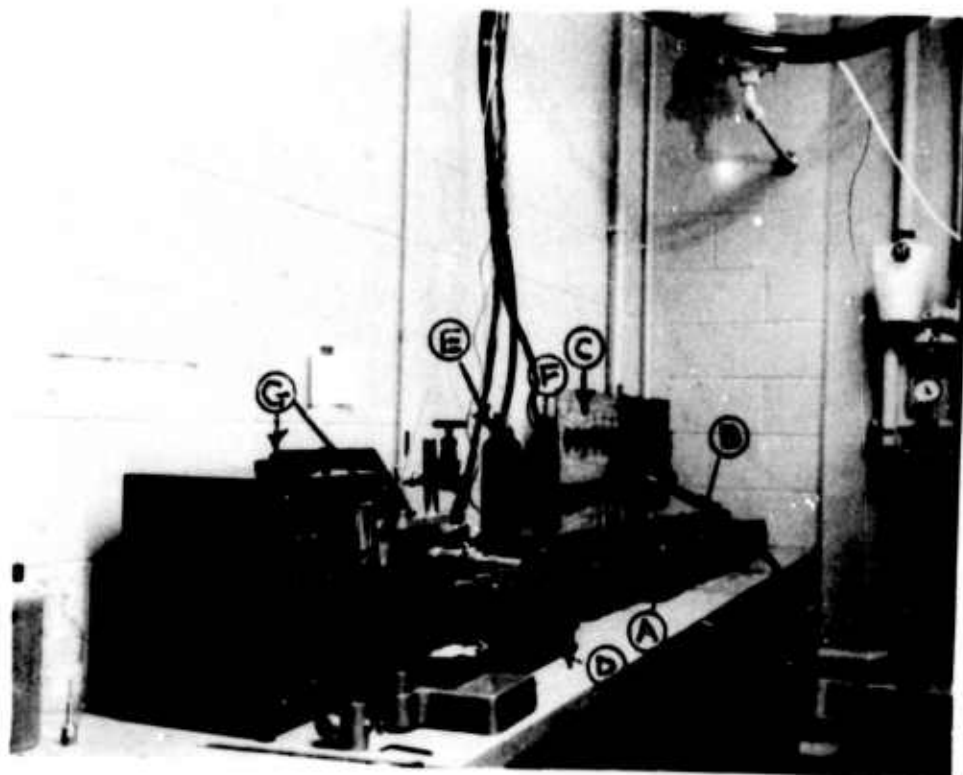


Fig. 9. Instrumentation and power supply. A.) 20 amp variac, E.) 4-10 amp variacs, C.) variable resistors, D.) potentiometer, F.) ice bath, F.) 24-way switch, G.) micromanometer-gaertner comparator set-up.

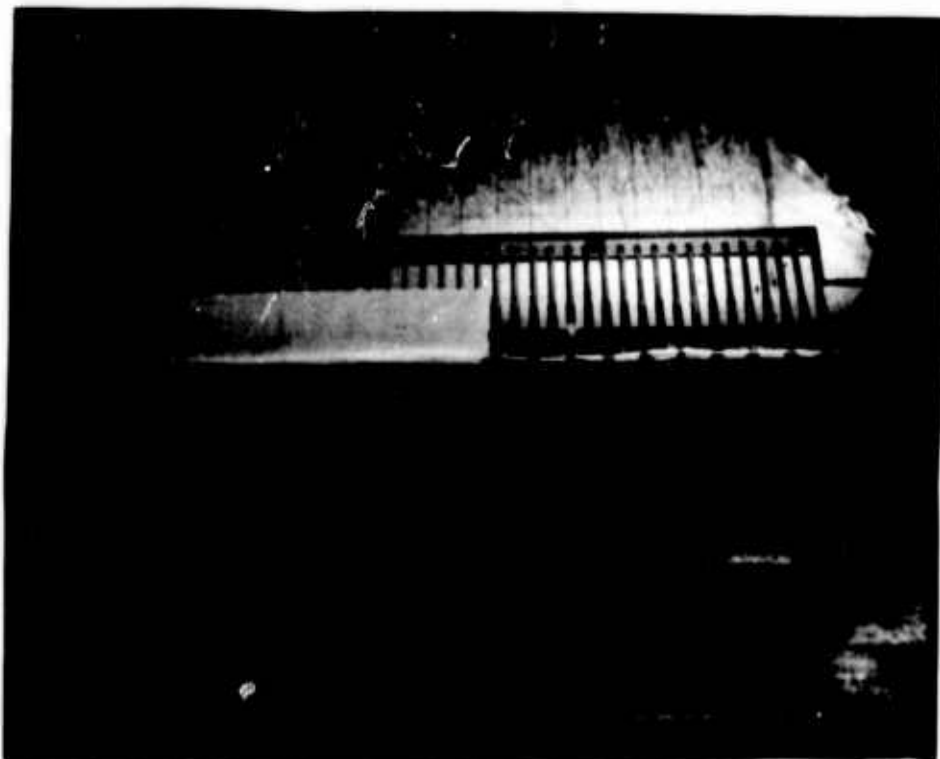


Fig. 10. The lower beam.

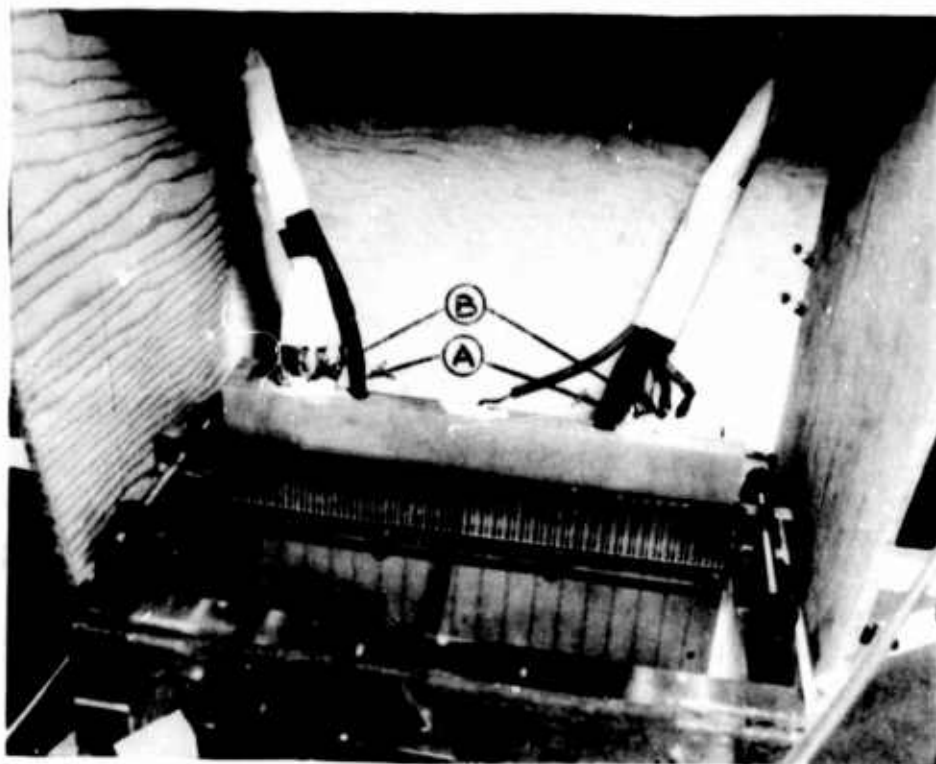


Fig. 11. The upper beam. A.) thermocouple leads, B.) plate power leads.

supported on a threaded rod for grid-plate spacing adjustment. To accomplish fine grid-plate spacing a nylon cord (Figure 4-E) was held in tension across the test section so that all the wires from the lower beam just touched it insuring constant spacing. The position of this cord was located by a threaded adjustment.

Each wire was soldered to one eye of a swivel, the other eye slipped over the high voltage lead wire (Figure 11). The wire was passed through a hole in the upper beam to give constant wire-wire spacing, then down past the nylon cord to the bottom beam. There it passed through a threaded section of brass tubing screwed into the beam (Figure 10). With tension on the wire, the end of the tube was crimped and soldered. With all wires in place, the tubes were backed off to put tension on the wires. Uniformity in tension was obtained by noting the pitch when plucked.

Grid current was supplied by a Sorensen 5038-4 high voltage source (Figure 12-A). Current from the source was measured on the high voltage side by a Westinghouse type PX-161 micro-ammeter (Figure 12-B) contained within a plexiglass box. A neon bulb protection circuit (Figure 12-C) was placed in series with the meter to guard against sparking. The grid voltage was measured by Singer model SEH electrostatic voltmeter (Figure 12-D).

The Mach-Zender interferometer was modified by adding two 1" thick optical flats in the reference leg to compen-

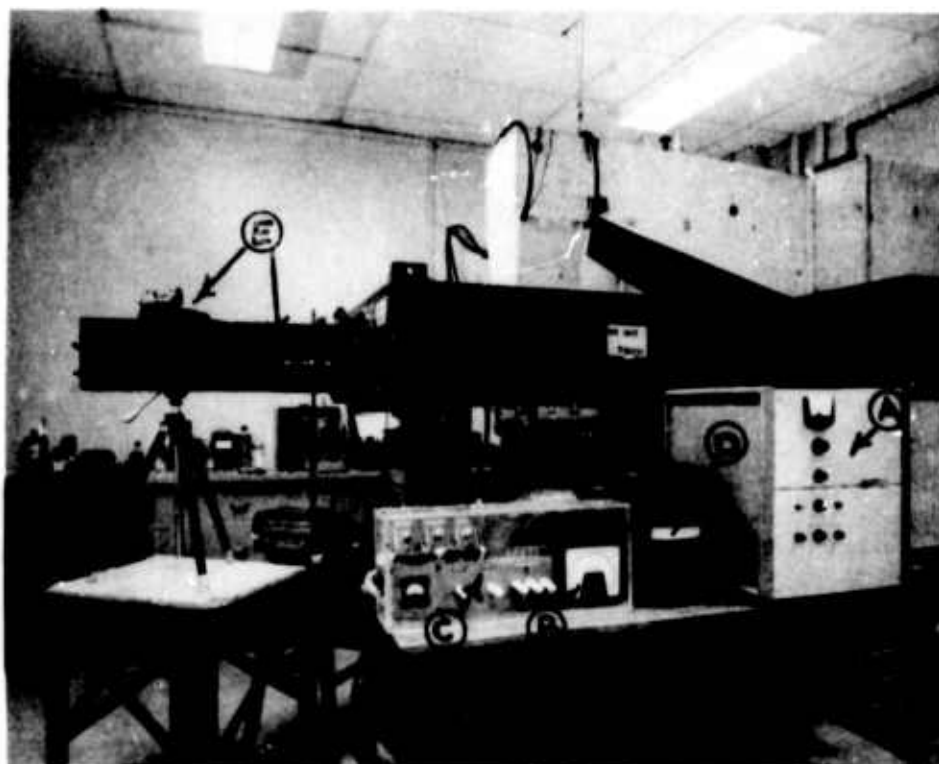


Fig. 12. The test set-up. A.) high voltage source, B.) micro-ammeter C.) protection circuit and switch, D.) electrostatic voltmeter, E.) camera.

sate for the optical flats in the test section walls. Because path lengths were still not the same some readjusting was necessary. The aligning procedure is described in Appendix II. Also a Baird Atomic D-9 interference filter with a peak wavelength for the green line of mercury of 5460 \AA and tolerance of $+15, -0 \text{ \AA}$ was installed.

A Speed Graphic camera fitted with a Polaroid 4x5 film holder was used in conjunction with a shutter to form a camera (Figure 12-E). Polaroid 200 speed film was exposed at $1/25$ shutter speed.

The stream velocity was determined by making pitot-static measurements (Figure 4-F). For low velocities the pressure difference was read using a micromanometer-microscope set-up (Figure 9-G). At higher velocities a 0 to 3 inch Ellicson inclined manometer (Figure 4-G) was used.

The wire-wire, and grid-plate spacings used in these tests were $1/2$ and $1/4$ inches respectively.

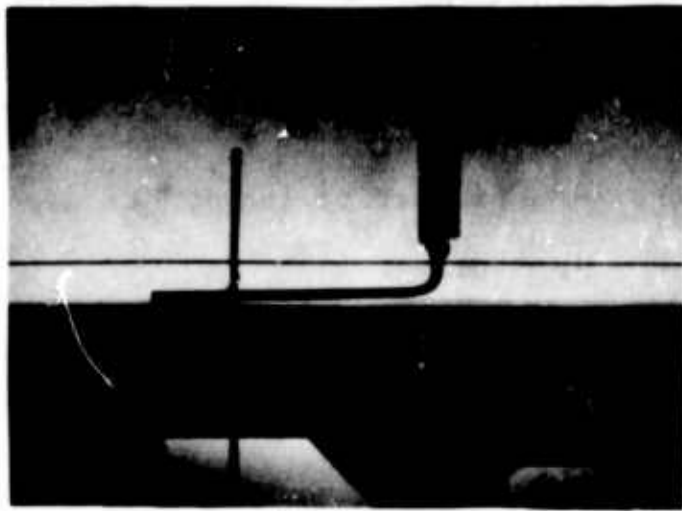
TEST PROCEDURE

In working with the interferometer, care must be taken to insure proper interpretation of the interferograms. The following procedure was used throughout the testing. The plate was positioned so that the region on the plate of interest was in view. The plate was made parallel to the test section wall by rotating the plate about its longitudinal and horizontal axis by alternate adjustment of plate-test-section bolts (Figure 5-B) fitted in slots in the test section wall. Parallelism was checked with a depth gauge micrometer at three points on the plate. The front wall of the test section was used as a reference. When the three points were within 0.005 inches, parallelism was considered accomplished.

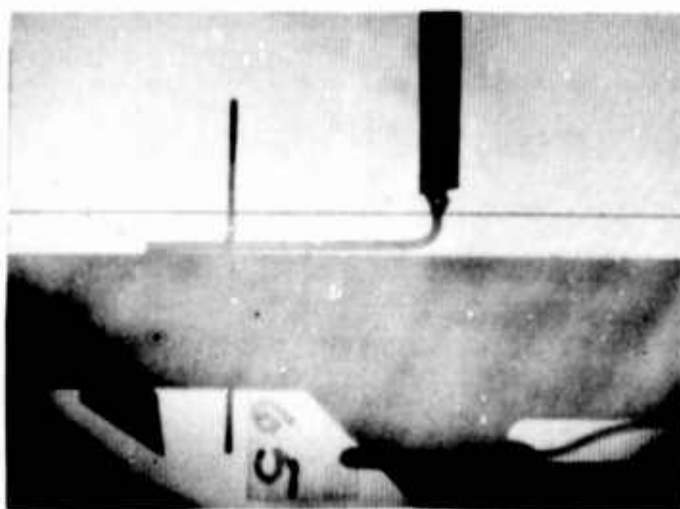
A similar procedure was used to locate the wire plane parallel to the plate. Using the plate surface as a reference, the beams and nylon cord were adjusted until the four grid-plate spacings were within one grid wire diameter of each other.

The damping screen (Figure 4-I) was now bolted to the nozzle. The optical flats were placed in the test section wall and adjusted to give a continuous internal test section surface.

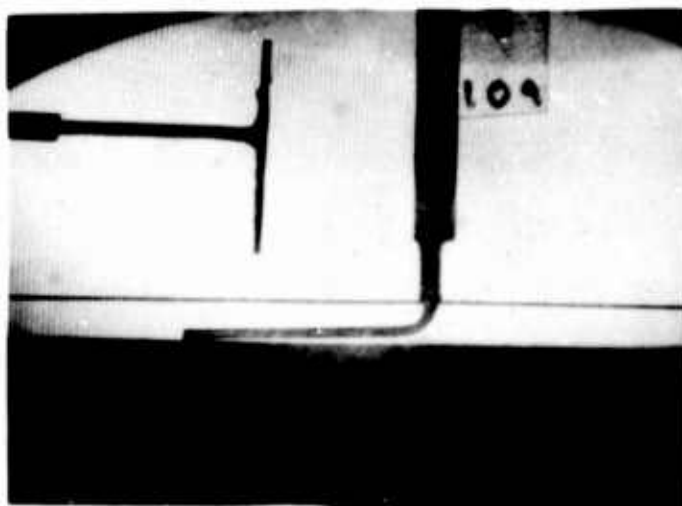
A glass probe was moved up to the plate surface (Figure 13). The camera was positioned so that the object plane coincided with the center of the plate to reduce refraction



Case A



Case P



Case C

Fig. 13. Reference photos.

error. The fringes were focused at the object plane (by the method described in Appendix II). The test section was then rotated about its vertical axis until the probe appeared just to touch the plate at its tip. The displacement fringes were made perpendicular to the plate by adjustment of mirror M2 (Figure 56). The interferometer optics was now ready for testing. A reference picture was then taken (Figure 13).

The glass probe was then retracted and replaced by a thermocouple (Figure 4-H) to measure free stream temperature.

The blower was started and the valve adjusted to give the desired flow rate. The plate was heated so that the surface temperature was uniform within 1°F from front to back (at high free stream velocities, the surface temperature varied across the plate from side to side. Since the heater circuits ran from side to side no adjustment could be made to reduce the 3° max cross plate temperature variance). When steady state was reached the no current picture was taken. Next grid voltage was adjusted until the desired grid current was obtained. If the plate temperature varied it was adjusted to no current conditions. All thermocouples were read and recorded at each test condition as well as stream velocity and temperature. Barometric pressure, wet and dry bulb temperatures were taken at the beginning of each test.

EVALUATION OF INTERFEROGRAMS

Temperature profiles were obtained by careful measurement of fringe displacements. To accomplish this the following procedure was used. The reference length "T" (Figure 5-D) was measured with a machinist rule. Since the actual length of the cross bar of the "T" was known, the photo magnification could be determined. Pointers marking distance from the leading edge located on the rear of the plate (Figure 13) were marked with a needle puncture for easy location in the field of the microscope. The interferogram was placed on the stage (Figure 14-A) of the Gaertner comparator and squared by tracing the upper edge of the plate with the cross-hair in the eye piece (Figure 14-B). The station was then located and a visual perpendicular erected to the upper surface. The location from the perpendicular of an even inch of actual length from the leading edge was determined then located under the cross-hairs. A needle puncture was made. An inch of actual length was then traversed along the upper edge and another position marked. Dividers were then used to locate the other positions.

The interferogram was removed from the stage so an extension of the straight line portion of the fringes could be etched to the upper edge at each position of interest (Figure 15). The interferogram was mounted once again and aligned along one of the etched lines. The microscope carriage (Figure 14-C) was then moved until the cross-hairs

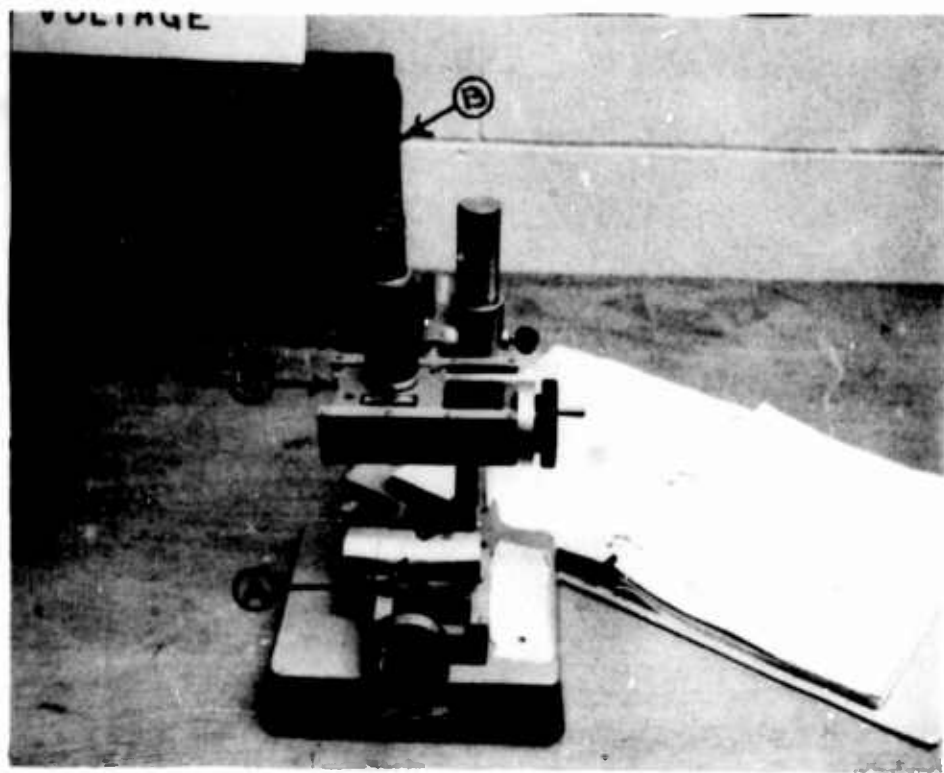


Fig. 14. The gaertner comparator. A.) stage, B.) eye piece, C.) microscope carriage.

were at the edge of the nearest up stream fringe. The stage was moved along that slope until the edge of the next fringe appeared under the cross-hairs. Its position was recorded and the process continued until the upper surface was reached, or the photo became unreadable. The position of the upper surface was noted as a ground reference. The profiles at other positions were determined in a similar manner. The interferogram was then aligned with the upper surface of the plate and the angle that the etched line made with the upper surface was measured. This procedure was checked by making measurements on photos taken by Kennard (Reference 6) and were found to be within 1° F. Also a free convection test was run (Figure 15) and its results compared with the well established Pohlhausen solution (Reference 4) as shown in Figure 16. The correlation was very good. This provided another check on the method (the chimney effect was neglected).

The temperature corresponding to each fringe was calculated by comparing conditions in the test section with known conditions in the reference leg by the procedure outlined in Appendix III.

Sources of errors in evaluating the interferograms (Reference 7) were found in determining the plate surface, locating the fringe edges near the edge of the boundary layer, and refraction of the light in the non-uniform density field of the boundary layer.

Case A

Case B

Case C

Case D

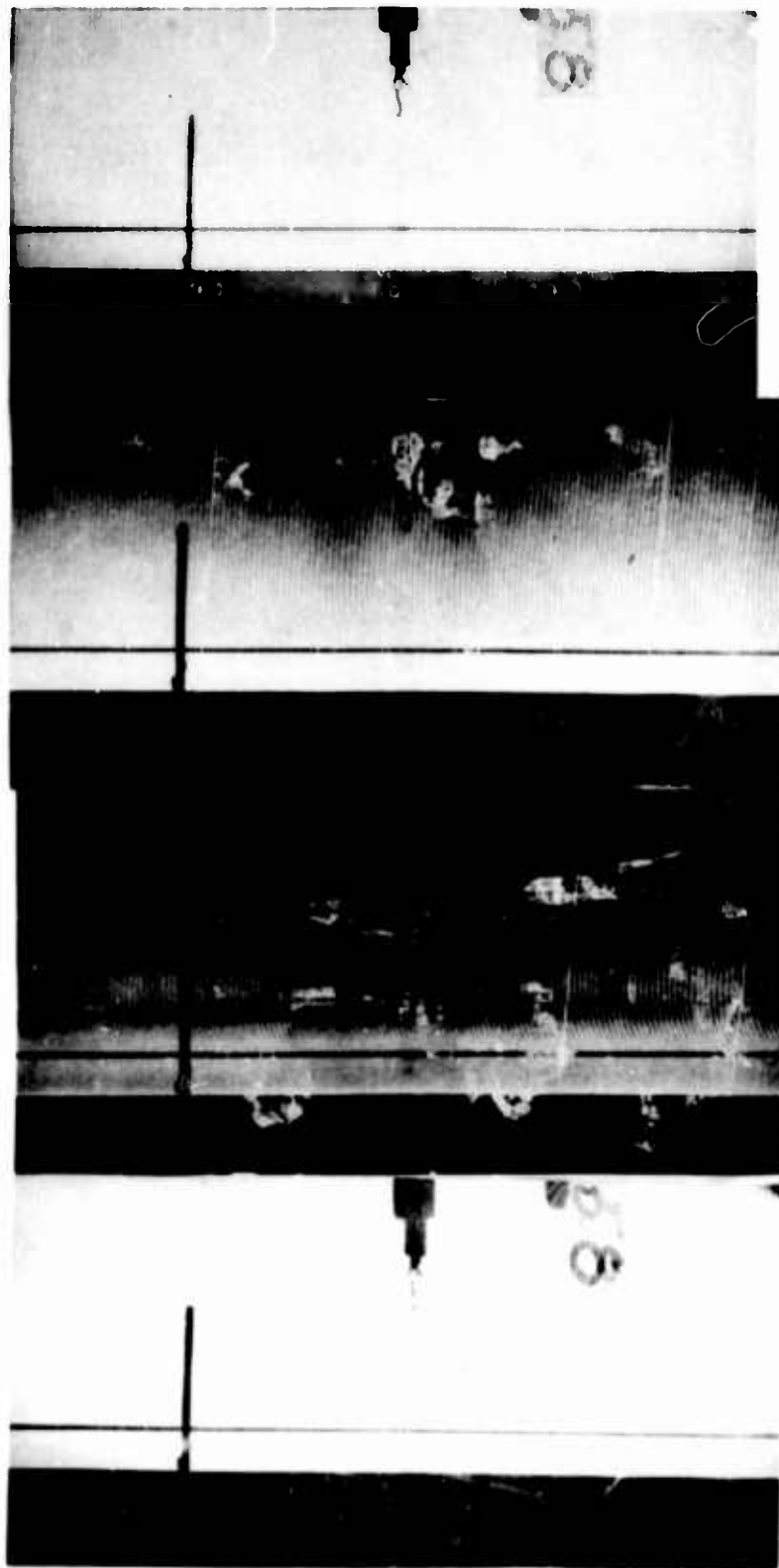


Fig. 15. Interferometer pictures of free convection heat transfer on a vertical flat plate. Plate temperature 157°F , room temperature 75°F .

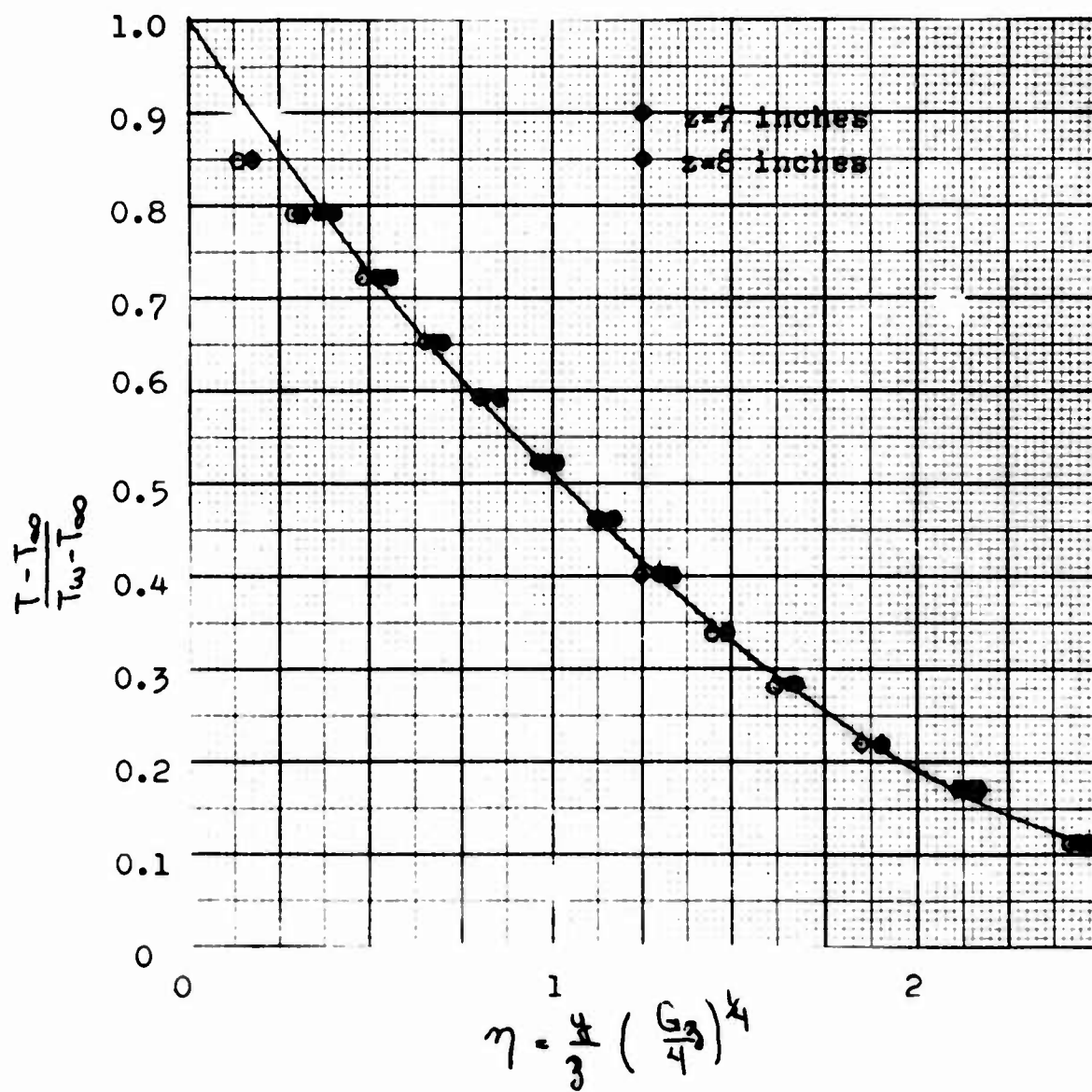


Fig. 16. Experimental points for the free convection test plotted against Pohlhausen's solution.

The surface of the plate is not sharply defined in an interferogram because of the angular deviation of the light from the extended source. A combination of reflected and refracted light from the plate interferes with the light from the beam that travels around the tunnel and the interference produces the pattern at the surface of the plate as shown in Figure 13. This region extends 0.024 inches above the surface and causes uncertainty in the location of the surface. In order to determine the surface accurately, an object of known geometry was photographed against the surface (Figure 13). By calculating the angle the probe made with the surface and the closeness to the end of the probe visible in the photo, the surface was located within 0.002 inches. The distance from the determined surface to the mean position of the wire grid was measured. By comparing this distance with the measured distance from mean wire position to apparent upper plate surface, the actual upper plate surface could be located for the no grid current photo of each test. It was assumed that this spacing was constant throughout a test.

In the region near the edge of the boundary layer, where the temperature gradient is relatively small, determination of the fringe edge was least accurate.

Large errors may occur due to refraction of light in the non-uniform density field of the boundary layer. When the density at the surface is less than in the main stream,

the light is bent away from the surface, as schematically shown in Figure 17. Instead of traversing the boundary layer at a constant density, the light passes through layers of increasing density. The average density along the light path is therefore higher than the density at the entrance height. Because the density difference is directly proportional to fringe shift, the fringe shift is less than would exist with no refraction.

The light after traversing the boundary layer makes an angle θ_e with the plate surface at the inside of the tunnel window. On striking the glass at an angle, the light is refracted according to Snell's Law and passes through the glass in a straight line at an angle θ_r . Without refraction in the boundary layer, the light path in glass would have been γ . With refraction, the path becomes $\frac{n_g \gamma}{\cos \theta_r}$ which is an increase in path length of $\frac{n_g \gamma (1 - \cos \theta_r)}{\cos \theta_r}$. This quantity, divided by the wavelength of light in a vacuum, is the decrease in fringe shift. Two methods of accounting for these errors are outlined in Appendix IV.

The data presented in this thesis ~~were~~ not corrected for refractive error because of the unsteady nature of the corona observed. If the data presented in Figure 15 actually corresponds to the Pohlhausen solution, it can be noted that the theory and test data deviate only near the plate. This gave a qualitative measure of the refractive error. An attempt was made to estimate the refractive error by the

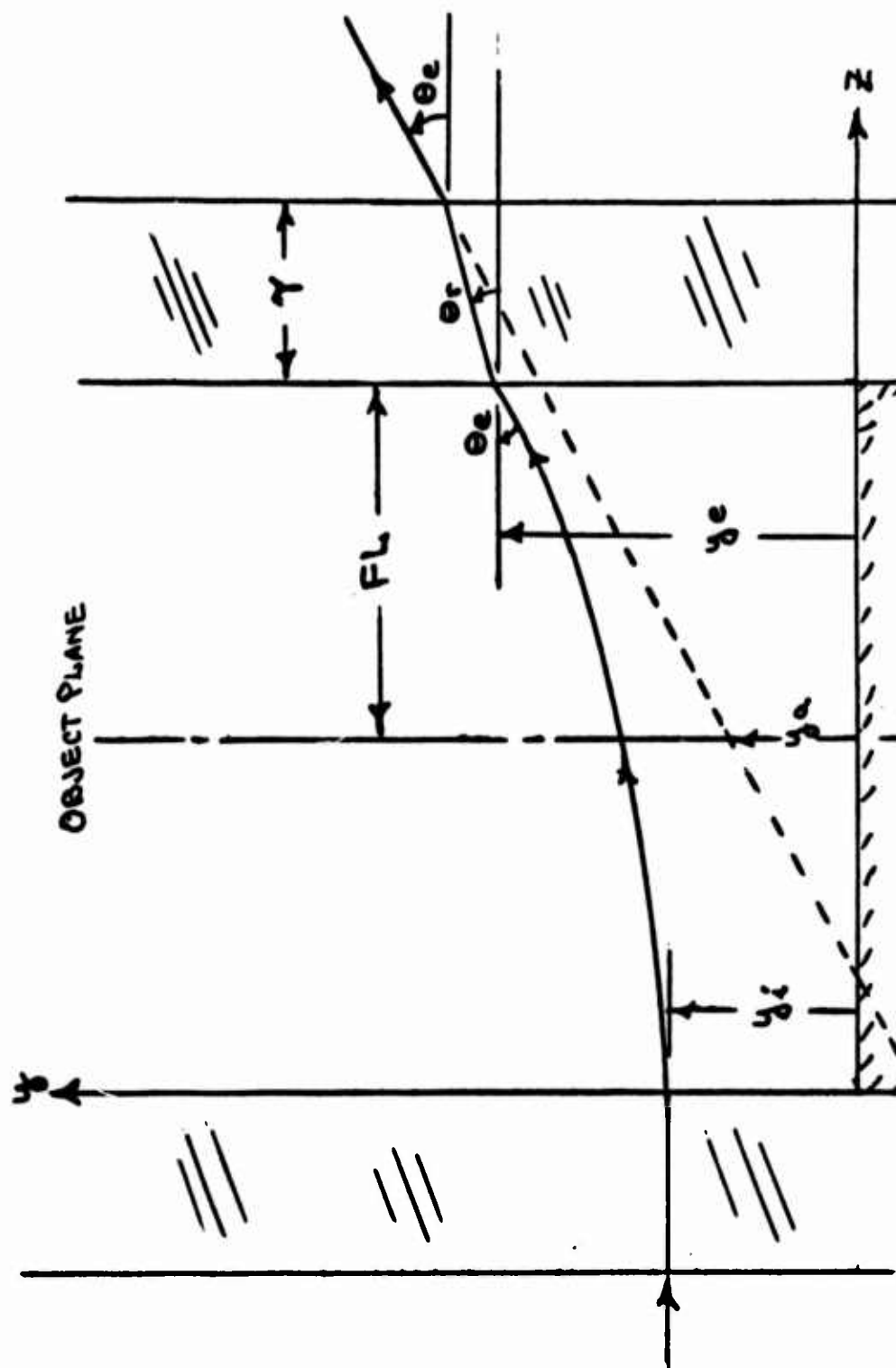
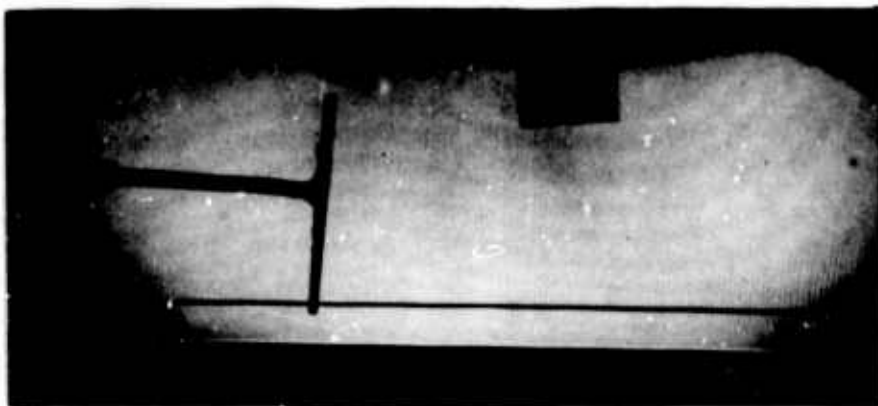


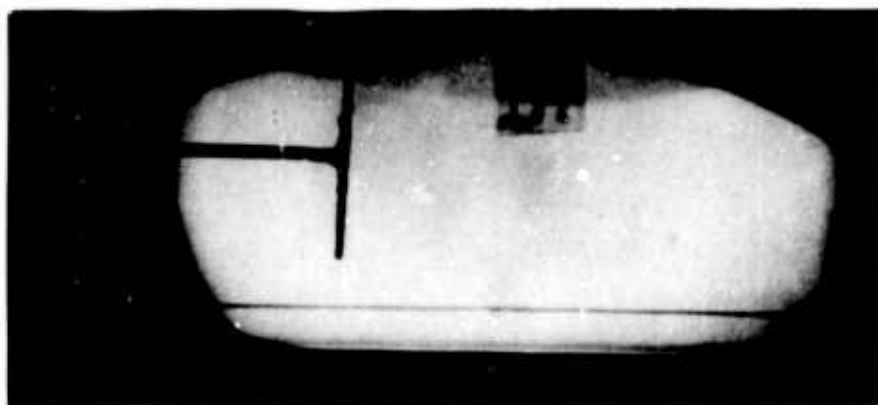
Fig. 17. Schematic diagram of the light path through the boundary layer.

two object plane method described in Appendix IV. It was unsuccessful because the fringes were so out of focus at the new object plane that the interferograms were unreadable (Figure 18). Relocation of the fringe focal plane would have necessitated changing the system optics.

In order to compare the test results with the theory discussed in a previous section, the data was reduced to non-dimensional form. The quantities in the non-dimensional group $\frac{T - T_{\infty}}{T_w - T_{\infty}}$ were determined as follows. $T - T_{\infty}$ was calculated by equation (12) of Appendix III. T_w was determined from an average thermocouple reading in the region of interest. T_{∞} was taken to be room temperature as read on a mercury bulb thermometer. A thermocouple was placed in the stream but was found to give erratic readings. The quantity $\eta = \eta(\omega_{\infty}, z, \gamma, y)$ was calculated for the two positions investigated. ω_{∞} was determined from pitot-static reading in main stream ahead of the plate. To account for the area reduction caused by the plate, a pressure profile was taken at the test site (P2 in Figure 5) and compared with concurrent readings ahead of the plate (P3 in Figure 5). The results are shown in Figure 19. The velocity corresponding to the flat portion of those curves was taken as ω_{∞} . A calibration curve (Figure 20) was developed by plotting these values against those ahead of the plate. γ was evaluated at the mean temperature $\frac{T_w + T_{\infty}}{2}$. z was measured from the leading edge. The y 's used were not corrected for refrac-



A. Object plane at plate center line.



B. Object plane at edge of test plate nearest the light source.

Fig. 18. Interference photos taken at two different object planes.

Difference between static and total pressure in inches of water

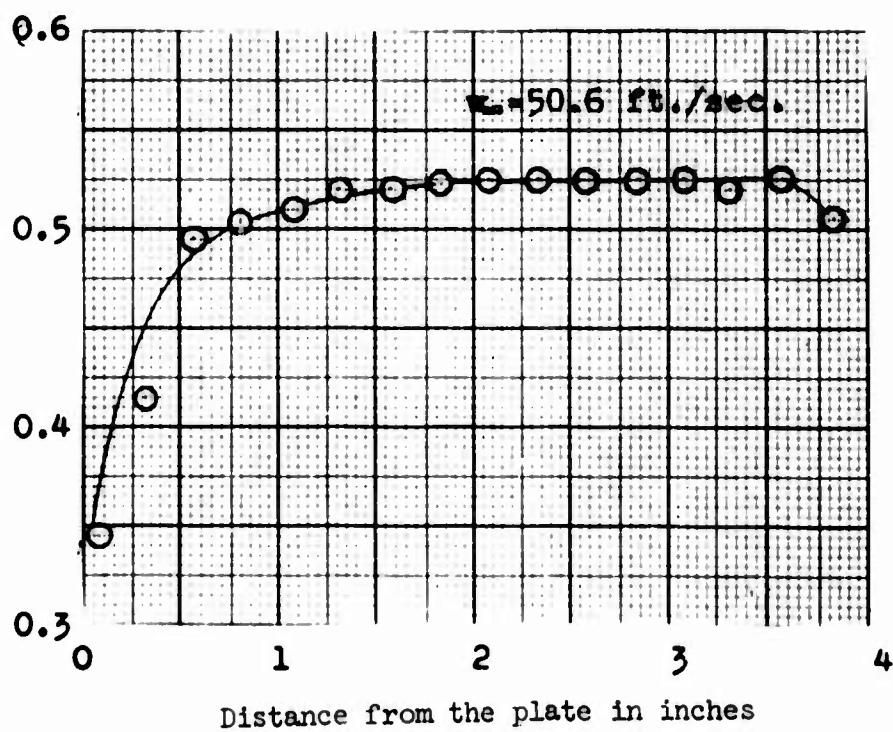
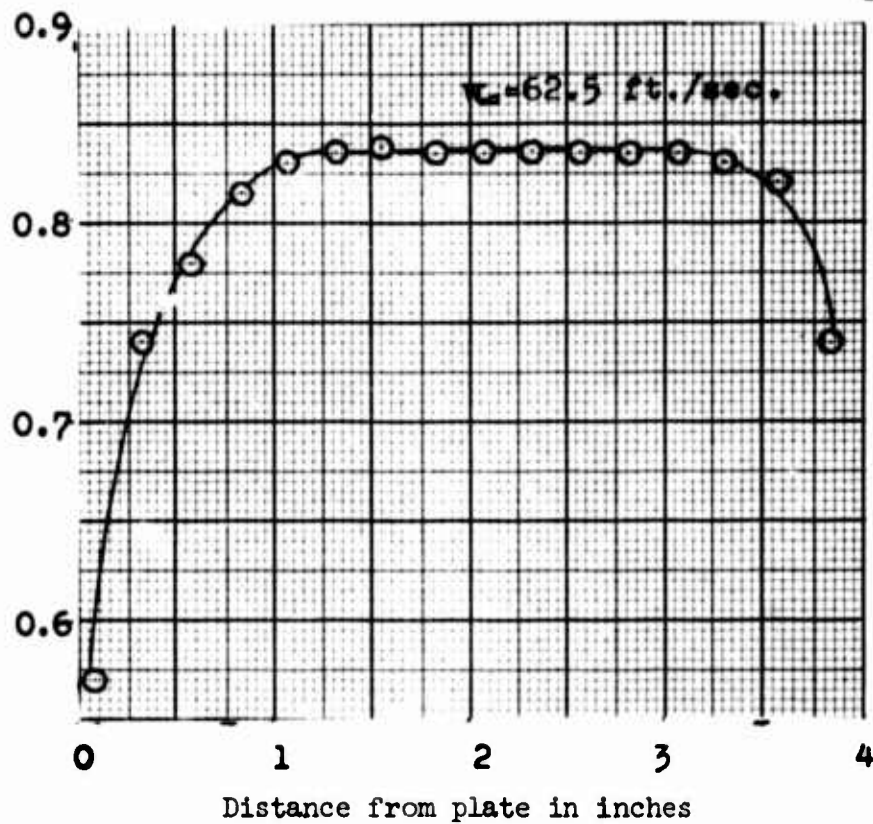


Fig. 19. Pitot-static pressure profile at the test site (P2).

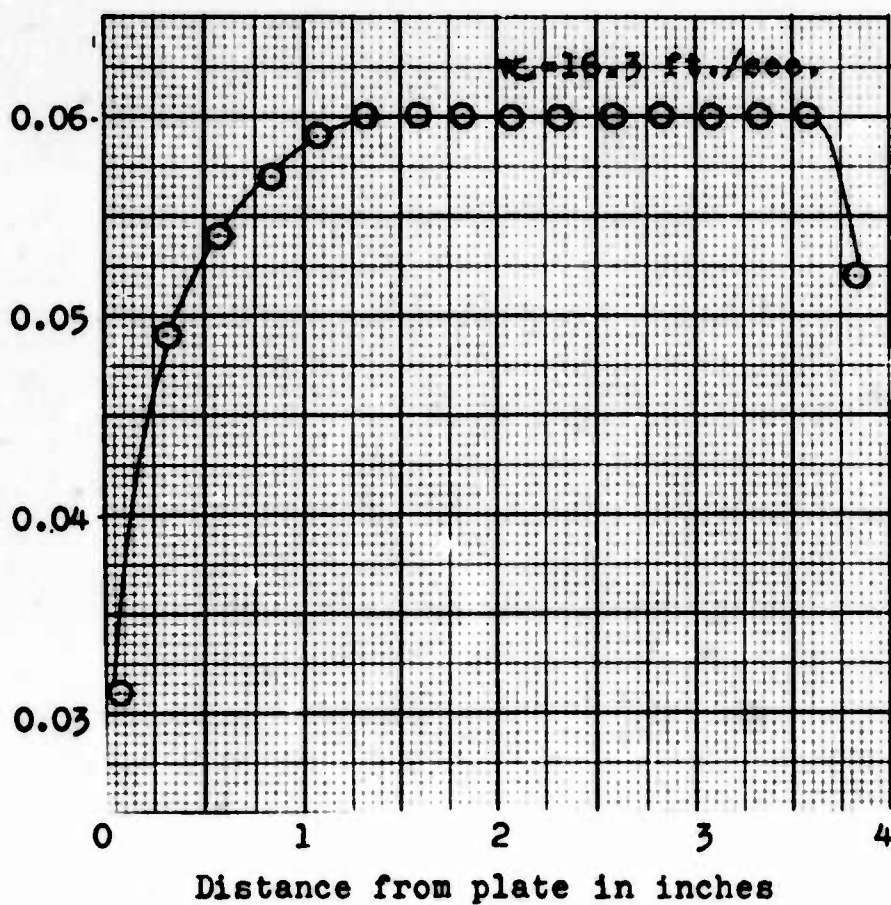
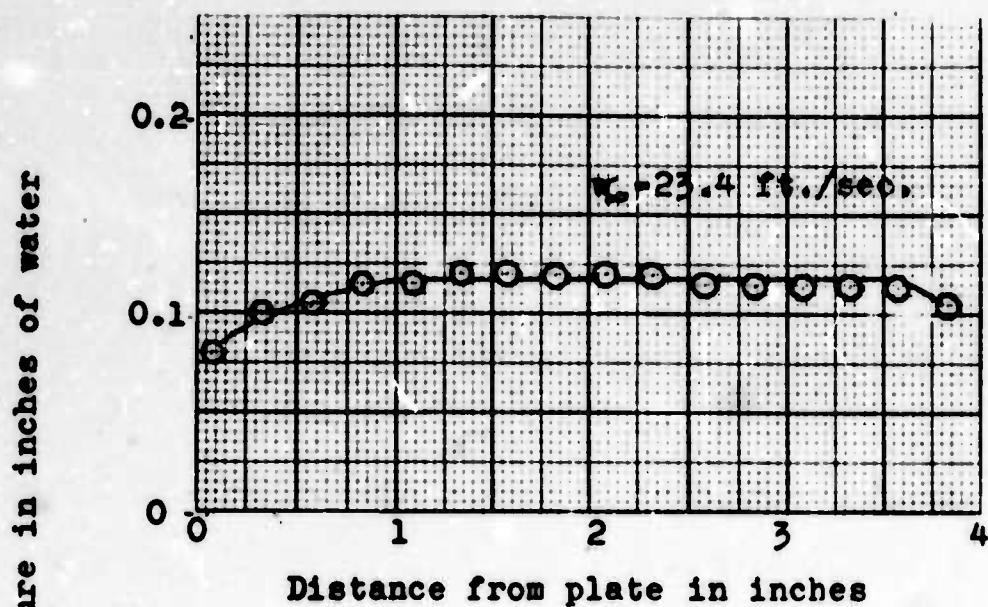


Fig. 19 con't. Pitot-static pressure profile at the test site (P2).

Difference between static and total pressure in inches of water

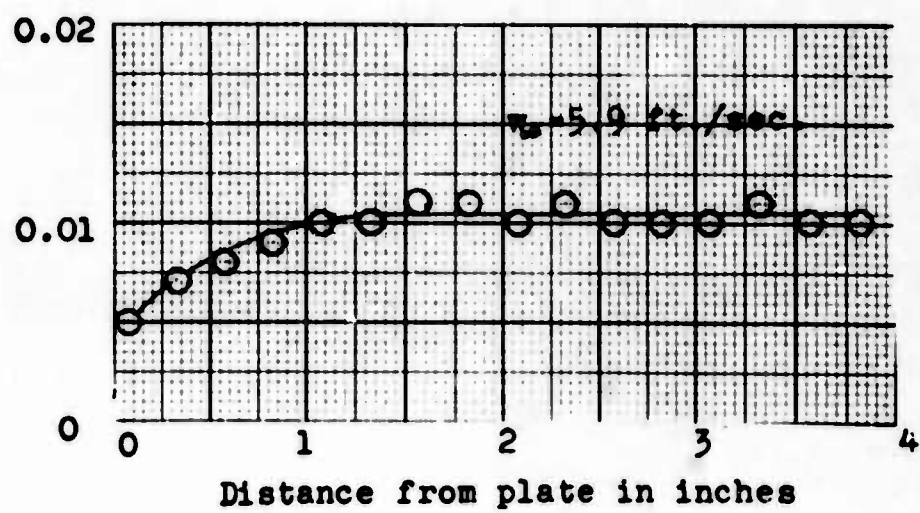
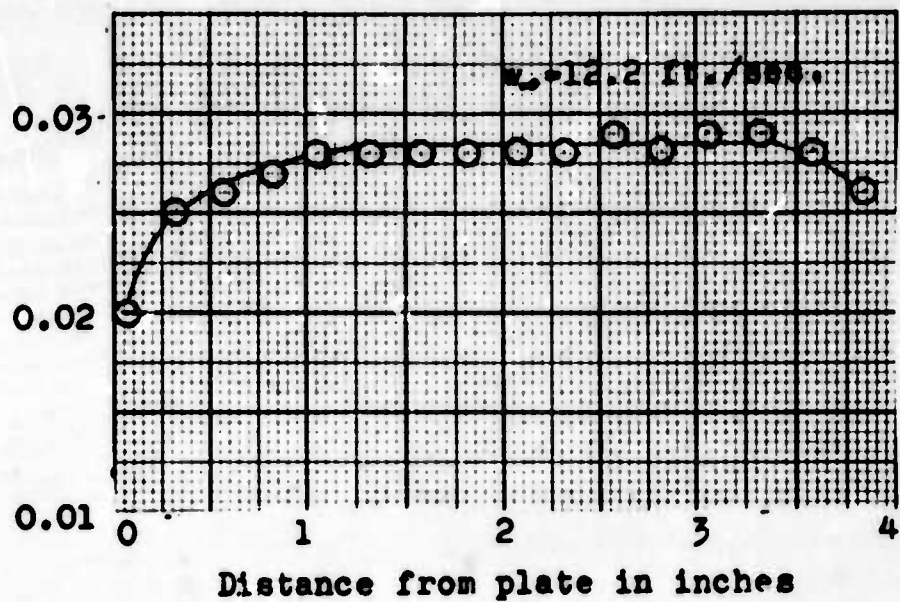


Fig. 19 con't. Pitot-static pressure profile at the test site (P2).

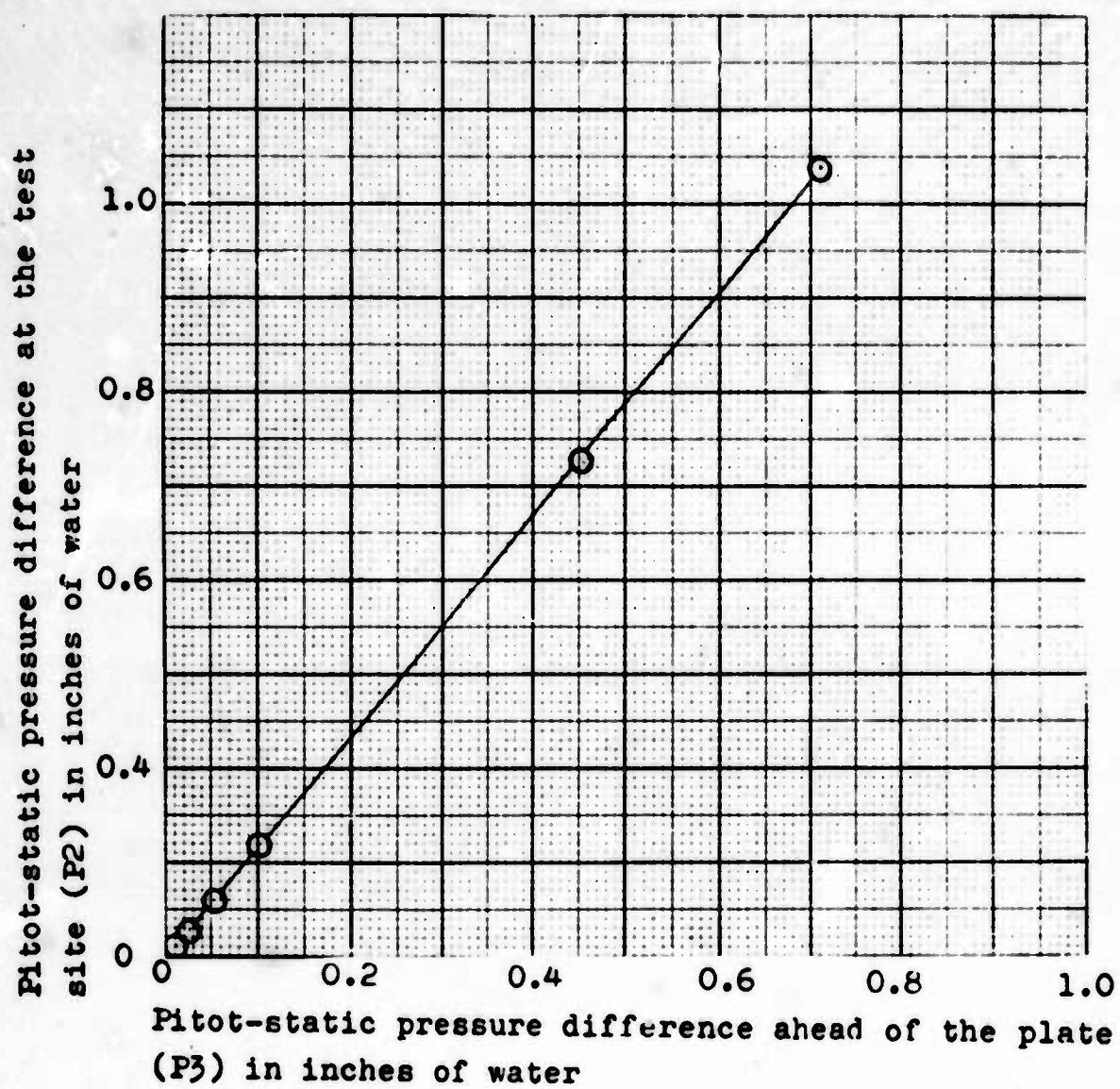


Fig. 20. Velocity calibration curve.

tion error. Values of $\frac{\eta}{\gamma}$ are tabulated in Table 1.

The quantity $m_3 = f(\rho_c, \rho, K^+, u_0)$ was determined for the conditions corresponding to each photo. The mobility (K^+) for dry air as reported by Cobine (Reference 8) was $1.36 \frac{\text{cm}^2}{\text{VOLT SEC}}$. The density (ρ) was evaluated at the mean temperature. The charge density (ρ_c) was estimated as follows. One of the assumptions of the theory was that $\rho_c = \text{constant}$ in the boundary layer. The total grid current flux (J) was assumed to be uniformly distributed over the plate therefore $\rho_c = \frac{J}{J_0}$ where J_0 is the average drift velocity. Since $J_0 = K^+ E$ the only quantity to be calculated is the field strength in the boundary layer. By a method of images (Figure 21) outlined by Attwood, (Reference 9), the field strength at the surface of the plate, excluding space charge effects, caused by one wire at a height h was

$$E = \frac{(Q_L)_e}{2\pi \epsilon} \frac{h}{x^2 + h^2}$$

where $(Q_L)_e$ is an equivalent current density per length derived from

$$V = \frac{(Q_L)_e}{2\pi \epsilon} \ln \frac{D}{R}$$

D is twice h . R is the radius of the wire and V is the grid voltage. The number of wire spacings (L) for the field strength to diminish to a value one order of magnitude less than the values directly below the wire was calcu-

Table 1

Values of $\frac{\eta}{\gamma}$ for various tests and positions.

Test	$\frac{w_{\infty}}{F_c}$	$\gamma \times 10^3 \frac{1}{F_c}$	$\gamma \frac{1}{F_c}$	$\frac{w_{\infty}}{\gamma} \frac{1}{F_c}$	$\sqrt{\frac{w_{\infty}}{\gamma}} \frac{1}{F_c}$	$\sqrt{\frac{w_{\infty}}{\gamma}} \frac{1}{w}$
8	5.9	0.196	0.583	5.17×10^4	2.27×10^2	1.89×10^1
8	5.9	0.196	0.667	4.52	2.12	1.77
9	12.2	0.196	0.583	1.07×10^5	3.27	2.73
9	12.2	0.196	0.667	0.94	3.06	2.55
10	16.3	0.196	0.583	1.43	3.78	3.15
10	16.3	0.196	0.667	1.24	3.52	2.94
11	23.4	0.196	0.583	2.05	4.53	3.78
11	23.4	0.196	0.667	1.79	4.24	3.53
12	50.6	0.196	0.583	4.43	6.65	5.55
12	50.6	0.196	0.667	3.87	6.22	5.20
13	62.5	0.196	0.583	5.48	7.40	6.17
13	62.5	0.196	0.667	4.78	6.91	5.77

γ was evaluated at $\frac{T_w + T_{\infty}}{2} = 110^\circ \text{F.}$

lated and found to be two for the geometry of this test. The average \bar{E} for six wires was taken by integrating $\sum E$'s between the third and fourth wire and dividing by L .

$$E_{AVE} = \frac{2Vh}{L \ln \frac{D}{R}} \int_0^L \left[\frac{1}{(x+2L)^2 + h^2} + \frac{1}{(x+L)^2 + h^2} + \frac{1}{x^2 + h^2} + \frac{1}{(x-L)^2 + h^2} + \frac{1}{(x-2L)^2 + h^2} + \frac{1}{(x-3L)^2 + h^2} \right] dx$$

Evaluation for the test geometry gave $E_{AVE} = 1.51 \sqrt{\frac{\text{VOLTS}}{\text{INCH}}}$.

The sum of the vectors \bar{E} could be taken in the scalar manner because all vectors were parallel and in the same direction at the plate surface.

m written in terms of test parameter is proportional to $\frac{1}{AK^2 Q} \times \frac{I}{\sqrt{W_\infty}}$ where A is the plate area below the wire grid and I the total grid current. The calculated values of m_3 for various photos are tabulated in Table 2.

Local Nusselt Numbers were calculated from the temperature profiles as follows (Reference 10). Nusselt Number defined as $Nu = \frac{h_3}{K}$ where 3 is a characteristic dimension (for the plate, the distance from the leading edge),

h is the local film heat transfer coefficient at the surface defined as $\frac{K}{\Delta T} \frac{dT}{dy} \Big|_w$, and K is the conductivity of the air at the wall temperature. Inserting the definition of h , Nusselt's Number becomes $Nu = \frac{3}{\Delta T} \frac{dT}{dy} \Big|_w$. The temperature gradient $(\frac{dT}{dy})_w$ on the surface can be determined from the temperature profile as shown in Figure 22.

The subtangent to this profile denoted by δ' is $\frac{\Delta T}{(dT/dy)_w}$.

Table 2

Values of mz for various test conditions.

Photo	V(KV)	$E(\frac{V \cdot cm}{e})$	I(μ Amps)	w_{∞}	$m(\frac{1}{e})$	mz at 7"	mz at 8"
69	5.6	1.0×10^5	200	5.9	1.01×10^{-3}	0.59×10^{-3}	0.67×10^{-3}
71	5.7	1.0	400	5.9	2.02	1.18	0.79
73	5.8	1.0	600	5.9	2.94	1.71	1.96
80	5.7	1.0	200	12.2	0.48	0.28	0.32
82	5.8	1.1	400	12.2	0.94	0.55	0.63
84	5.8	1.1	600	12.2	1.41	0.82	0.94
86	5.9	1.1	800	12.2	1.86	1.09	1.24
90	5.8	1.1	200	16.3	0.35	0.21	0.23
92	5.9	1.1	400	16.3	0.69	0.40	0.46
94	6.0	1.1	600	16.3	1.02	0.60	0.68
96	6.0	1.1	800	16.3	1.35	0.79	0.90
98	5.7	1.0	200	23.4	0.25	0.15	0.17
99	5.8	1.1	400	23.4	0.48	0.28	0.32
100	5.9	1.1	600	23.4	0.72	0.42	0.48
101	6.0	1.1	800	23.4	0.95	0.55	0.63
102	6.0	1.1	1000	23.4	1.18	0.69	0.79
104	5.8	1.1	400	50.6	0.14	0.08	0.09
105	5.9	1.1	600	50.6	0.33	0.20	0.22
106	6.0	1.1	800	50.6	0.44	0.26	0.29
107	6.0	1.1	1000	50.6	0.55	0.32	0.36
109	6.0	1.1	1000	62.5	0.44	0.26	0.30

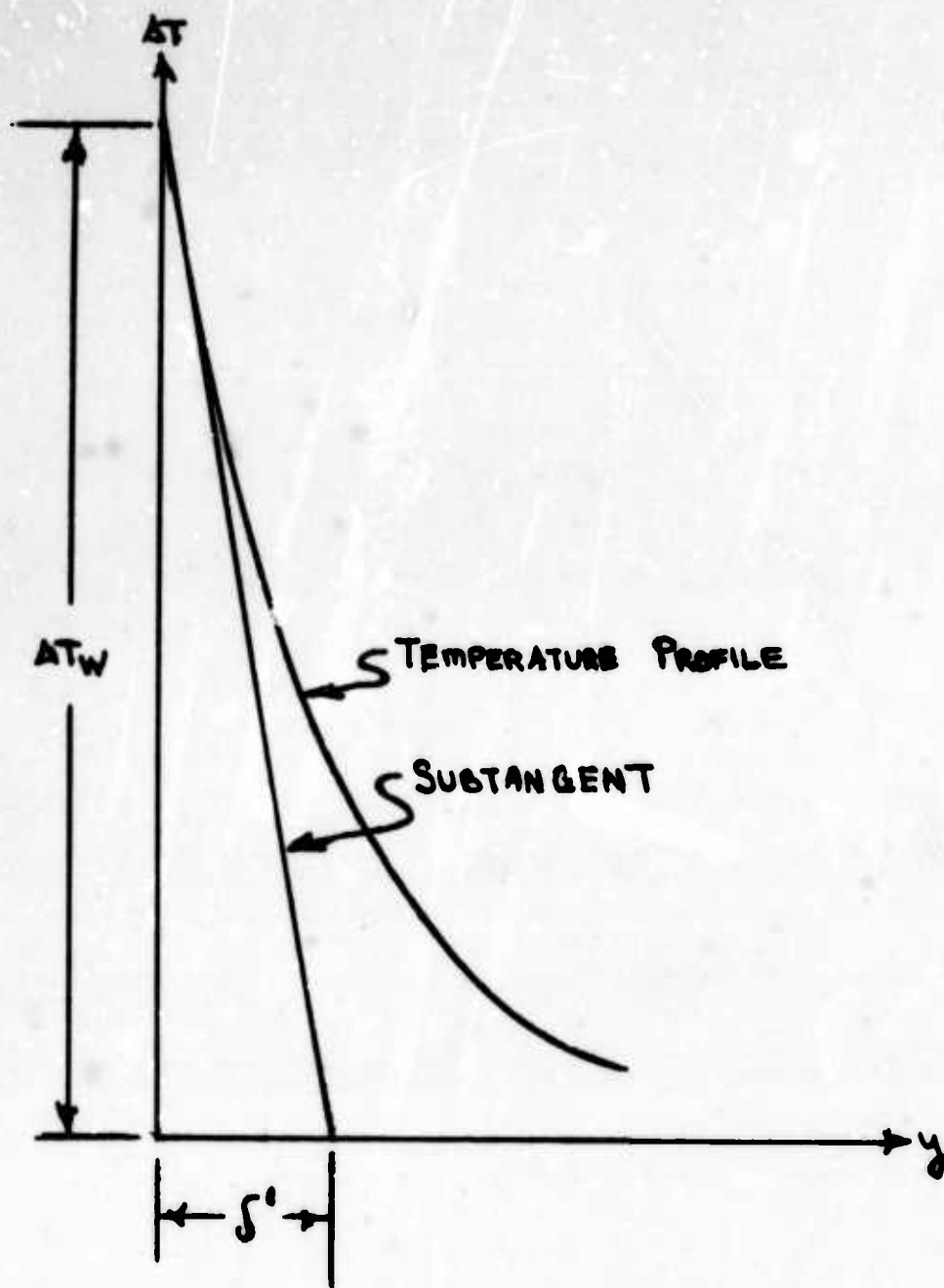


Fig. 22. Schematic of the temperature profile near the surface of the plate.

Substituting \int_0^1 , the Nusselt Number is simply the ratio of two lengths, $\frac{3}{\delta}$, one of which is predetermined as reference length used for the special problem and the second can be obtained from the temperature profile.

The accuracy of this method of determining the Nusselt Number depends on the accuracy with which the tangent can be drawn on the temperature profile. The subtangent to the test profiles were constructed assuming a nearly linear profile from 80 to 70°F ΔT.

The maximum velocity in a free convective boundary layer (w_{fmax}) was calculated by assuming the maximum value of $\frac{w}{2\sqrt{g\beta}} \sqrt{\frac{T_\infty}{T_w - T_\infty}}$ was 0.275 as shown in Schlichting. For a ΔT of 80°F, w_{fmax} was 0.925 and 0.988 feet per second at 7" and 8" from the leading edge respectively. Figure 23 shows the non-dimensional plot $\frac{Nu}{Nu_0}$ vs. $\frac{w_\infty}{w_{fmax}}$ where the zero subscript denoted the no current test.

Figures 24, 27, 30, 33, 36, and 39 present the interferograms taken at 5.9, 12.2, 16.3, 23.4, 50.6, and 62.5 feet per second respectively. The temperature profiles at two positions (7 and 8 inches from the leading edge) are shown in Figures 25, 26, 28, 29, 31, 32, 34, 35, 37, 38, 40, and 41. Temperature profiles for test conditions that resulted in similar values of the parameter mz ($a \leq mz < a + 0.02 \times 10^{-3}$) are presented in non-dimensional form $\frac{T - T_\infty}{T_w - T_\infty}$ vs. η in Figures 42 through 49. The profiles predicted by theoretical analysis are also shown (the solid curves).

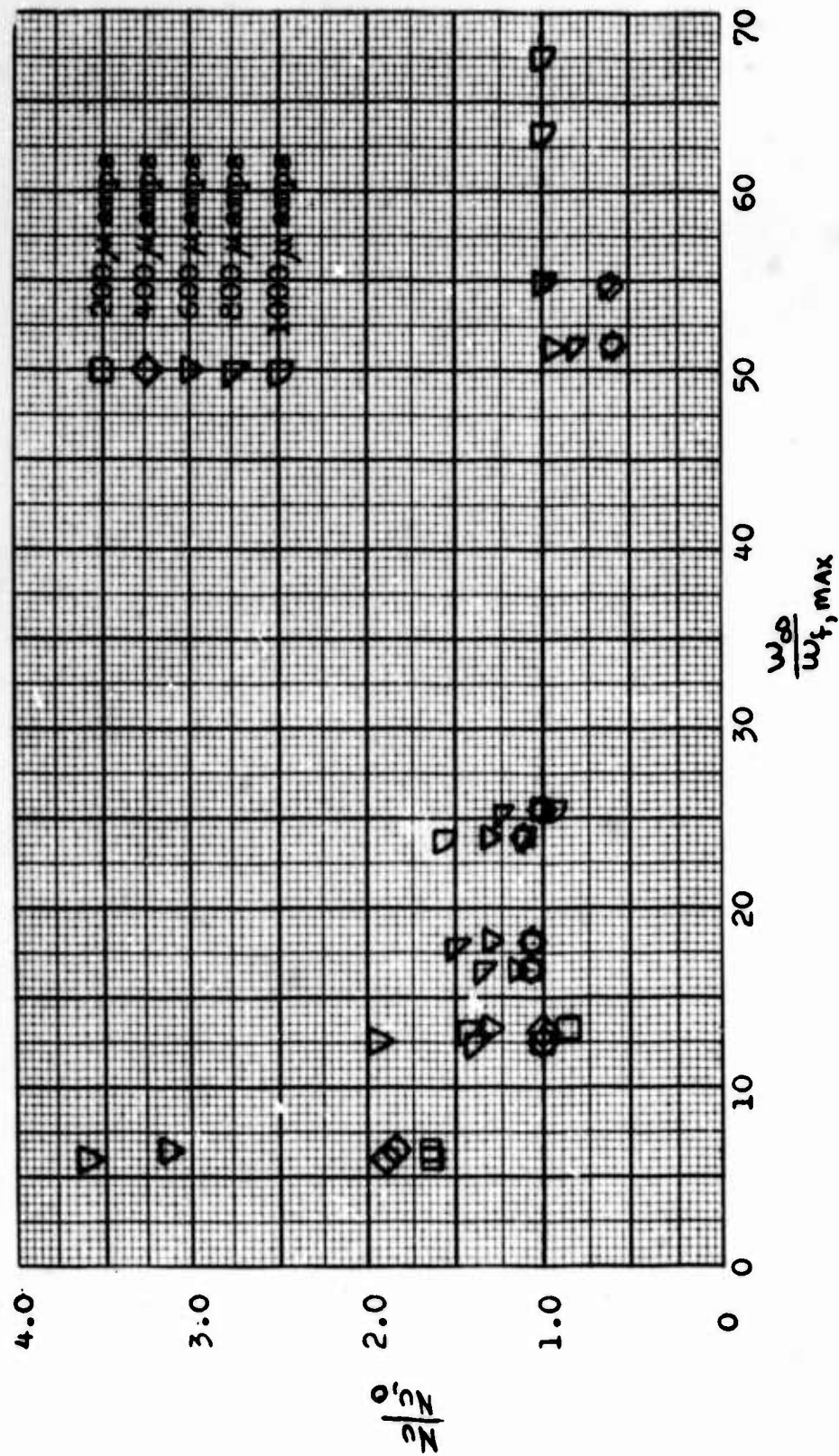
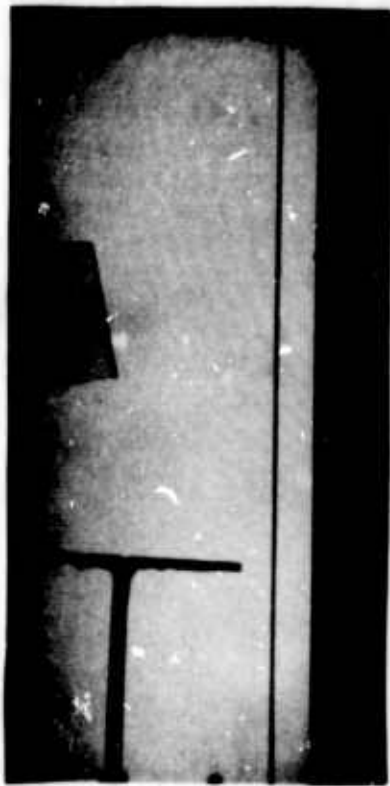


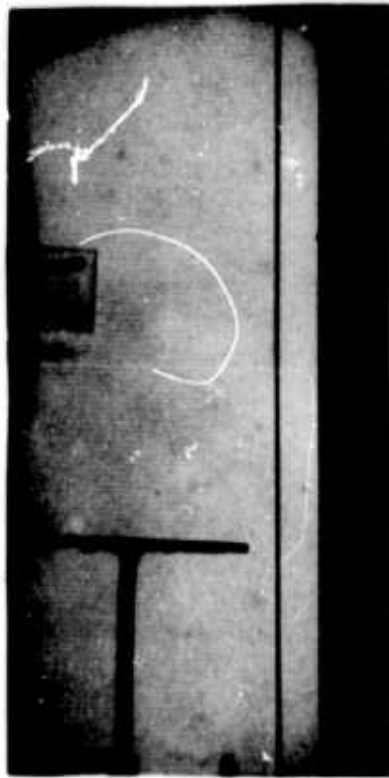
Fig. 23. A non-dimensional plot showing the effect of corona discharge at various free stream velocities. w_0 is the maximum free convective velocity at the same ΔT , subscript 0 indicates no current condition.



A. 0 kV $\Delta T = 79^{\circ}\text{F}$ 0 Microamps



B. 5.6 kV $\Delta T = 83^{\circ}\text{F}$ 200 Microamps



C. 5.7 kV $\Delta T = 80^{\circ}\text{F}$ 400 Microamps



D. 5.8 kV $\Delta T = 80^{\circ}\text{F}$ 600 Microamps

Fig. 24. Effects of corona discharge on the temperature profile on a flat plate in forced convection. Free stream velocity 5.9 feet per second, grid wires 0.006 inch diameter, grid-plate spacing 0.236 inches, wire-wire spacing $\frac{1}{8}$ inch, room temperature 76°F .

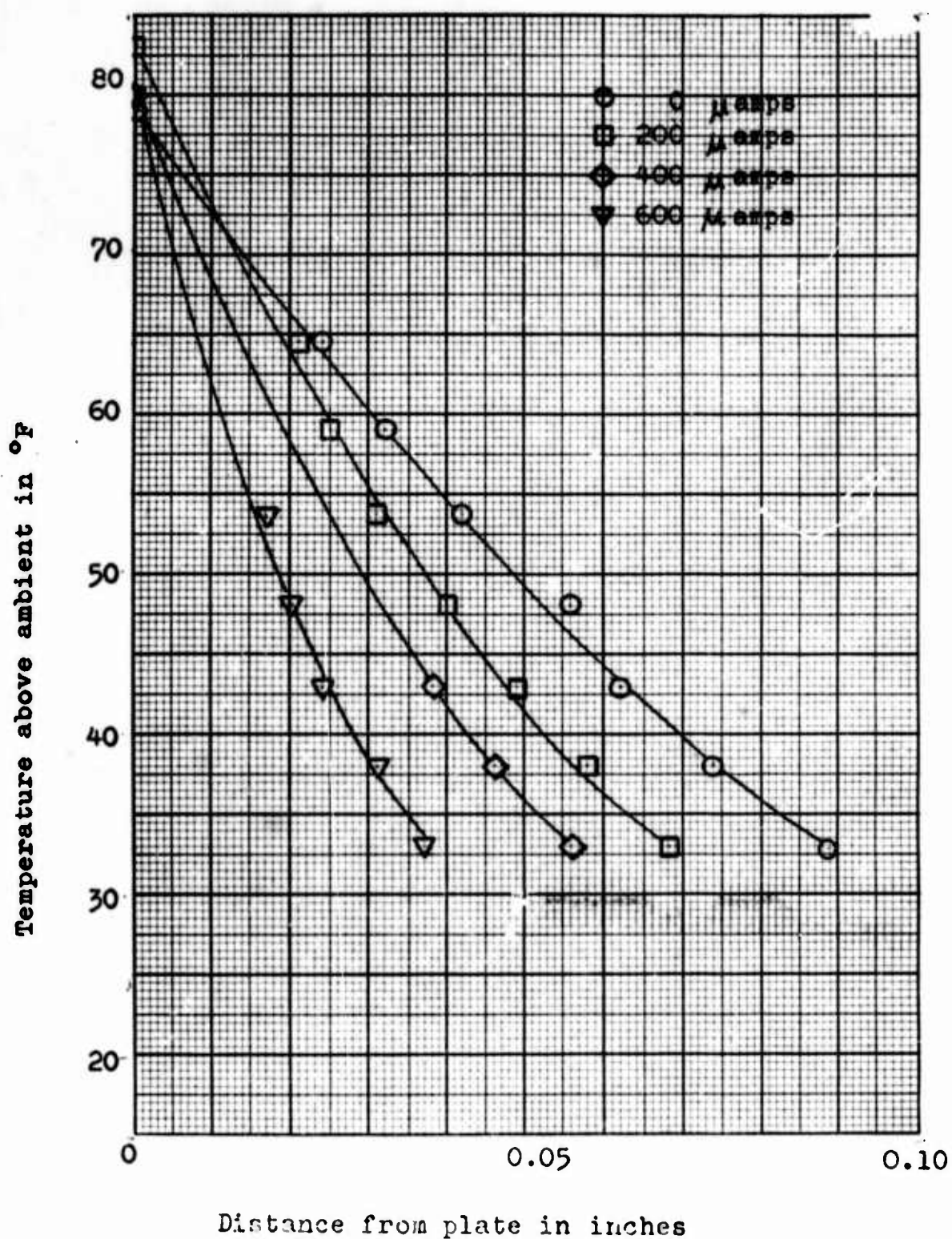


Fig. 25 Effects of corona discharge on the temperature profile 7 inches from the leading edge. Free stream velocity 5.9 feet per second, grid-plate spacing 0.236 inches, wire-wire spacing $\frac{1}{2}$ inch.

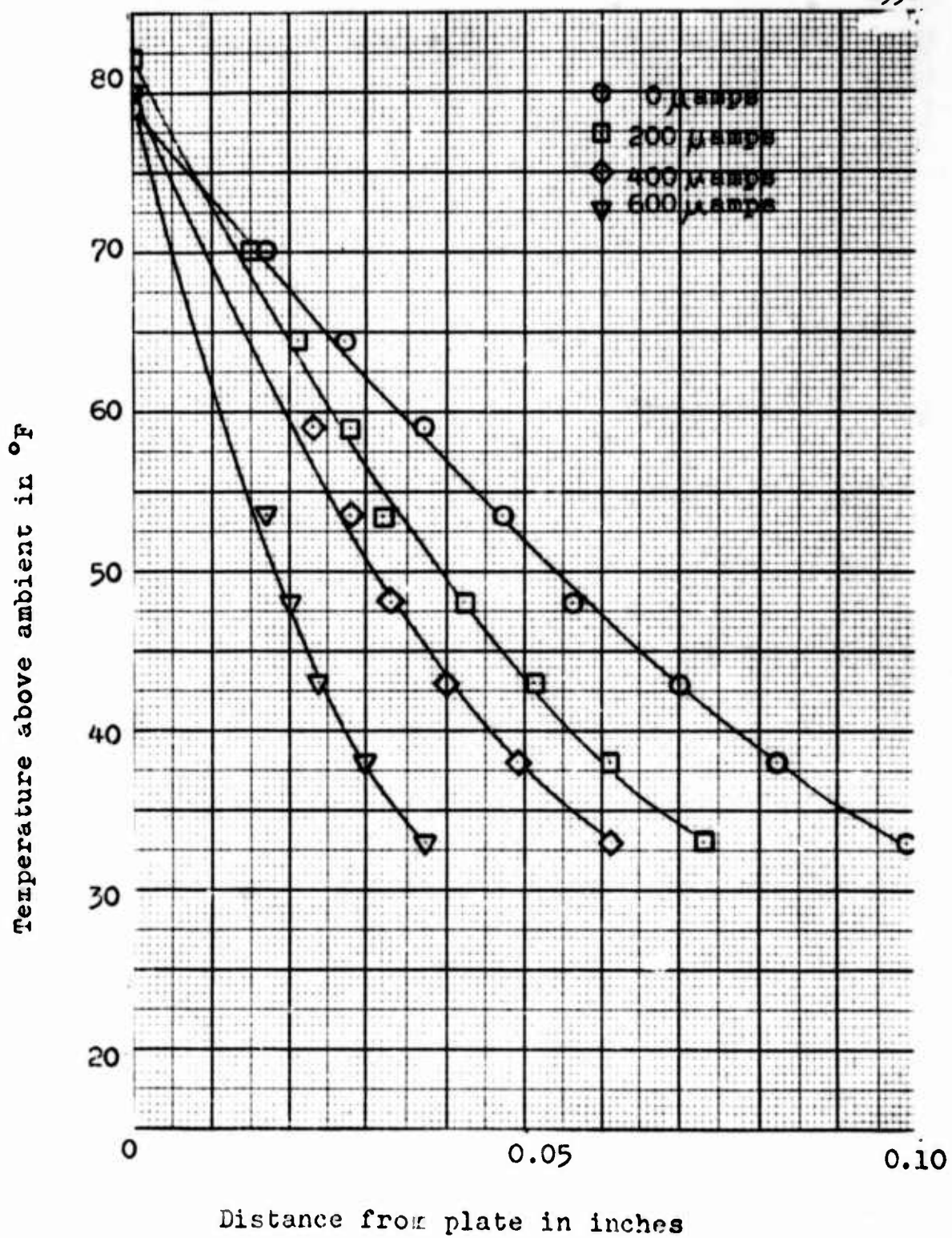
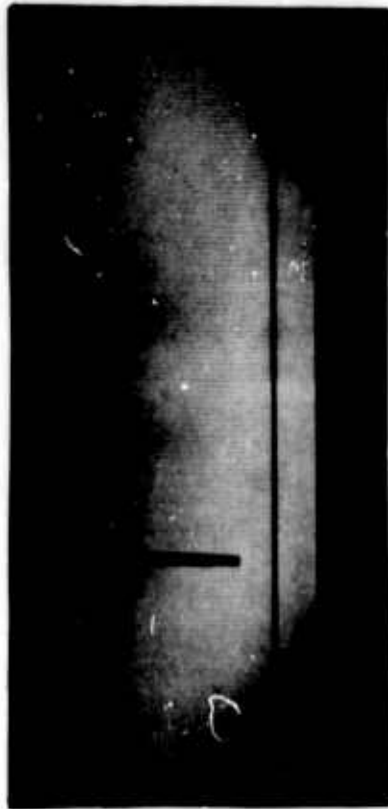
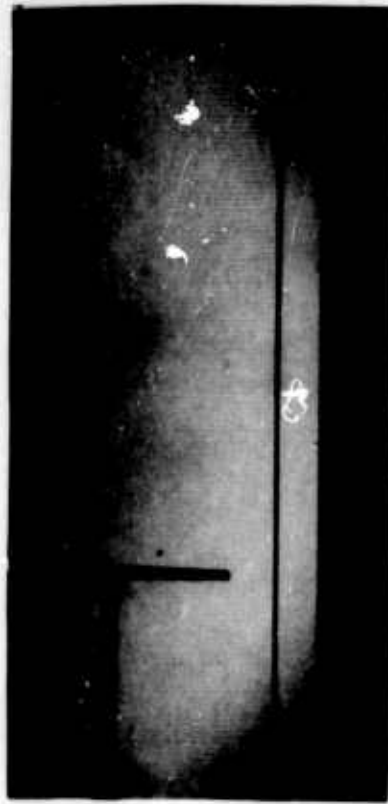


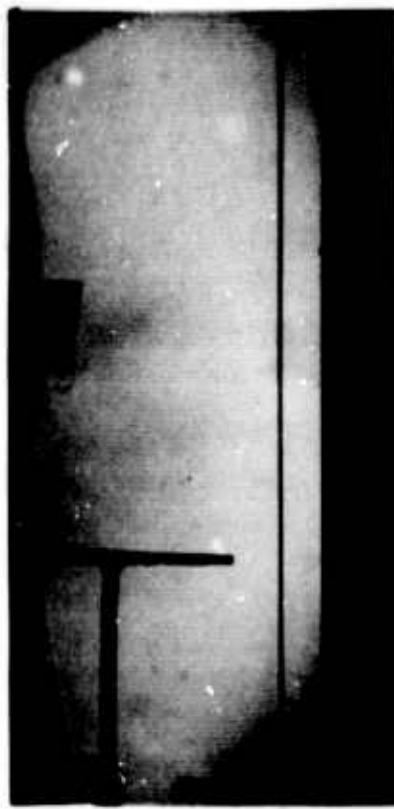
Fig. 26. Effects of corona discharge on the temperature profile 8 inches from the leading edge. Free stream velocity 5.9 feet per second, grid-plate spacing 0.236 inches, wire-wire spacing $\frac{1}{2}$ inch.



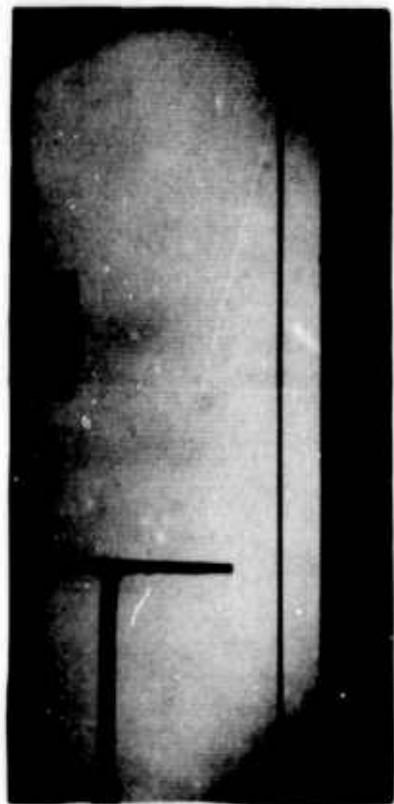
A. 0 KV $\Delta T = 82^{\circ}\text{F}$ 0 Microamps



B. 5.7 KV $\Delta T = 82^{\circ}\text{F}$ 200 Microamps

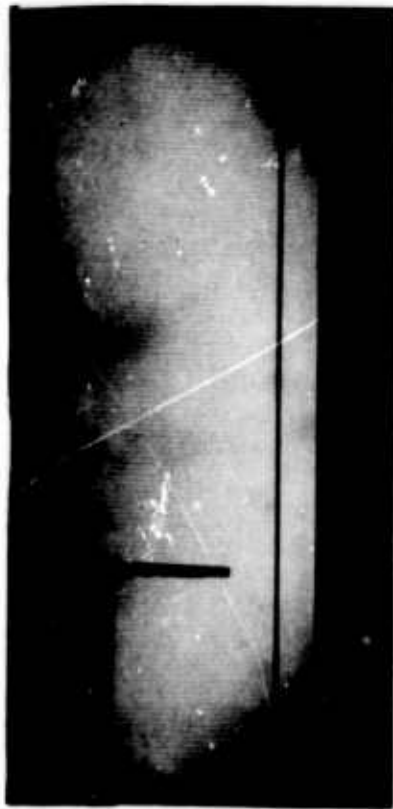


C. 5.8 KV $\Delta T = 82^{\circ}\text{F}$ 400 Microamps



D. 5.8 KV $\Delta T = 84^{\circ}\text{F}$ 600 Microamps

Fig. 27. Effects of corona discharge on the temperature profile on a flat plate in forced convection. Free stream velocity 12.2 feet per second, grid wires 0.006 inch diameter, grid-plate spacing 0.236 inches, wire-wire spacing $\frac{1}{8}$ inch, room temperature 72°F .



NO DATA

E. 5.9KV	T= 82°F	800 Microamps	P.	KV	T= °F	1000 Microamps
----------	---------	---------------	----	----	-------	----------------

Fig. 27 con't. Effects of corona discharge on the temperature profile on a flat plate in forced convection. Free stream velocity 12.2 feet per second, grid wires 0.006 inch diameter, grid-plate spacing 0.236 inches, wire-wire spacing $\frac{1}{4}$ inch, room temperature 72°F.

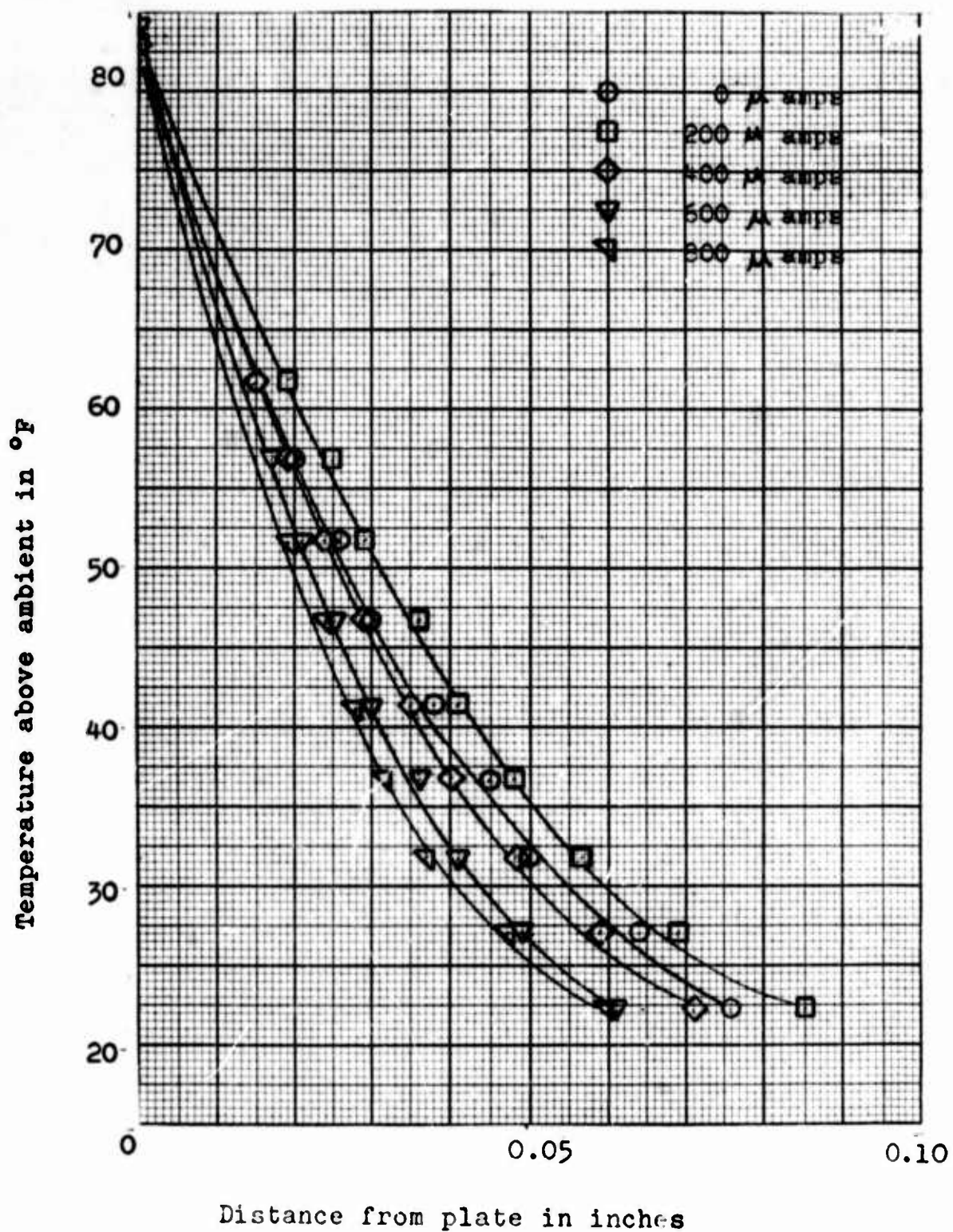


Fig. 28. Effects of corona discharge on the temperature profile 7 inches from the leading edge. Free stream velocity 12.2 feet per second, grid-plate spacing 0.236 inches, wire-wire spacing $\frac{1}{2}$ inch.

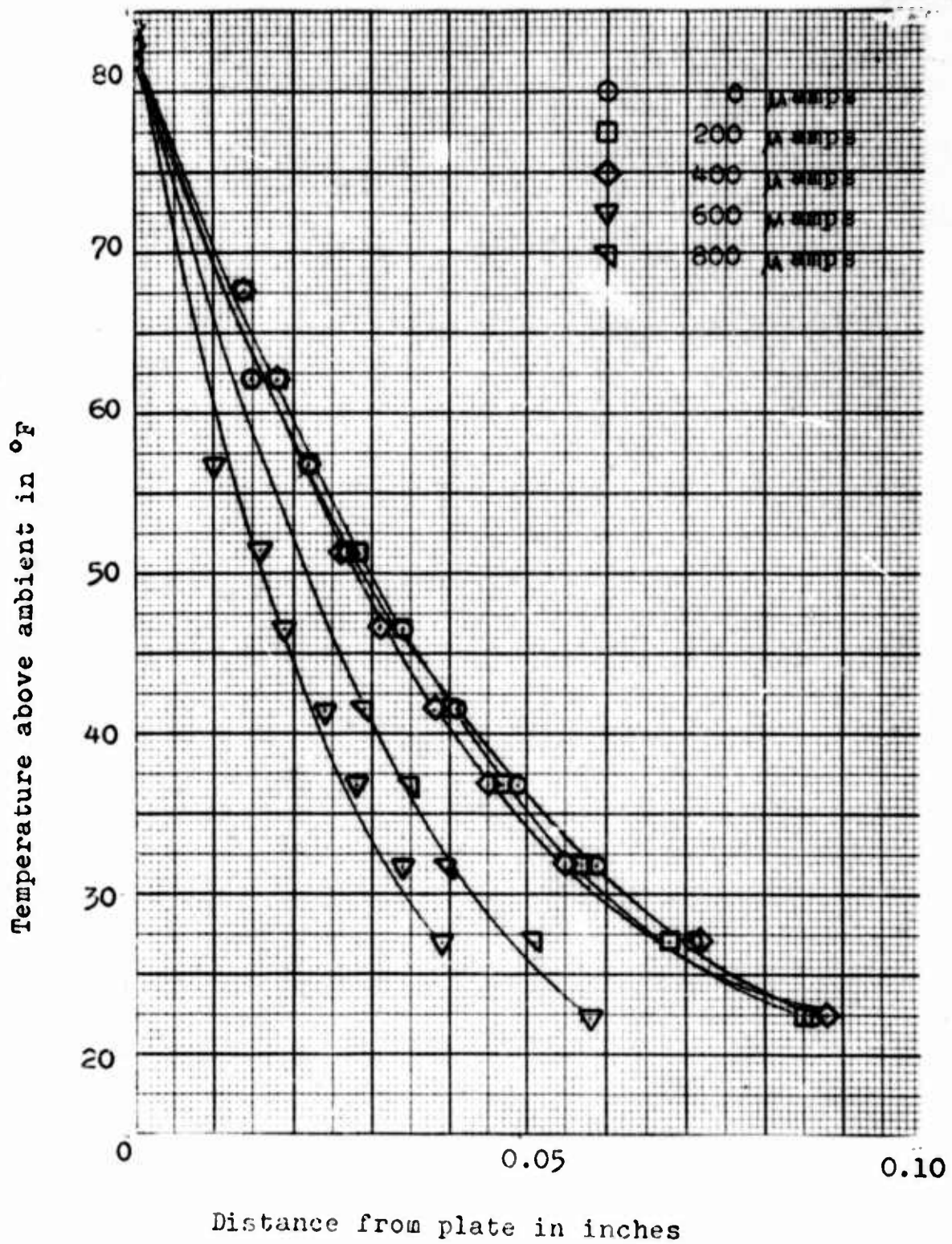
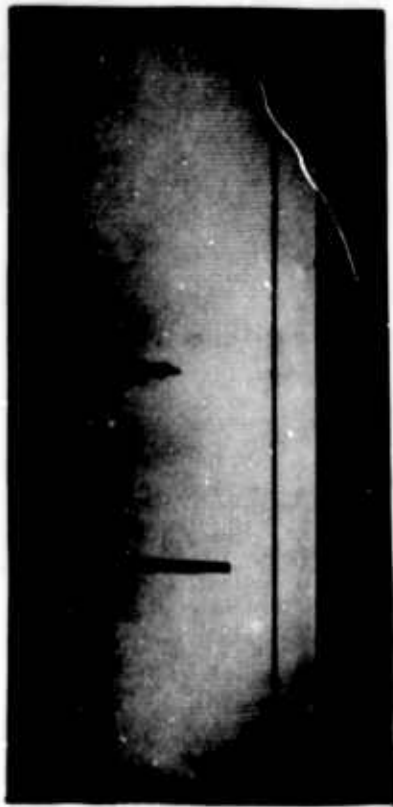
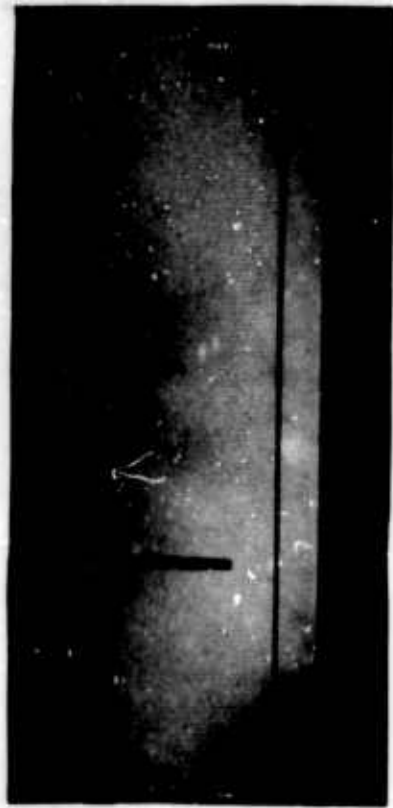


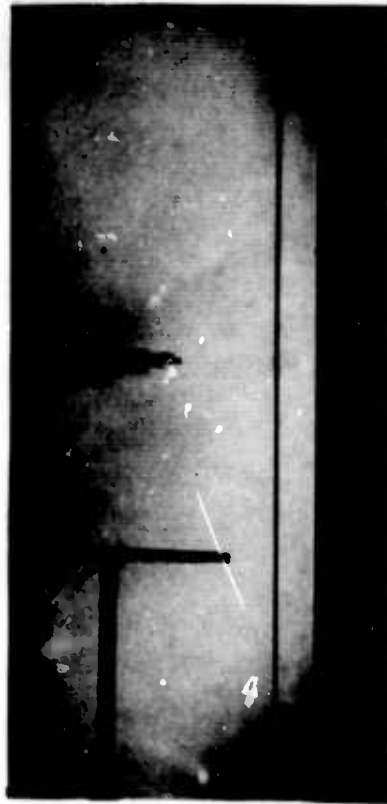
Fig. 29. Effects of corona discharge on the temperature profile 8 inches from the leading edge. Free stream velocity 12.2 feet per second, grid-plate spacing 0.236 inches, wire-wire spacing $\frac{1}{2}$ inch.



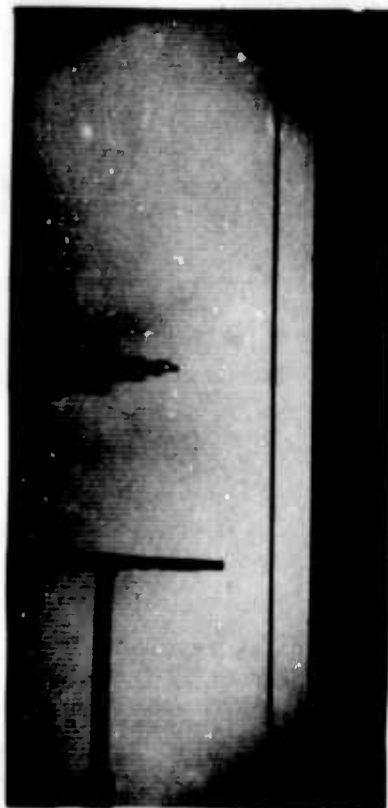
A. 0 KV $\Delta T = 78^{\circ}F$ 0 Microamps



B. 5.8 KV $\Delta T = 78^{\circ}F$ 200 Microamps

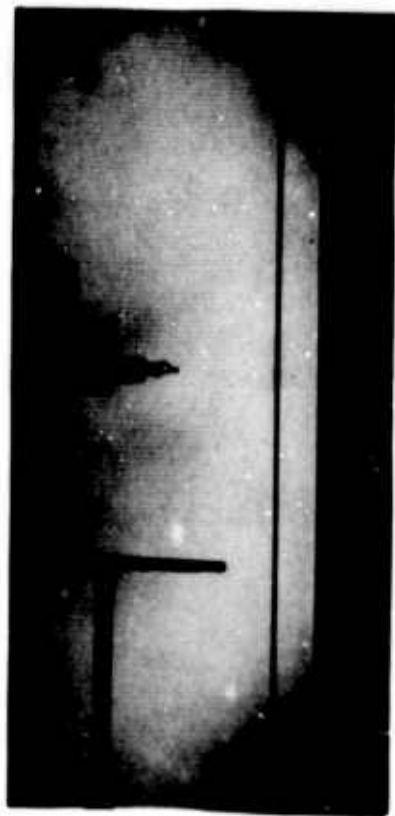


C. 5.9KV $\Delta T = 77^{\circ}F$ 400 Microamps



D. 6.0 KV $\Delta T = 78^{\circ}F$ 600 Microamps

Fig.30.. Effects of corona discharge on the temperature profile on a flat plate in forced convection. Free stream velocity 16.3 feet per second, grid wires 0.006 inch diameter, grid-plate spacing 0.236 inches, wire-wire spacing $\frac{1}{8}$ inch, room temperature $73^{\circ}F$.



NO DATA

E. 6.0KV T= 78°F 800 Microamps P. KV T= °F 1000 Microamps

Fig. 30-con't. Effects of corona discharge on the temperature profile on a flat plate in forced convection. Free stream velocity 16.3 feet per second, grid wires 0.006 inch diameter, grid-plate spacing 0.236 inches, wire-wire spacing $\frac{1}{8}$ inch, room temperature 73°F.

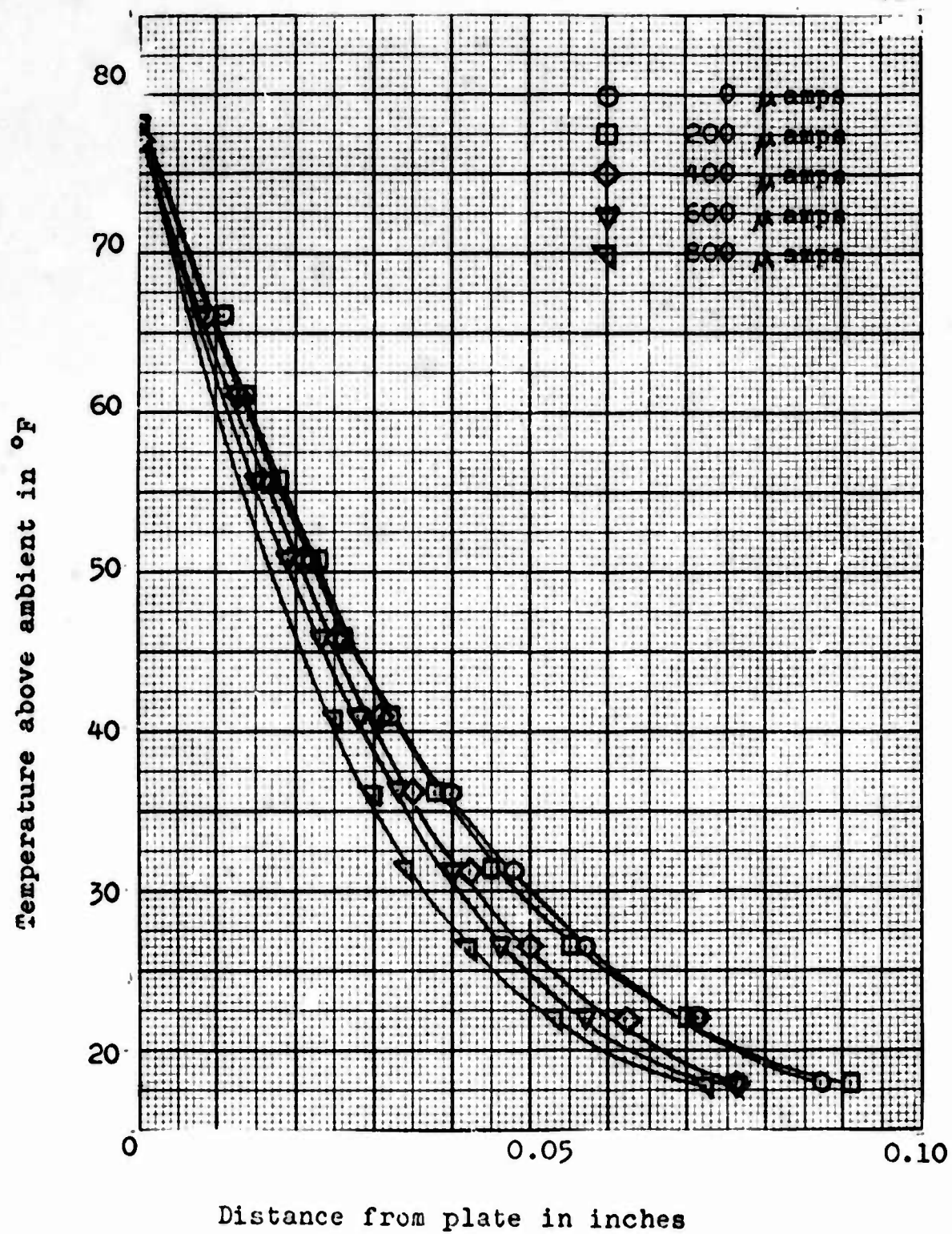


Fig. 31. Effects of corona discharge on the temperature profile 7 inches from the leading edge. Free stream velocity 16.3 feet per second, grid-plate spacing 0.236 inches, wire-wire spacing $\frac{1}{2}$ inch.

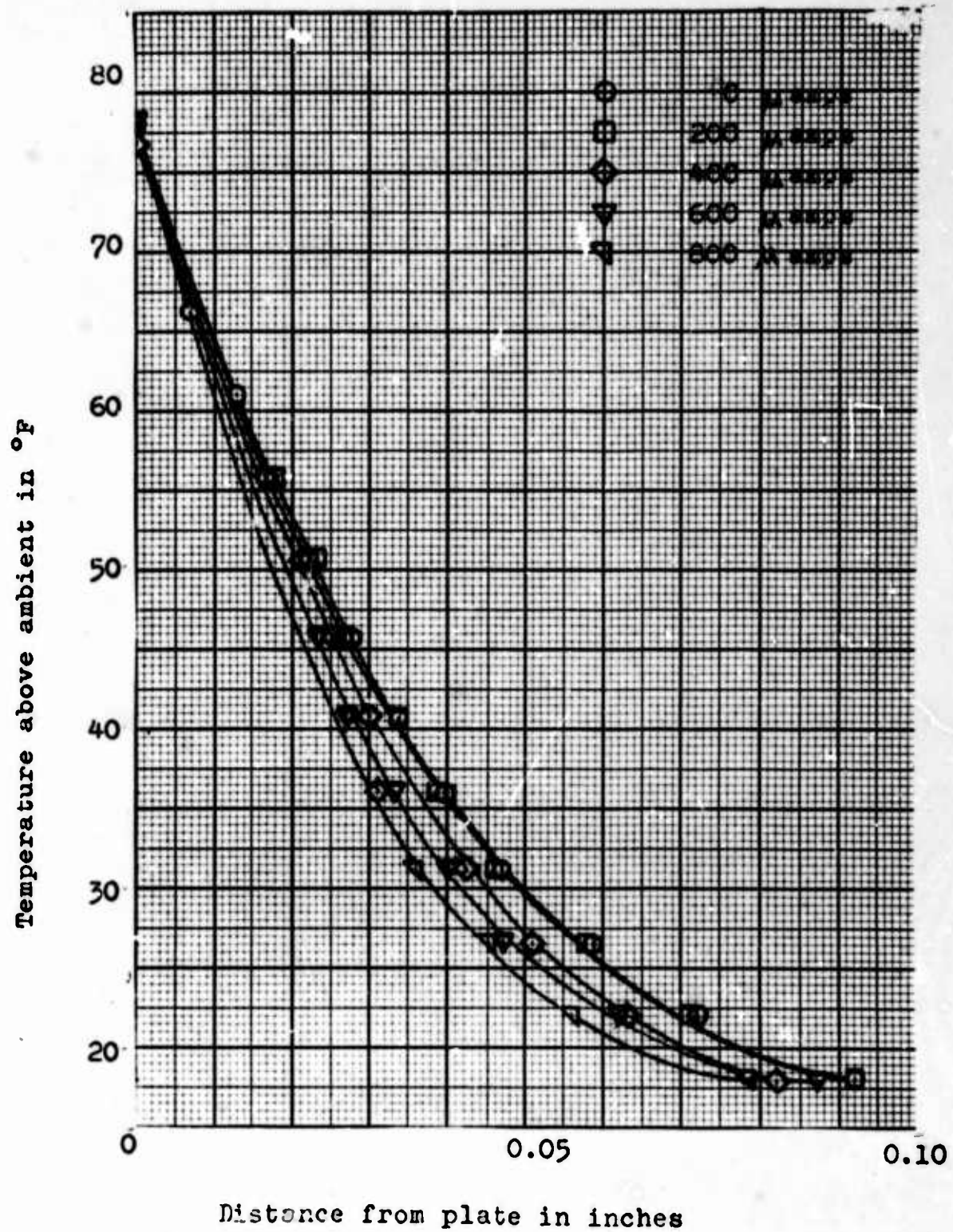
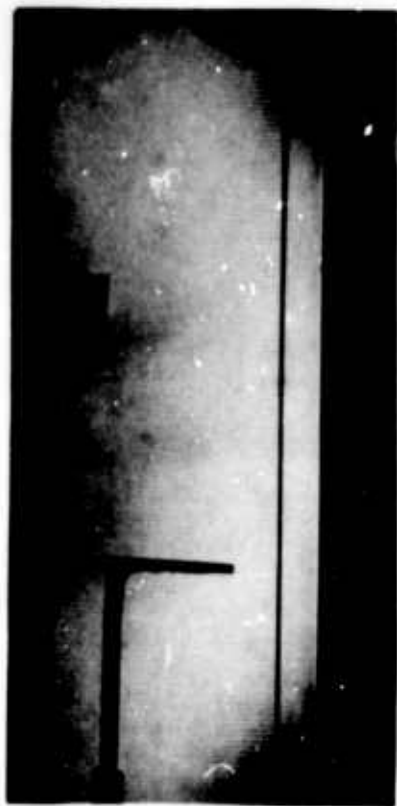


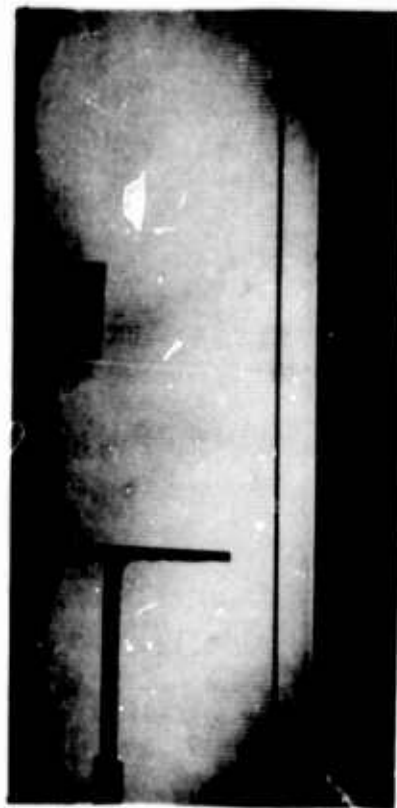
Fig. 32. Effects of corona discharge on the temperature profile 8 inches from the leading edge. Free stream velocity 16.3 feet per second, grid-plate spacing 0.236 inches, wire-wire spacing $\frac{1}{2}$ inch.



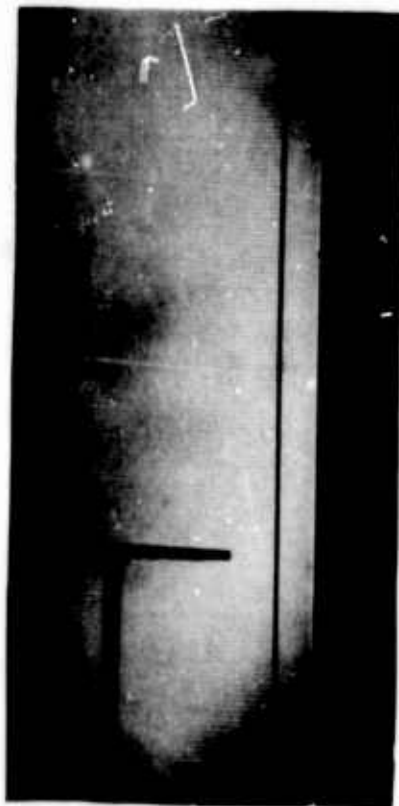
A. 0 KV $\Delta T = 76^{\circ}\text{F}$ 0 Microamps



B. 5.7KV $\Delta T = 76^{\circ}\text{F}$ 200 Microamps

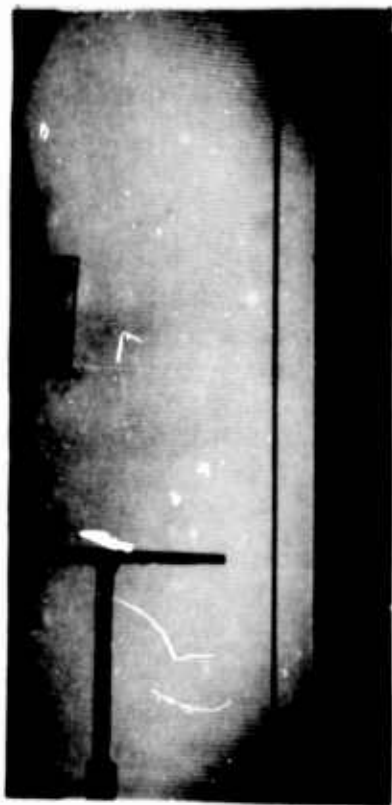


C. 5.8KV $\Delta T = 76^{\circ}\text{F}$ 400 Microamps

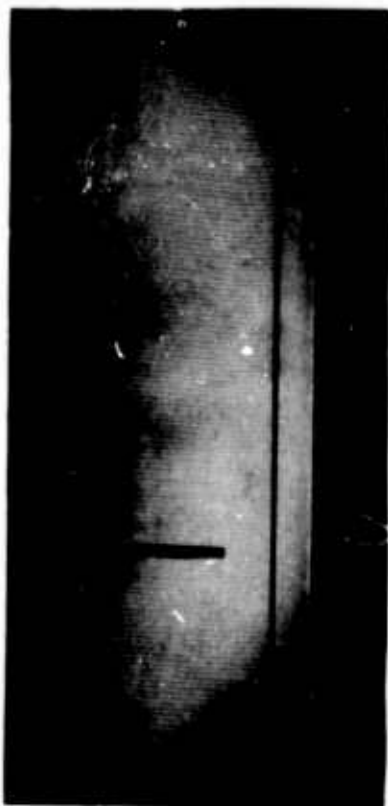


D. 5.9KV $\Delta T = 76^{\circ}\text{F}$ 600 Microamps

Fig. 33. Effects of corona discharge on the temperature profile on a flat plate in forced convection. Free stream velocity 23.4 feet per second, grid wires 0.006 inch diameter, grid-plate spacing 0.236 inches, wire-wire spacing $\frac{1}{4}$ inch, room temperature 73°F .



E. 6.0 KV T=76°F 800 Microamps



F. 6.0 KV T=76°F 1000 Microamps

Fig. 33. con't. Effects of corona discharge on the temperature profile on a flat plate in forced convection. Free stream velocity 23.4 feet per second, grid wires 0.006 inch diameter, grid-plate spacing 0.236 inches, wire-wire spacing $\frac{1}{2}$ inch, room temperature 73°F.

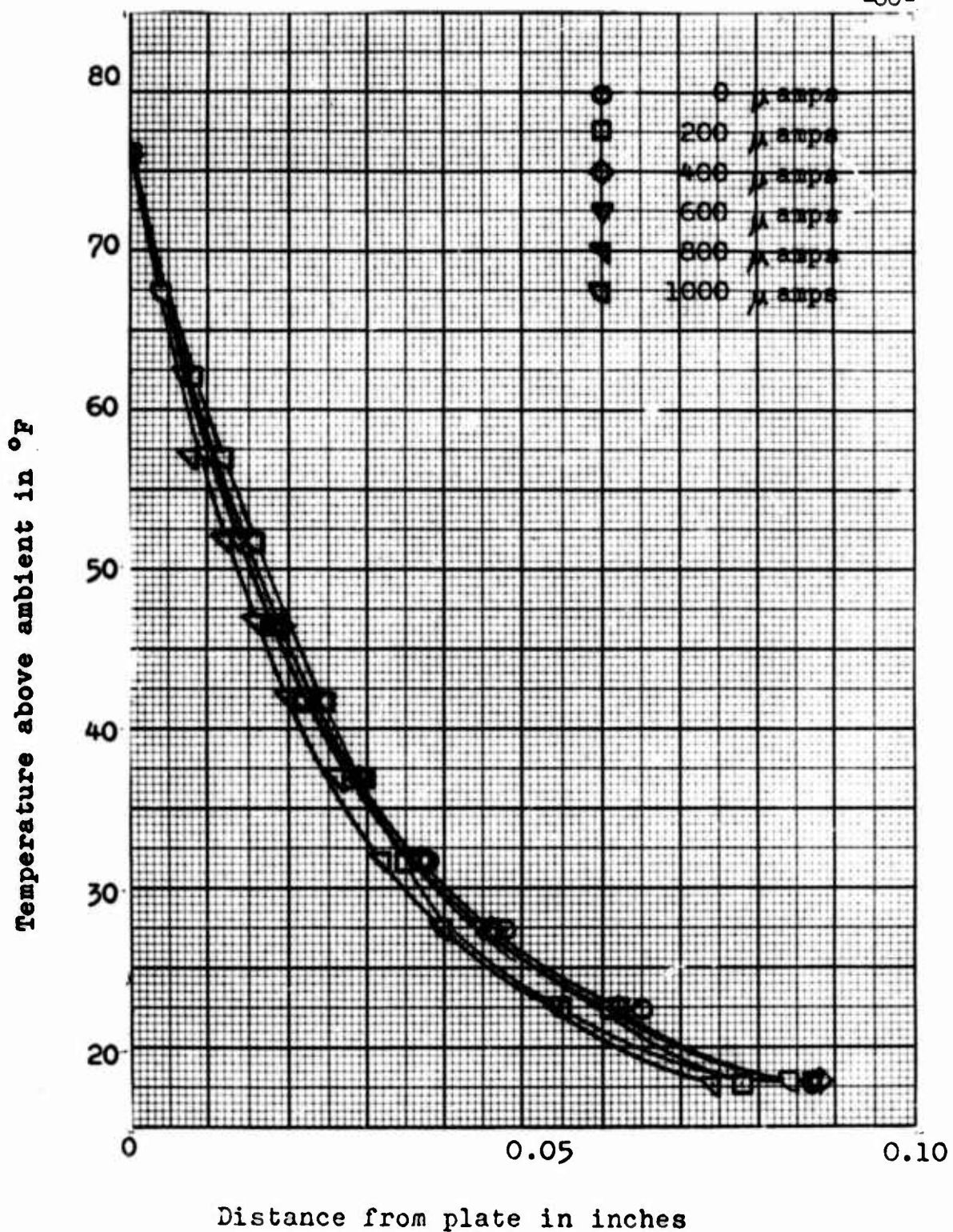


Fig. 34. Effects of corona discharge on the temperature profile 7 inches from the leading edge. Free stream velocity 23.4 feet per second, grid-plate spacing 0.236 inches, wire-wire spacing $\frac{1}{2}$ inch.

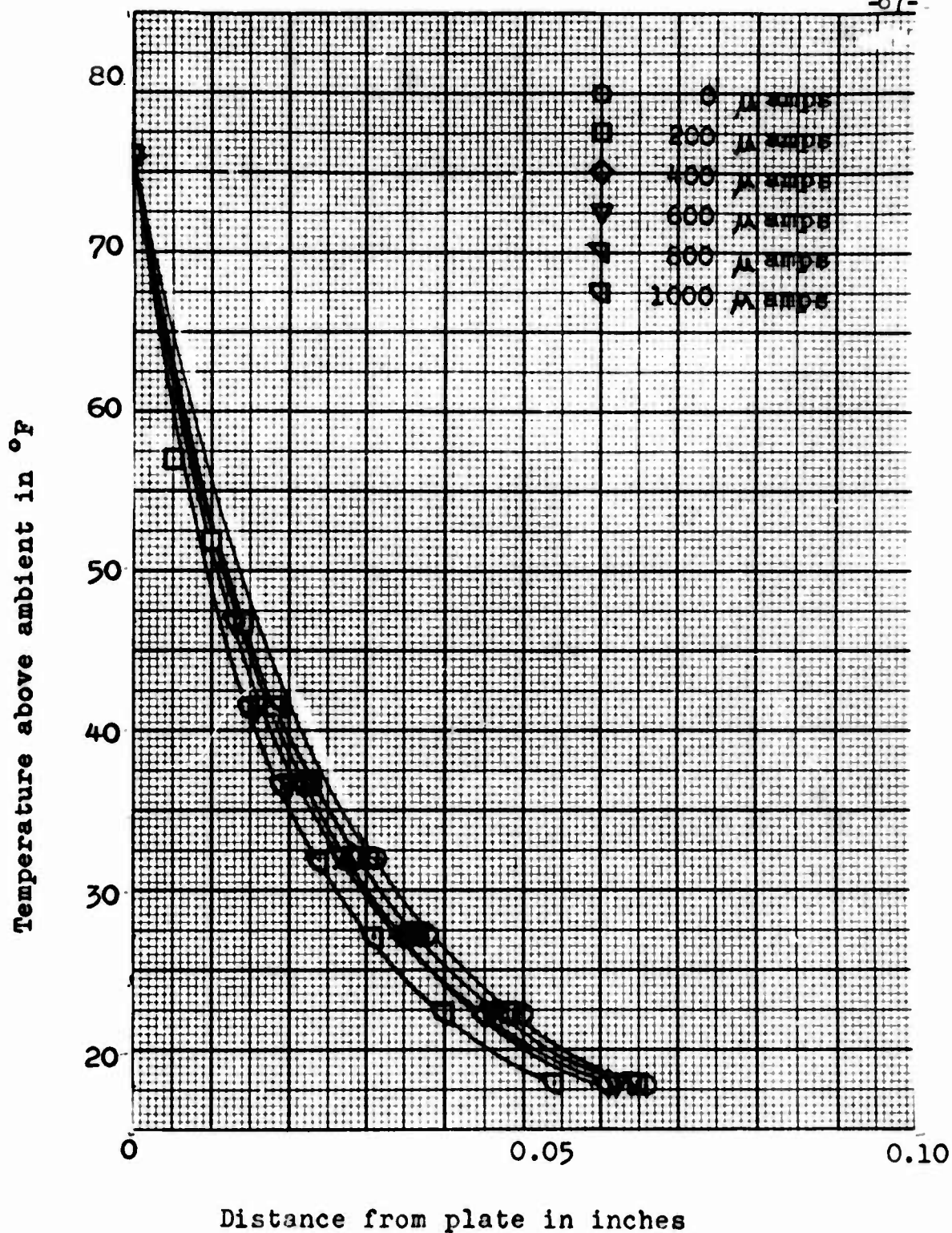
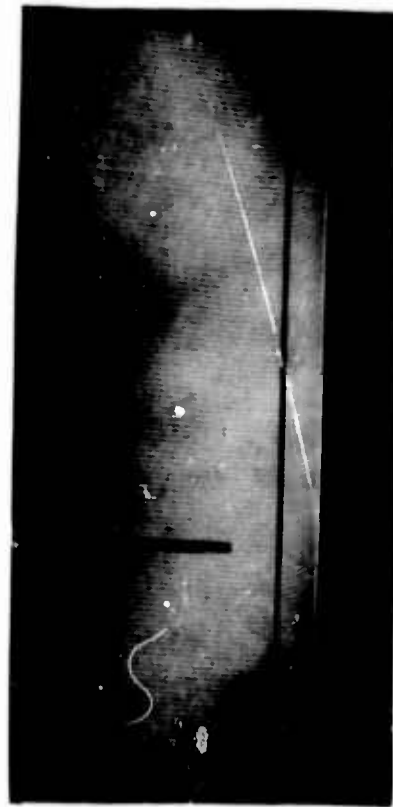


Fig. 35. Effects of corona discharge on the temperature profile 8 inches from the leading edge. Free stream velocity 23.4 feet per second, grid-plate spacing 0.236 inches, wire-wire spacing $\frac{1}{2}$ inch.

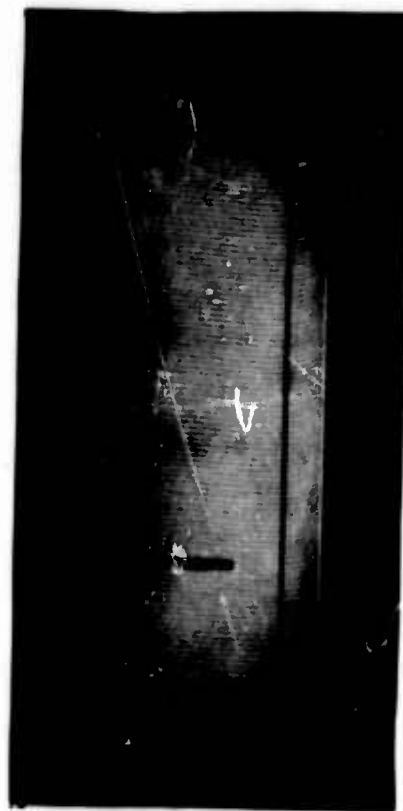


A. 0 KV $\Delta T = 78^\circ F$ 0 Microamps

NO DATA

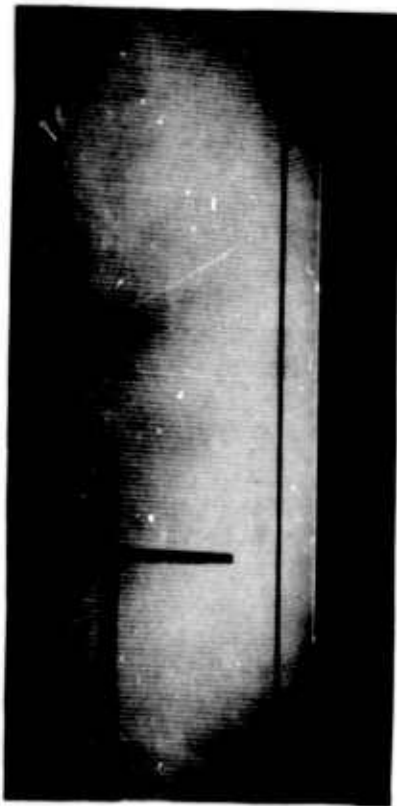


C. 5.8 KV $\Delta T = 78^\circ F$ 400 Microamps

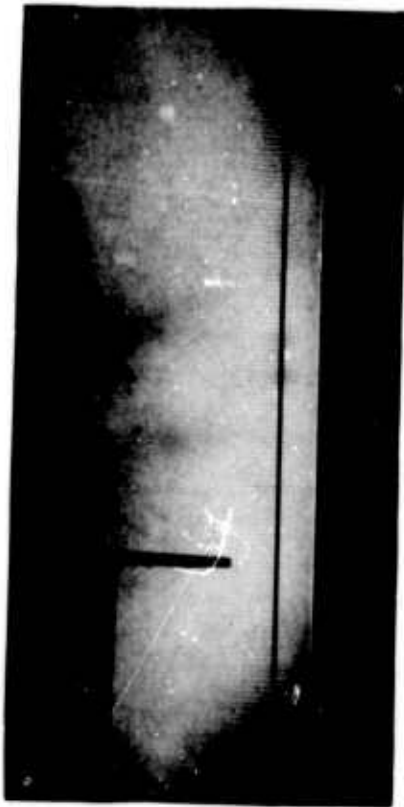


D. 5.9 KV $\Delta T = 78^\circ F$ 600 Microamps

Fig. 36. Effects of corona discharge on the temperature profile on a flat plate in forced convection. Free stream velocity 50.6 feet per second, grid wires 0.006 inch diameter, grid-plate spacing 0.236 inches, wire-wire spacing $\frac{1}{8}$ inch, room temperature $73^\circ F$.



E. 6.0KV T= 78°F 800 Microamps



F. 6.0KV T= 78°F 1000 Microamps

Fig. 36.con't. Effects of corona discharge on the temperature profile on a flat plate in forced convection. Free stream velocity 50.6 feet per second, grid wires 0.006 inch diameter, grid-plate spacing 0.236 inches, wire-wire spacing $\frac{1}{8}$ inch, room temperature 73°F.

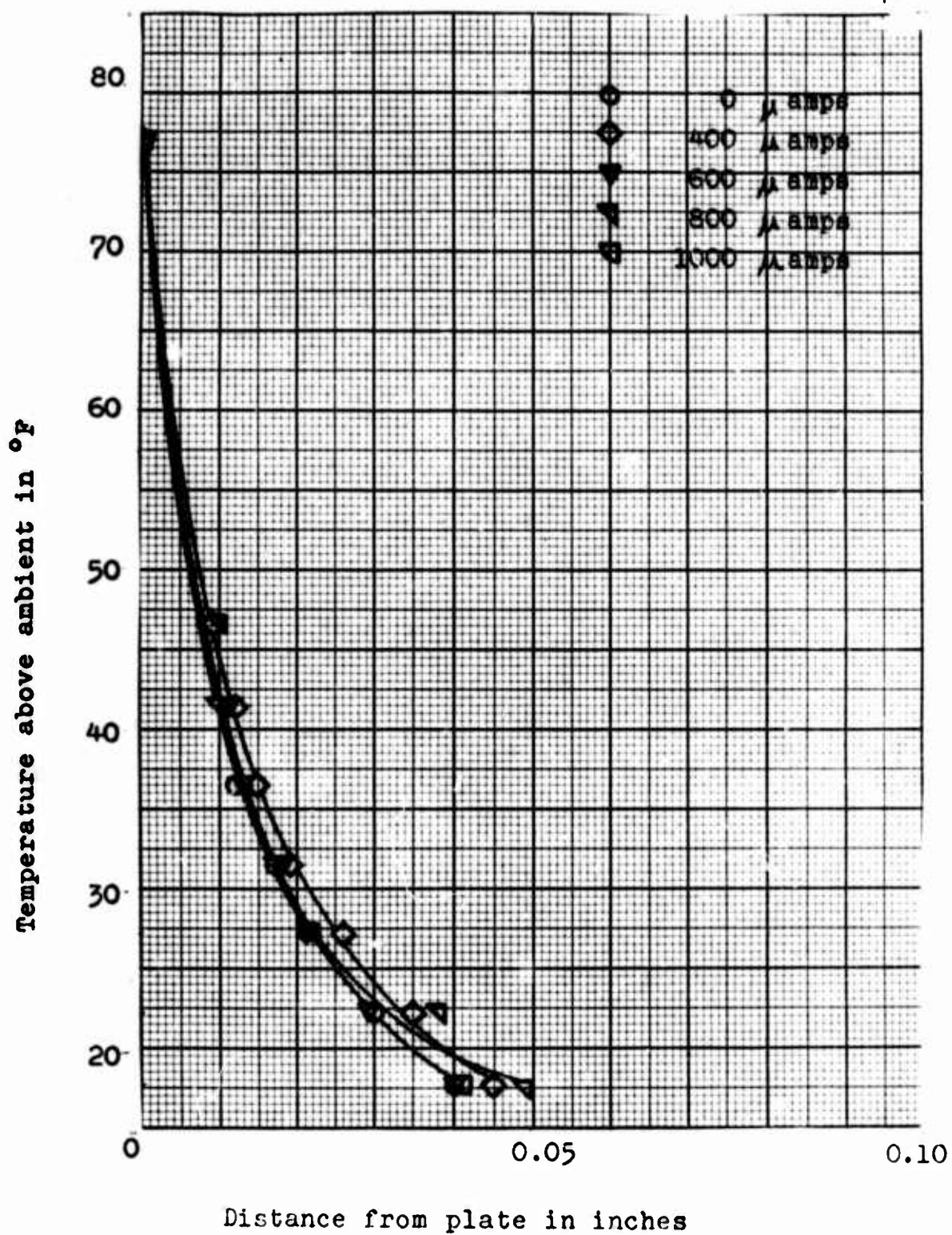


Fig.37. Effects of corona discharge on the temperature profile 7 inches from the leading edge. Free stream velocity 50.6 feet per second, grid-plate spacing 0.236 inches, wire-wire spacing $\frac{1}{2}$ inch.

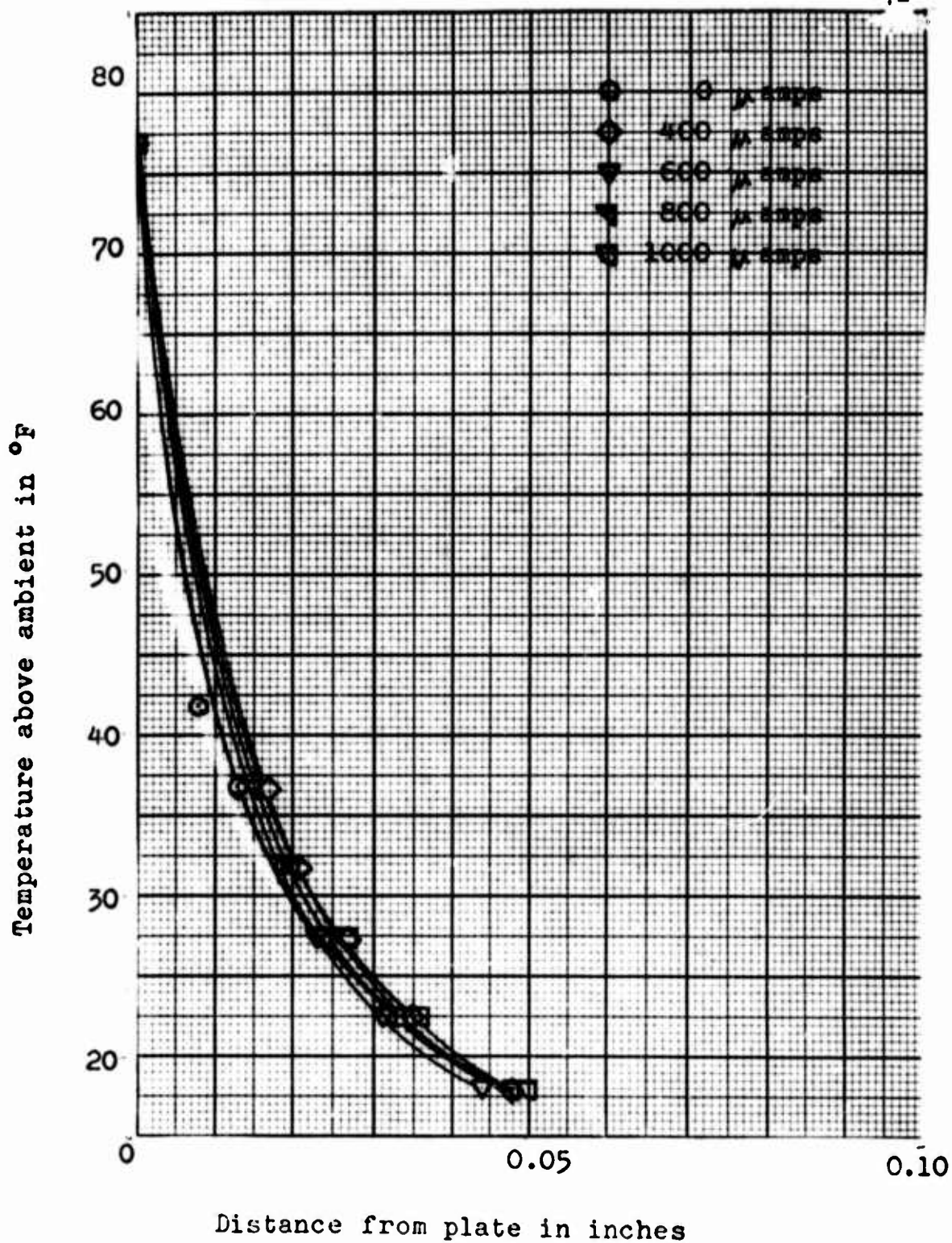
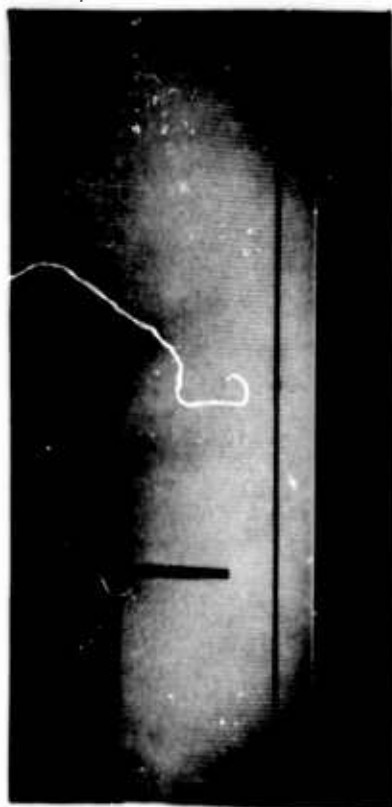
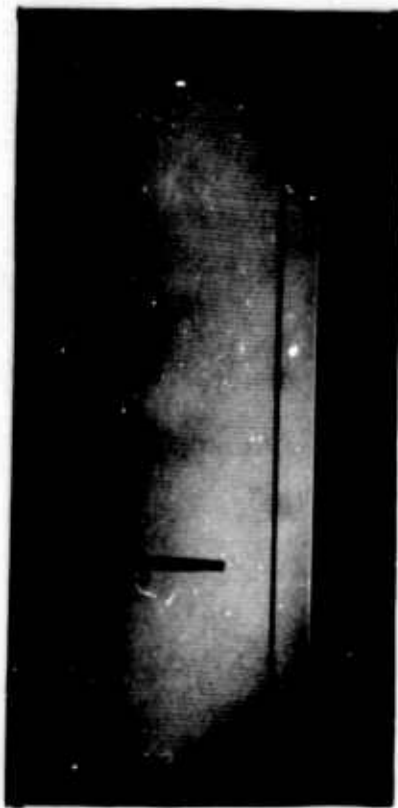


Fig. 38. Effects of corona discharge on the temperature profile 8 inches from the leading edge. Free stream velocity 50.6 feet per second, grid-plate spacing 0.236 inches, wire-wire spacing $\frac{1}{2}$ inch.



A. 0 KV T=78°F 0 Microamps



B. 6.0 KV T=78°F 1000 Microamps

Fig. 39. Effects of corona discharge on the temperature profile on a flat plate in forced convection.
Free stream velocity 62.5 feet per second, grid wires 0.006 inch diameter, grid-plate spacing 0.236 inches, wire-wire spacing $\frac{1}{2}$ inch, room temperature 73°F.

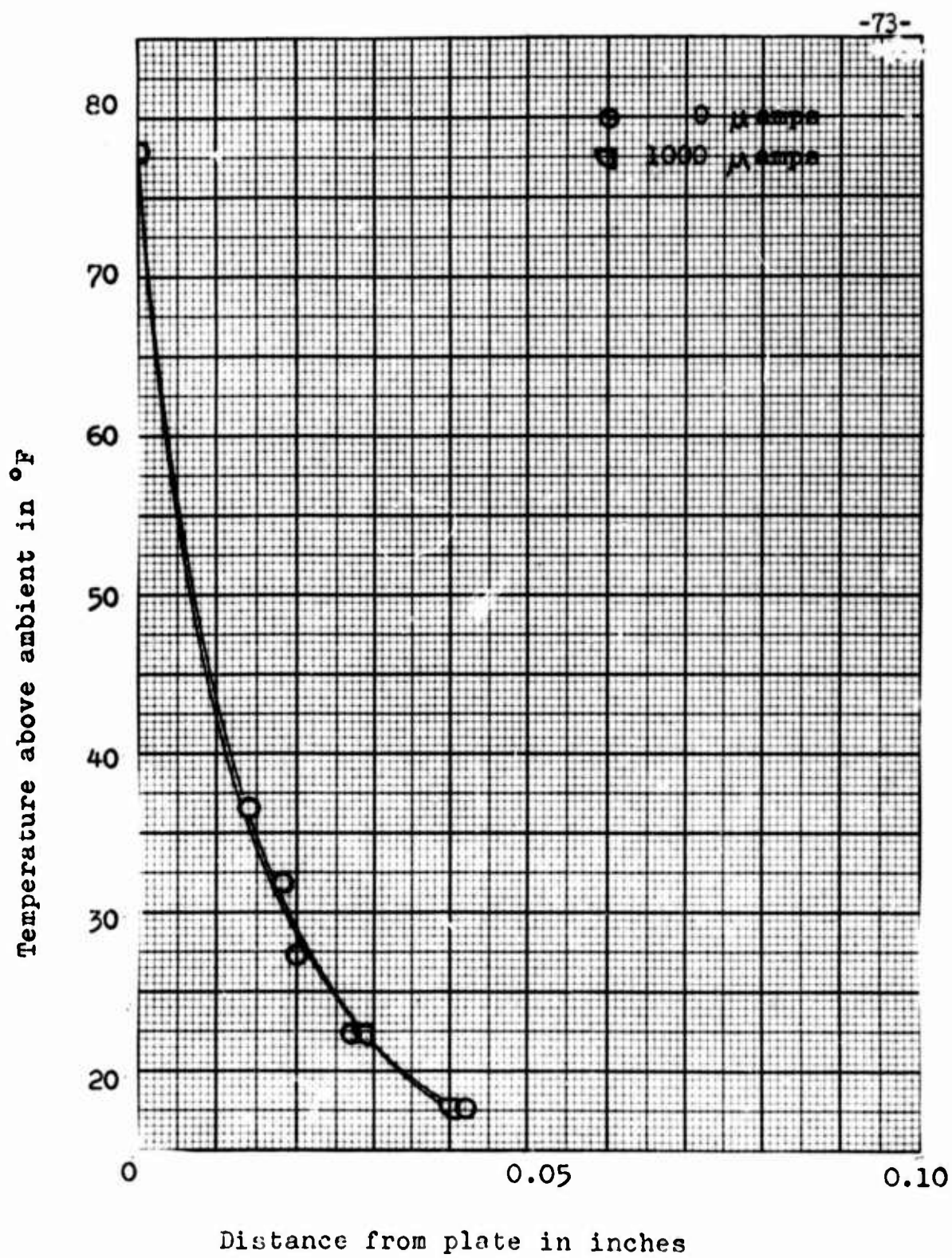


Fig.40. Effects of corona discharge on the temperature profile 7 inches from the leading edge. Free stream velocity 62.5 feet per second, grid-plate spacing 0.256 inches, wire-wire spacing $\frac{1}{2}$ inch.

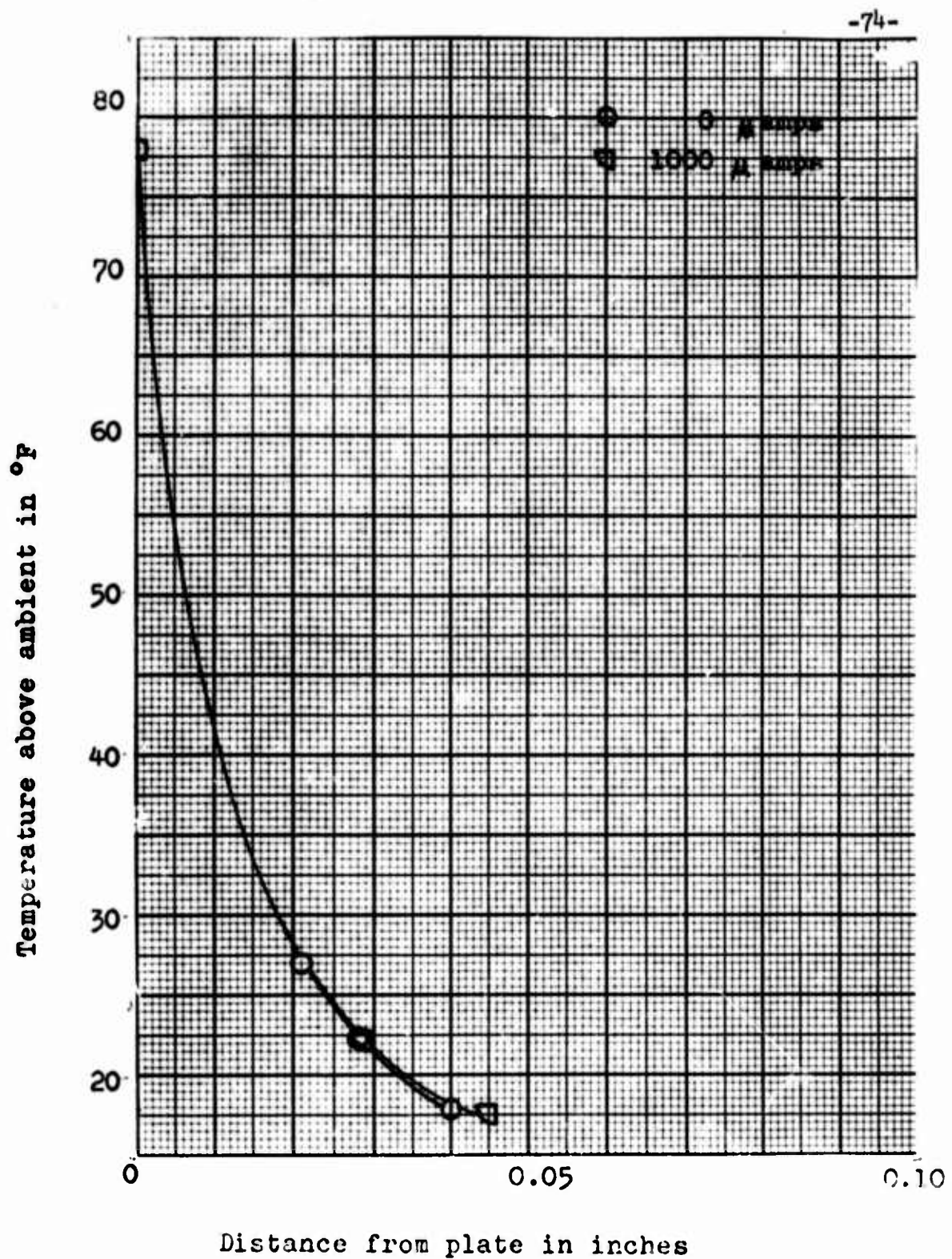


Fig. 41. Effects of corona discharge on the temperature profile 8 inches from the leading edge. Free stream velocity 62.5 feet per second, grid-plate spacing 0.236 inches, wire-wire spacing $\frac{1}{2}$ inch.

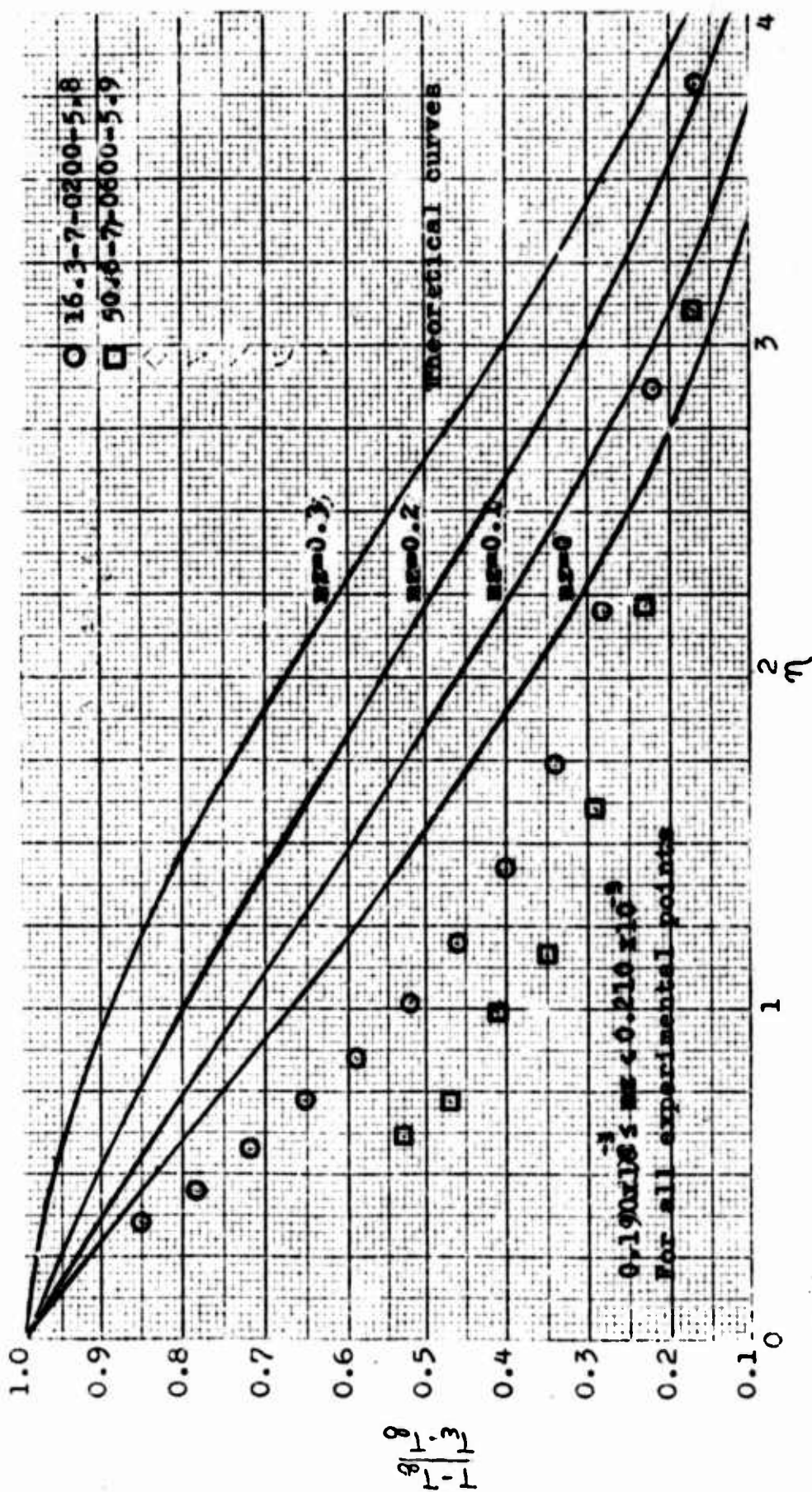


Fig. 42 . Temperature profiles for various values of m . The experimental points are designated by a number indicating free stream velocity (ft. per sec.)-distance from leading edge(inches)-corona current (μ amps)-grid voltage(kilovolts).

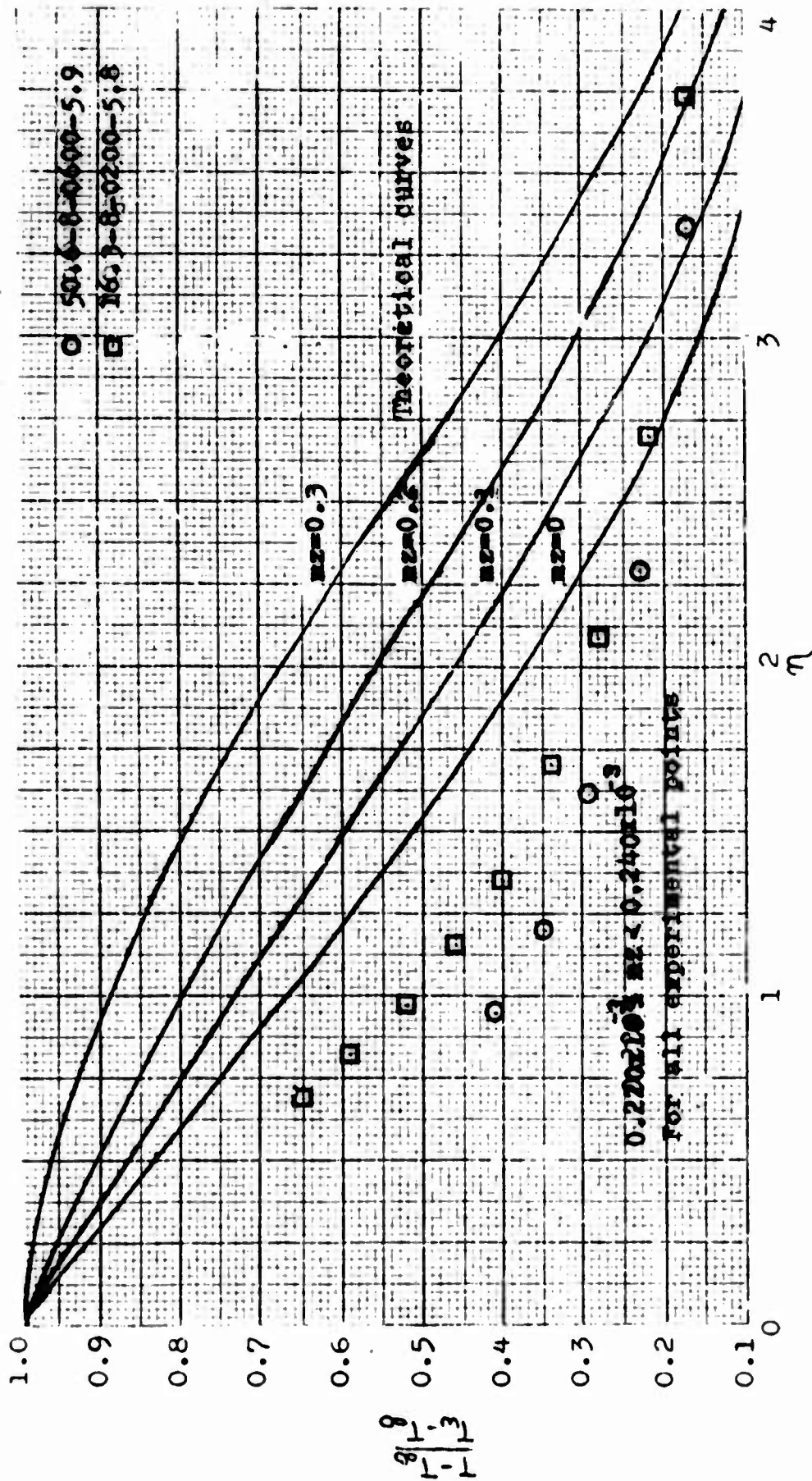


Fig. 47. Temperature profiles for various values of m_z . The experimental points are designated by a number indicating free stream velocity (ft. per sec.)-distance from leading edge (inches)-corona current (μ amps)-grid voltage (kilovolts).

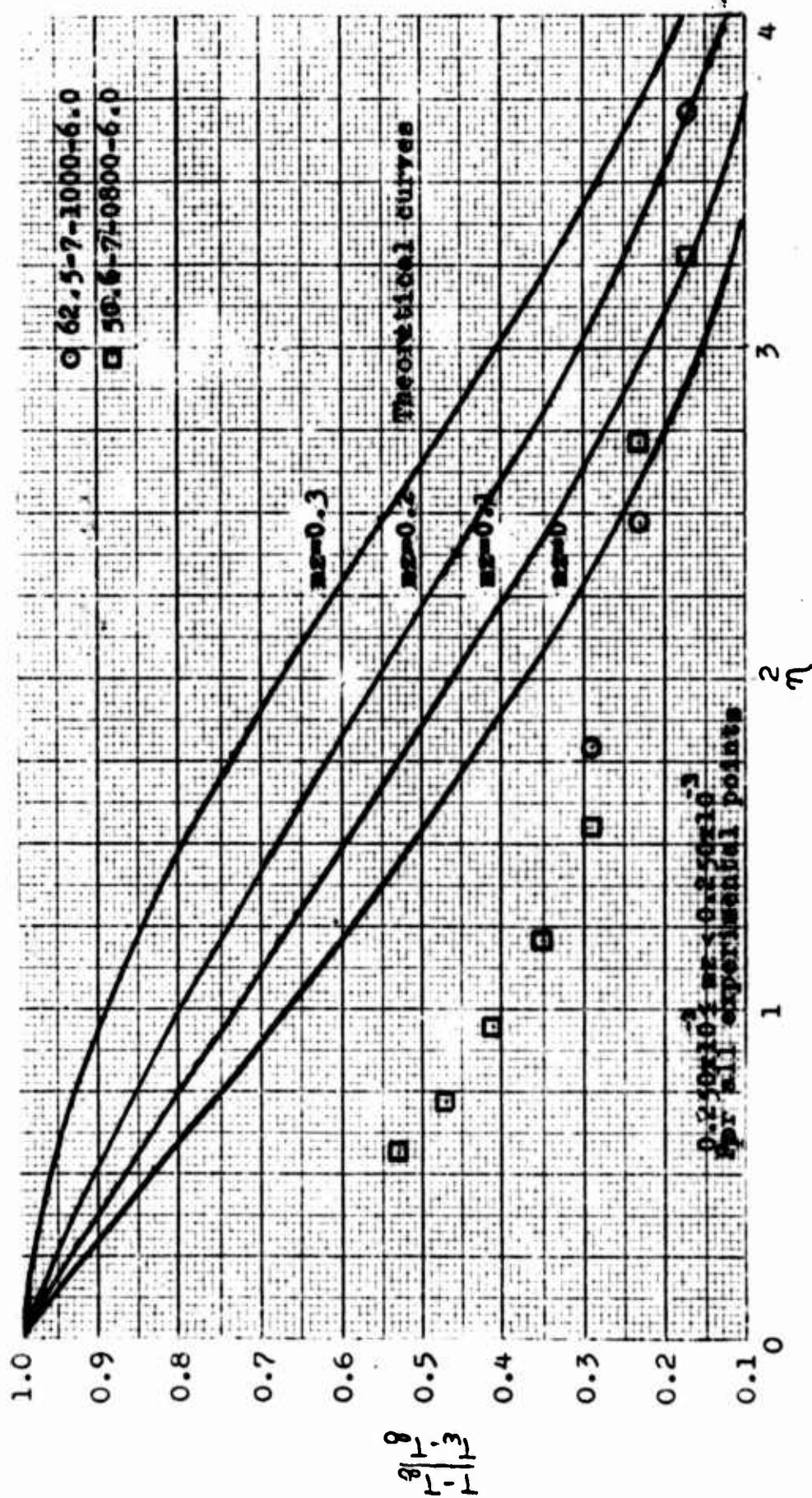


Fig. 44 . Temperature profiles for various values of m . The experimental points are designated by a number indicating free stream velocity (ft. per sec.)-distance from leading edge(inches)-corona current (μ amps)-grid voltage(kilovolts).

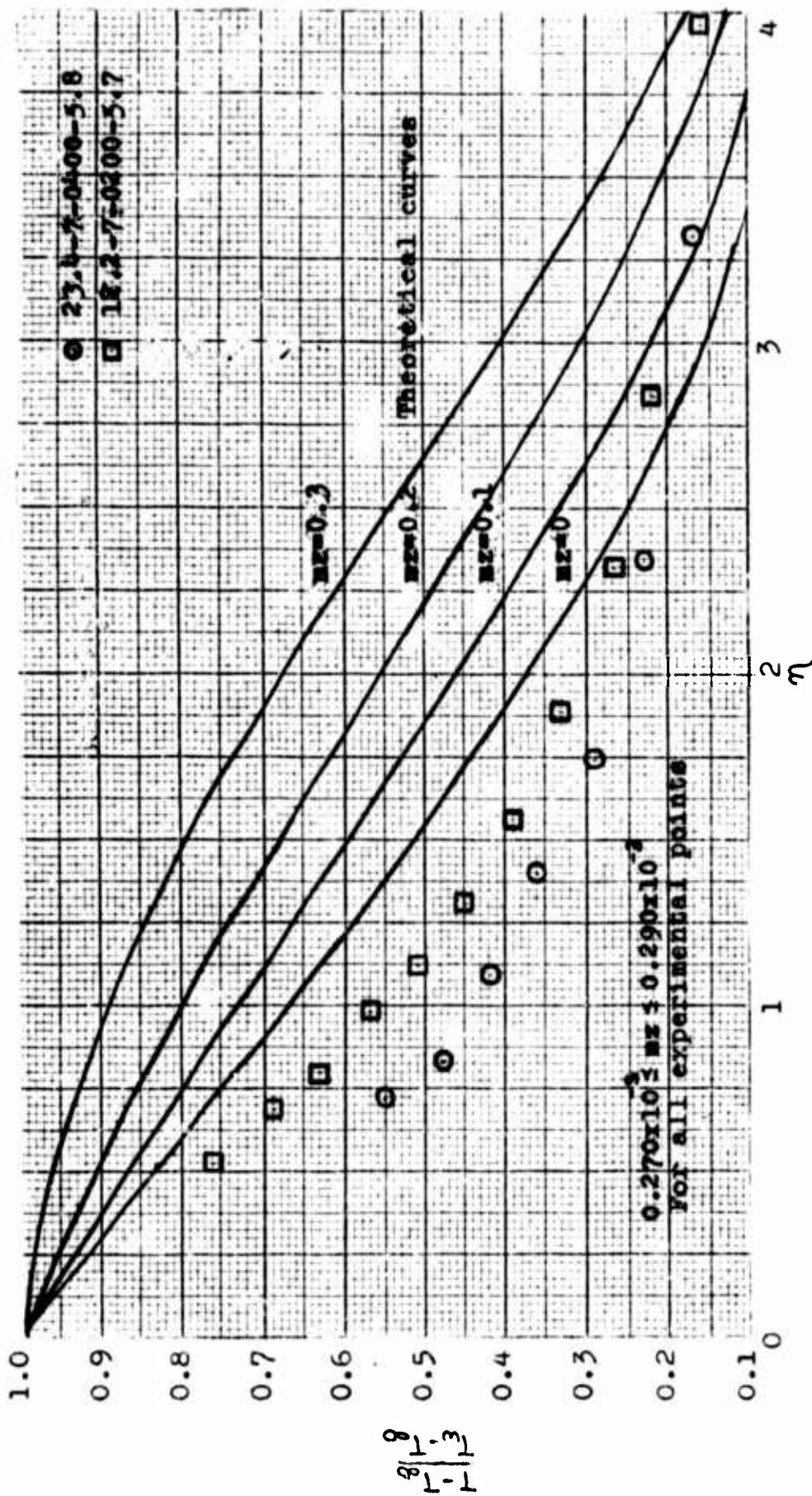


Fig.45 . Temperature profiles for various values of rz . The experimental points are designated by a number indicating free stream velocity (ft. per sec.)-distance from leading edge (inches)-corona current (μ amps)-grid voltage(kilovolts).

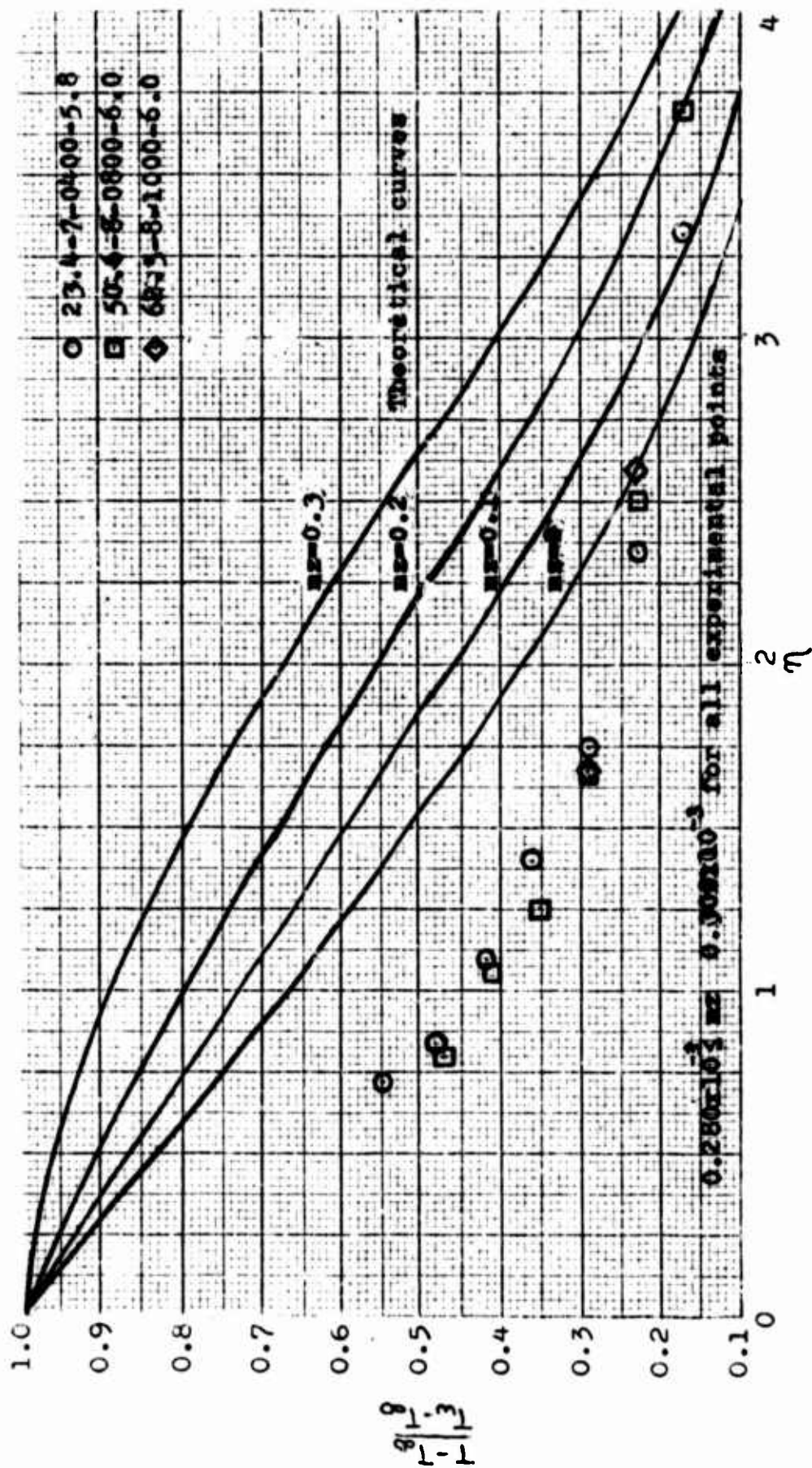


Fig. 46. Temperature profiles for various values of m_z . The experimental points are designated by a number indicating free stream velocity (ft. per sec.)-distance from leading edge (inches)-corona current (μ amps)-grid voltage (kilovolts).

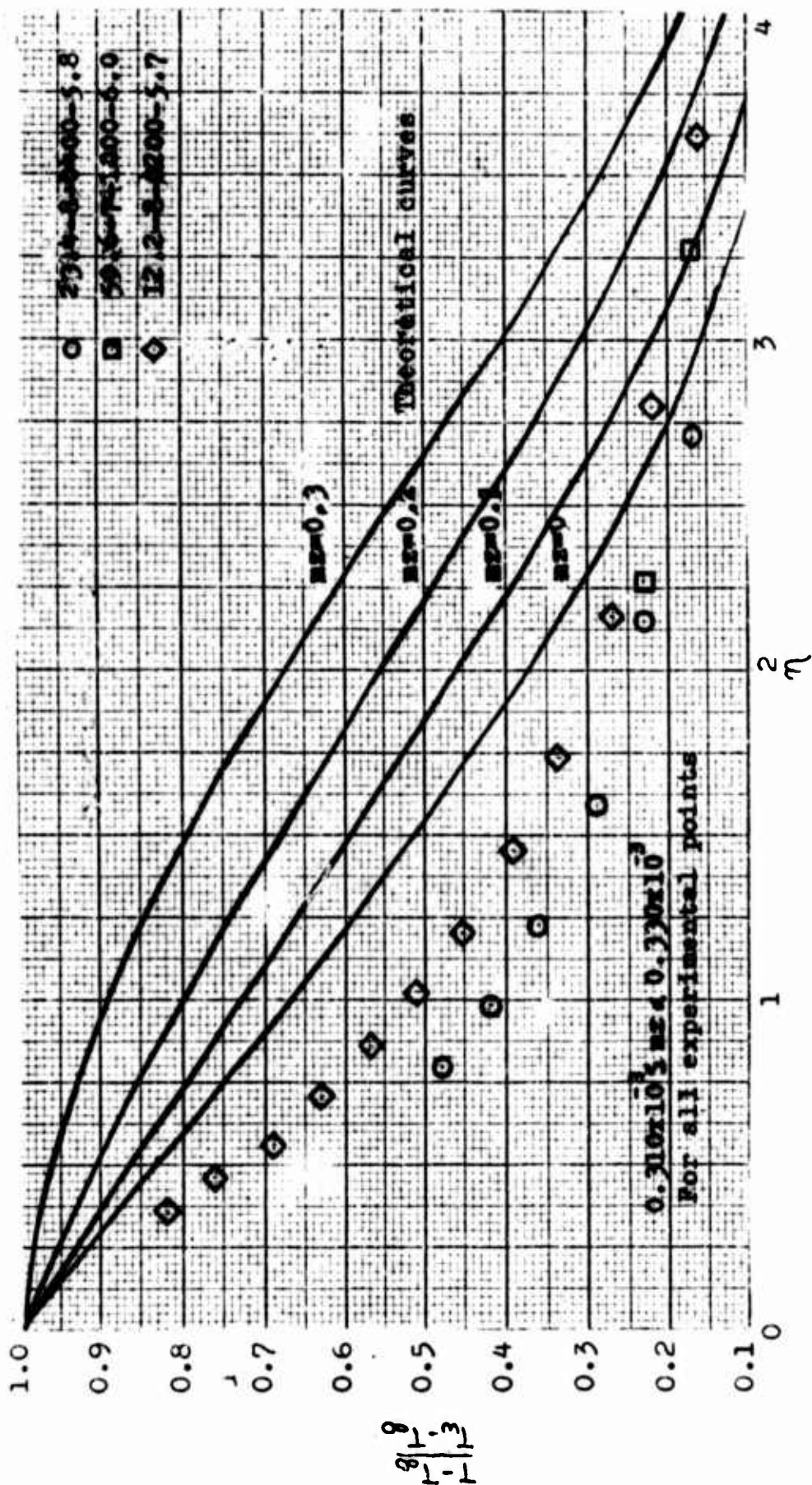


Fig. 47. Temperature profiles for various values of m . The experimental points are designated by a number indicating free stream velocity (ft. per sec.)-distance from leading edge (inches)-corona current (μ amps)-grid voltage (kilovolts).

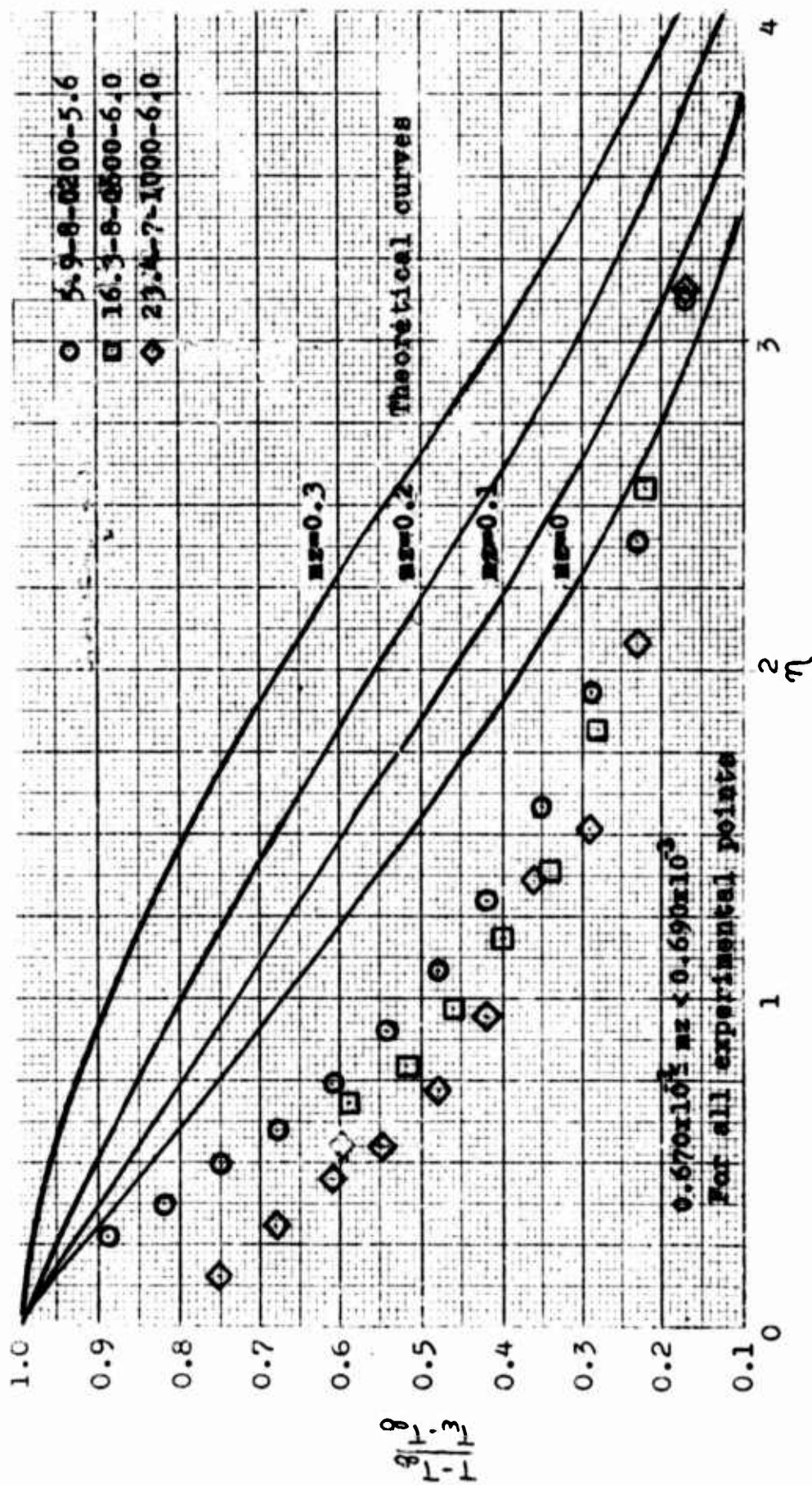


Fig. 48. Temperature profiles for various values of m_z . The experimental points are designated by a number indicating free stream velocity (ft. per sec.)-distance from leading edge(inches)-corona current (μ amps)-grid voltage(kilovolts).

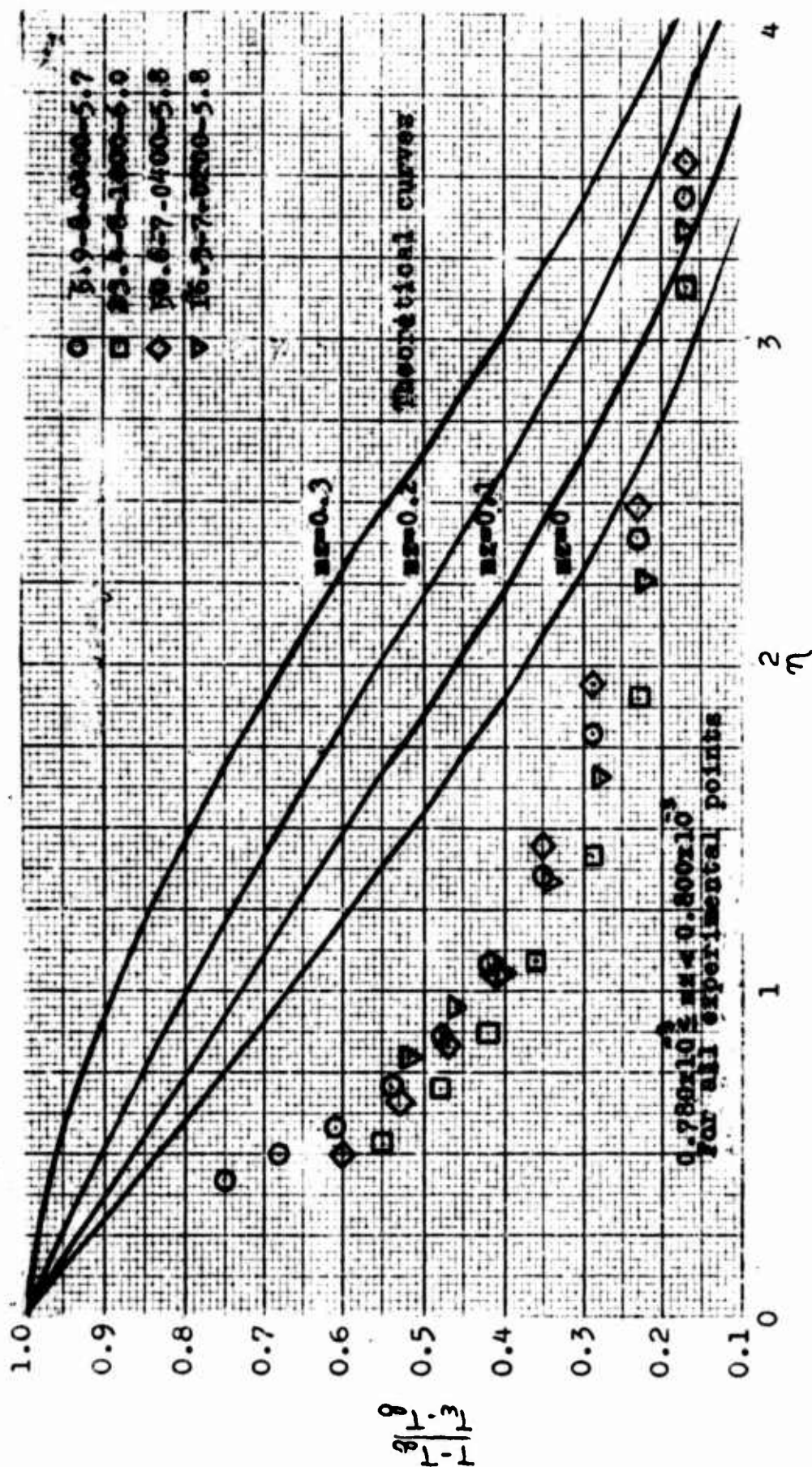


Fig.49 . Temperature profiles for various values of m . The experimental points are designated by a number indicating free stream velocity (ft. per sec.)-distance from leading edge(inches)-corona current (μ amps)-grid voltage(kilovolts).

Discussion of Results

The effect of corona discharge on the heat transfer from a flat plate at zero incidence in forced convection appears to become negligible at free stream velocities greater than forty times the maximum free convective velocity for the same temperature difference as shown in Figure 23. At high free stream velocities and low corona currents the change in Nusselt's number appears to be less than one. Actually this result is due to inaccuracies in determining the subtangent to the temperature profiles (Figure 22). When the temperature profiles are almost identical, any inaccuracy in determining the subtangent will be quite pronounced when the ratio of δ' 's is taken, as can be noted in Figure 23.

In order to check the accuracy of the conclusion drawn above, an additional test was run at 62.5 feet per second. The plate temperature was recorded before the high voltage was applied. Then a voltage was applied so that a corona current of 1000 μ amperes was indicated. No changes were made in the power being supplied to the plate. The set-up was left undisturbed for 30 minutes. The plate temperature was again recorded and was found to be identical to that taken before the voltage was applied. The heat balance was unaffected by the corona discharge. It can be concluded that the ratio of Nusselt's numbers before and after the voltage was applied is one.

Figures 42 through 49 are plots of different combinations of test parameters that resulted in similar values of mz (charge number \times 1/Reynolds number). The correlation was poor. Also plotted in these figures are the analytically determined curves. In all cases an increase in the value of mz decreased the ratio of $\frac{T-T_w}{T_w-T_\infty}$ for a given value of η experimentally. The opposite effect was predicted. The effect of changes in corona discharge rate alone are shown in Figures 50 and 51. The ratio of change in corona current to change in grid voltage was much greater than one. Therefore increases in corona current are proportional to increases in mz . The experimental trend for increasing values of mz was opposite to that predicted analytically.

The experimental values of mz were 1/1000 of those considered in the analysis. With the test configuration used larger values of mz were unobtainable due to break-down of the air at high grid voltages.

The no corona current profiles were plotted against the Blasius solution for a laminar boundary layer in forced convection. The results are shown in Figures 52 and 53. The correlation was poor at the higher free stream velocities. The existence of a laminar boundary layer is questionable. A plot of $\log_{10} \left(1 - \frac{T-T_w}{T_w-T_\infty} \right)$ vs. $\log_{10} \left(\frac{y}{\delta} \right)$ for a turbulent boundary layer should have a slope of 1/7 (Reference 15). Such a plot was made for the 50.6 and 62.5 foot per second tests (Figure 54). Their slopes ranged

from 1/4.8 to 1/6.0. It appears that the boundary layer was in transition from laminar to turbulent in this velocity range. This trend can also be noted in Figures 52 and 53.

For the 5.9 foot per second test there is some question whether it was representative of forced convective laminar flow because the free stream velocity is less than one order of magnitude greater than the maximum free convective velocity as shown in Figure 23. Figure 55 shows the 5.9 foot per second test with no corona current plotted with the Pohlhausen solution for free convection for the same temperature difference. The correlation is poorer than the same test plotted against the Blasius solution as shown in Figures 52 and 53. The 5.9 foot per second test appears to be representative of a laminar boundary layer.

Dr. Velkoff (Reference 1) observed similar effects of corona discharge for free convection as were observed in this investigation at low free stream velocities. He attributed the phenomenon to a mixing of two streams (the free convective current and the corona wind). A similar mixing probably took place in this experiment at low free stream velocities.

If the temperature profiles for the 5.9 foot per second cases with corona (Figures 50 and 51) are compared with the 50.6 and 62.5 foot per second no corona cases (Figures 52 and 53), a marked similarity is noted. Since it appears that the boundary layers for the higher velocities were

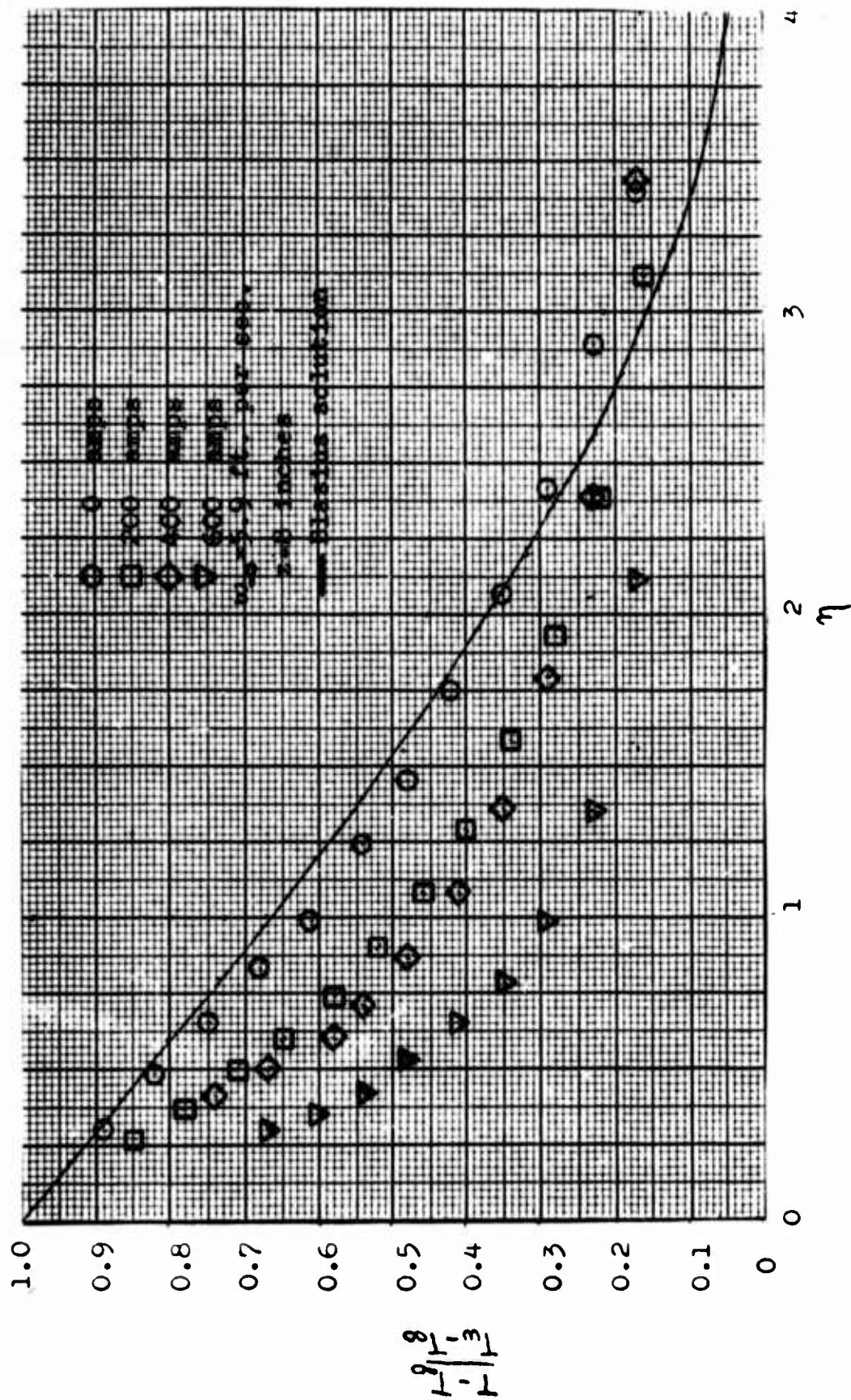


Fig. 50 . Temperature profiles for different amounts of corona current.

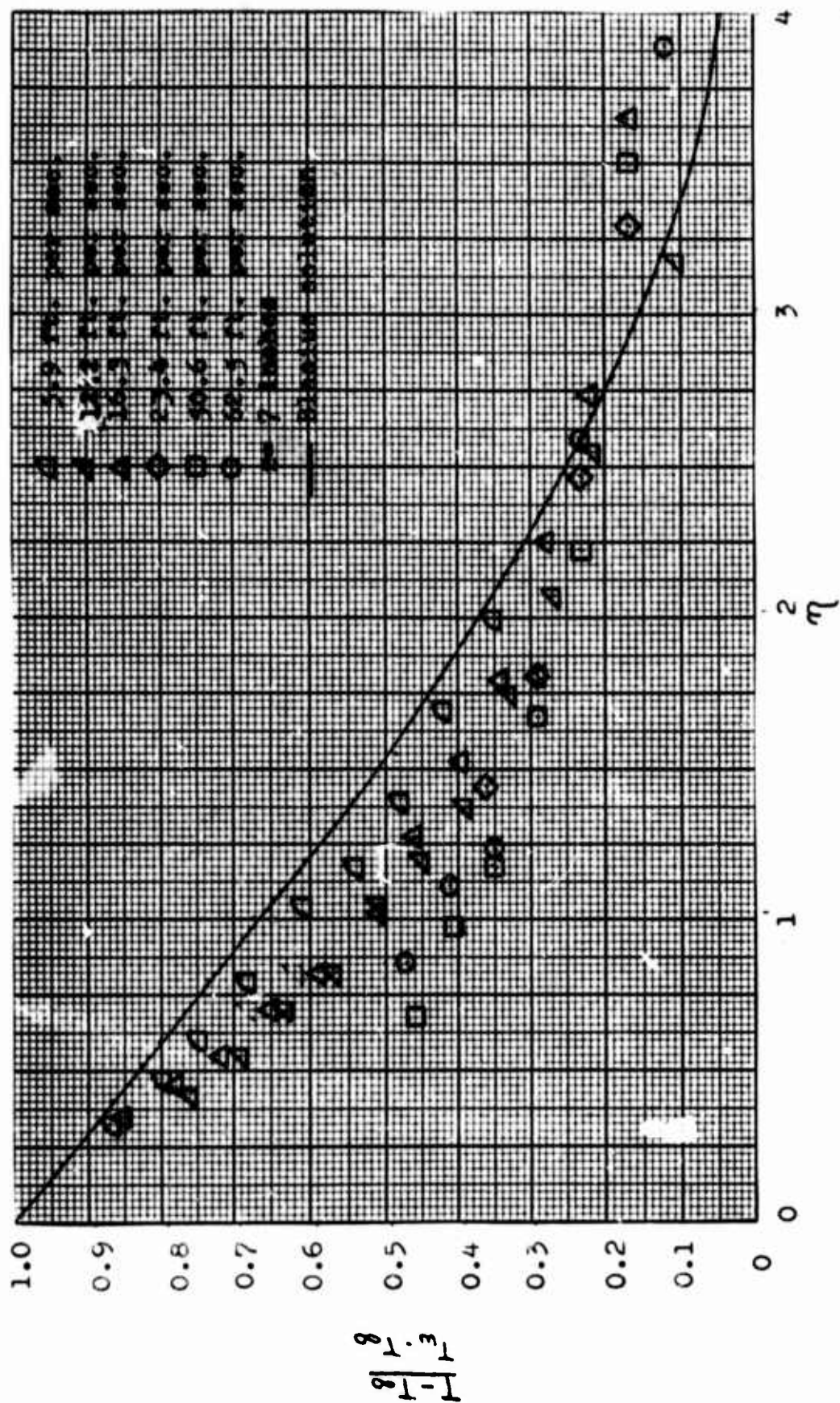


Fig.52 . Experimental temperature profiles plotted against the Flasius solution.

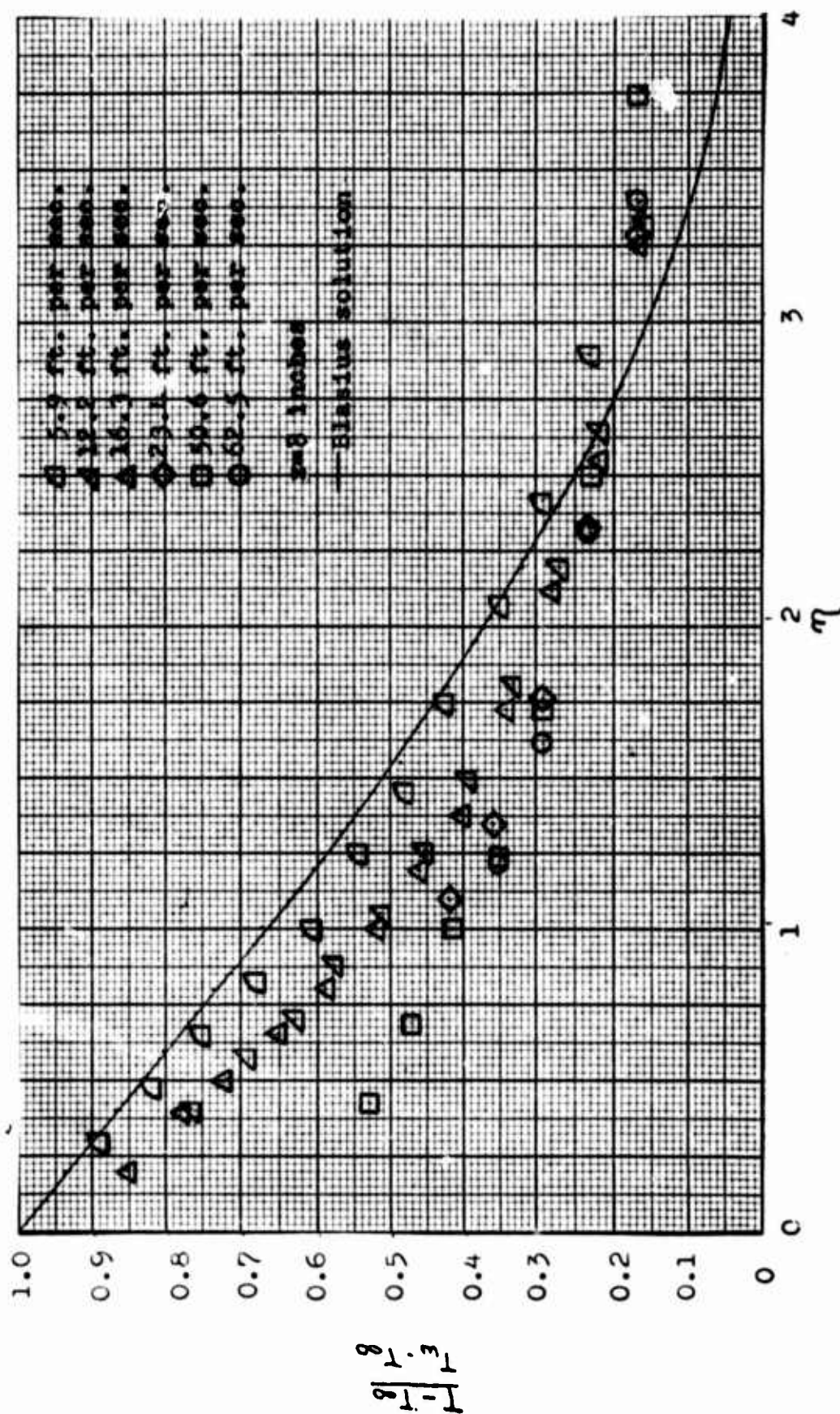


Fig. 53. Experimental temperature profiles plotted against the Blasius solution.

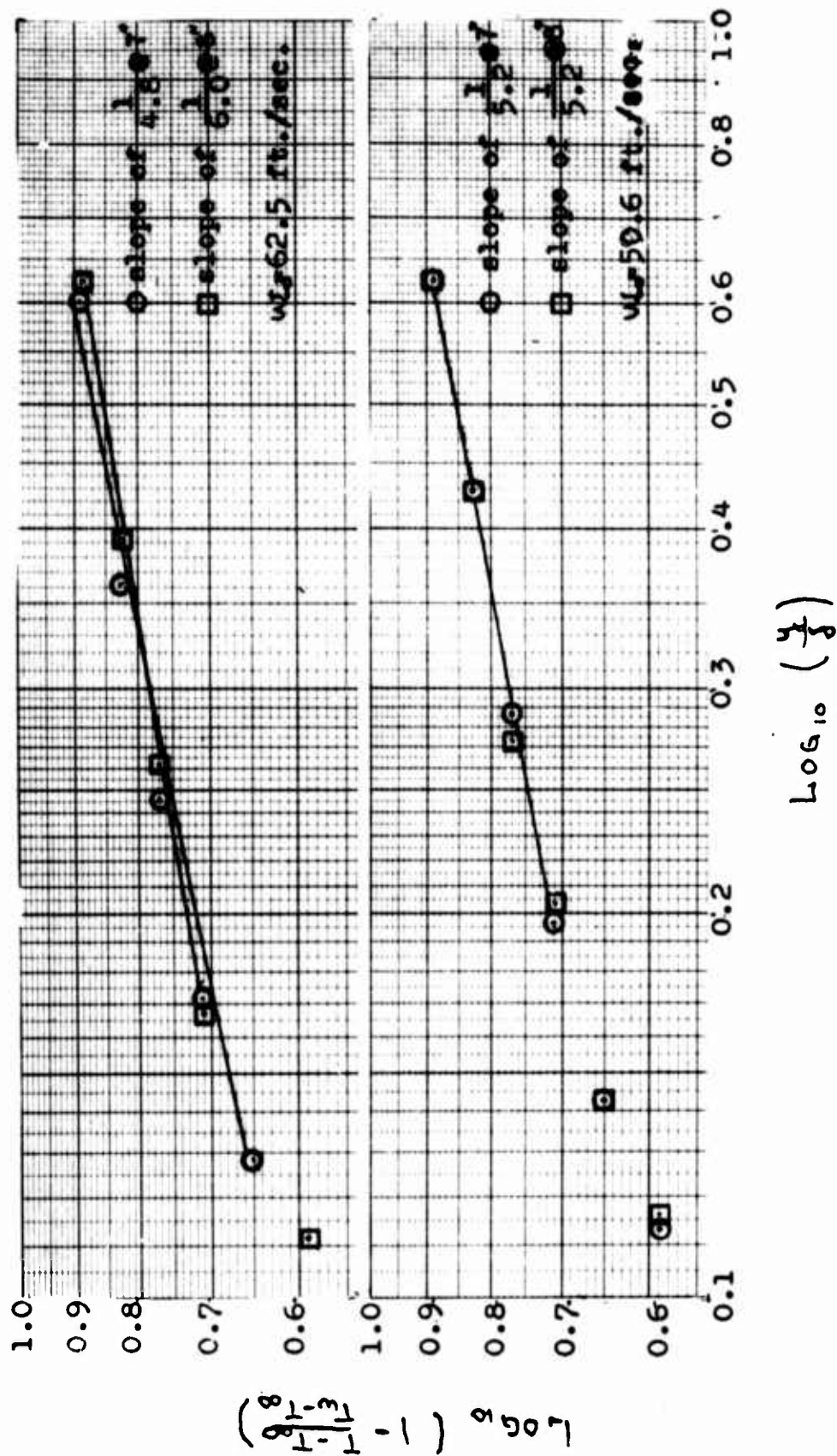


Fig. 54. Temperature profiles. \int defined to be $\frac{T-T_{\infty}}{T_w-T_{\infty}}=0.06$.

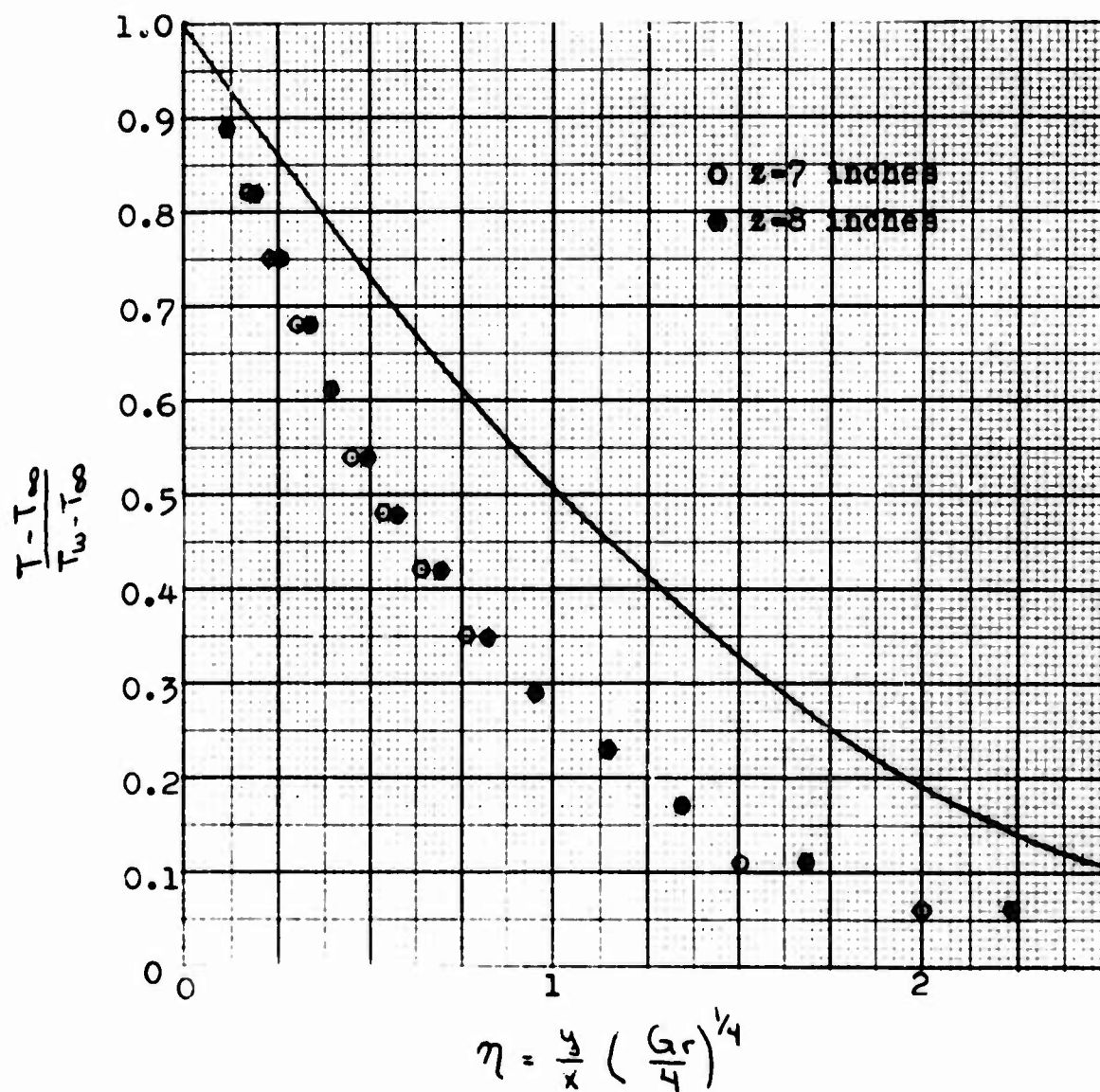


Fig.55 . Experimental points for the test run at 5.9 feet per second free stream velocity plotted against the Pohlhausen solution for free convection.

turbulent, a similarity between the high velocity, no corona boundary layers and the low velocity, corona boundary layers would suggest that the low velocity, corona boundary layers were also turbulent.

To account for this observation a new mechanism is needed to describe the effects of corona discharge on external, thermal boundary layers. A possible mechanism that would account for the observed result is that the corona discharge induces an instability in the flow. At high free stream velocities, the instability becomes a second order effect.

CONCLUSIONS

- 1.) At low free stream velocities the thermal boundary layer was drastically changed. Heat transfer was increased in a similar manner as was observed by Velkoff for free convection.
- 2.) As the free stream velocity was increased, the corona discharge effect became second order. At 62.5 feet per second, no change was noted between the corona and no corona tests.
- 3.) The effect at the lower velocities was opposite to those predicted by the body force hypothesis. It appears that a new mechanism must be hypothesized to explain the flow.
- 4.) It was found that the boundary layer was turbulent in the high free stream velocity tests without corona. It was also noted that their temperature profiles were similar to those for the low free stream velocity tests with corona discharge.
- 5.) A possible mechanism to explain the phenomenon observed is that the corona discharge induces an instability that becomes a second order effect at high free stream velocities.

REFERENCES

1. Velkoff, H. R., "An Exploratory Investigation of the Effects of Ionization on the Flow and Heat Transfer in a Dense Gas", ASD-TDR-63-842 Aero Propulsion Laboratory, ASD, Air Force Systems Command, W-PAFB, Ohio, 1963.
2. Velkoff, H. R., "An Analysis of the Effects of Ionization on the Laminar Flow of a Dense Gas in a Channel", RTD-TDR-63-4009 Aero Propulsion Laboratory, Air Force Systems Command, W-PAFB, Ohio, 1963.
3. Chuang, T. S., An Interim Report for Contract DA-31-124-ARO-D-246 Done at The Ohio State University under RF Project 1864, 1967.
4. Schlichting, H., Boundary Layer Theory, McGraw-Hill, New York, N. Y., 1963.
5. Rossow, V. J., "On Flow of Electrically Conducting Fluid Over a Flat Plate in the Presence of a Transverse Magnetic Field", NACA TN 3971, 1957.
6. Kennard, R. B., "An Optical Method for Measuring Temperature Distribution and Convective Heat Transfer", Bureau of Standards Journal of Research, Vol. 8.
7. Blue, R. E., "Interferometer Corrections and Measurements of Laminar Boundary Layers in Supersonic Stream", NACA-TN 2110.
8. Cobine, J. D., Gaseous Conductors, Dover Publications, Inc., New York, N. Y., 1958.

9. Attwood, S. S., Electric and Magnetic Fields, John Wiley and Sons, Inc., New York, N. Y., 1949.
10. Eckert, E. R. G. and Soehngen, E. E., "Studies on Heat Transfer in Laminar Free Convection with the Mach-Zender Interferometer", AF-TN 5747.
11. Hottenroth, "Some Experiences Gathered on the Mach-Zender Interferometer", a report for the Institute for Aerodynamics Research Institute Hermann Goering, Brunswick.
12. Gebhart, B. and Knowles, C. P., "Design and Adjustment of a 20 cm Mach-Zender Interferometer", The Review of Scientific Instruments, Vol. 37, No. 1.
13. International Cricitcal Tables, Vol. 7, McGraw-Hill Book Company, New York, N. Y., 1930.
14. Keatino, T. V., "A Study of the Characteristics of the Boundary Layer on a Flat Plate with Forced Convection", a Thesis at The Ohio State University, 1948.
15. Eckert, E. R. G., Introduction To The Transfer of Heat and Mass, McGraw-Hill Book Company, Inc., New York, N. Y., 1950.

Appendix I
Rossow Solution

A. Function $f_2(\eta)$ (after Rossow).

η	f_2	f_2'	f_2''
0	0	0	-0.894
0.2	-0.018	-0.178	-0.888
0.4	-0.071	-0.354	-0.868
0.6	-0.159	-0.525	-0.835
0.8	-0.281	-0.687	-0.789
1.0	-0.433	-0.839	-0.730
1.2	-0.615	-0.978	-0.660
1.4	-0.824	-1.102	-0.579
1.6	-1.055	-1.209	-0.489
1.8	-1.306	-1.298	-0.394
2.0	-1.573	-1.367	-0.296
2.2	-1.862	-1.416	-0.197
2.4	-2.138	-1.446	-0.103
2.6	-2.429	-1.458	-0.017
2.8	-2.720	-1.454	+0.059
3.0	-3.010	-1.435	0.121
3.2	-3.294	-1.406	0.168
3.4	-3.572	-1.369	0.201
3.6	-3.841	-1.327	0.218
3.8	-4.102	-1.283	0.222
4.0	-4.354	-1.239	0.216
4.2	-4.598	-1.197	0.200
4.4	-4.833	-1.159	0.180
4.6	-5.062	-1.125	0.156
4.8	-5.284	-1.097	0.131
5.0	-5.501	-1.073	0.107
5.2	-5.713	-1.054	0.085
5.4	-5.923	-1.039	0.065
5.6	-6.129	-1.028	0.049
5.8	-6.334	-1.019	0.036
6.0	-6.537	-1.013	0.026
6.2	-6.739	-1.009	0.018
6.4	-6.941	-1.006	0.012
6.6	-7.141	-1.004	0.008
6.8	-7.342	-1.002	0.005
7.0	-7.542	-1.001	0.003
7.2	-7.743	-1.001	0.002
7.4	-7.943	-1.001	0.001
7.6	-8.143	-1.000	0.001
7.8	-8.343	-1.000	0.000
8.0	-8.543	-1.000	0.000

B. Variations of the velocity profiles.

a.) $mz=0$

η	$f_0' = \frac{\omega}{\omega_0} = \frac{\omega}{\omega_{\infty}}$	$1-f_0'$	f_1'
0	0.00000	1.00000	0.000
1.0	0.32979	0.67.21	-0.839
2.0	0.62977	0.37023	-1.367
3.0	0.84605	0.15395	-1.435
4.0	0.95552	0.04448	-1.239
5.0	0.99155	0.00845	-1.073
6.0	0.99898	0.00102	-1.013
7.0	0.99992	0.00008	-1.001
8.0	1.00000	0.00000	-1.000

b.) $mz=0.1$

η	mzf	$\frac{\omega}{\omega_0}$	$\frac{\omega}{\omega_0} = \frac{\omega}{\omega_{\infty}} - \frac{\omega}{\omega_0}$	$1 - \frac{\omega}{\omega_0}$
0	0.0000	0.00000	0.00000	1.00000
1.0	-0.0839	0.24589	0.27320	0.72680
2.0	-0.1367	0.49307	0.54785	0.45215
3.0	-0.1435	0.70245	0.78050	0.21940
4.0	-0.1239	0.83162	0.92400	0.07600
5.0	-0.1073	0.88425	0.98250	0.01750
6.0	-0.1013	0.89768	0.99740	0.00260
7.0	-0.1001	0.89982	0.99980	0.00020
8.0	-0.1000	0.90000	1.00000	0.00000

c.) $mz=0.2$

η	mzf	$\frac{\omega}{\omega_0}$	$\frac{\omega}{\omega_0} = \frac{\omega}{\omega_{\infty}} - \frac{\omega}{\omega_0}$	$1 - \frac{\omega}{\omega_0}$
0	0.0000	0.00000	0.00000	1.00000
1.0	-0.1678	0.16199	0.2025	0.7975
2.0	-0.2734	0.35637	0.4455	0.5545
3.0	-0.2870	0.55900	0.6990	0.3010
4.0	-0.2478	0.70772	0.8846	0.1154
5.0	-0.2146	0.77695	0.9712	0.0288
6.0	-0.2026	0.79638	0.9955	0.0045
7.0	-0.2002	0.79972	0.9996	0.0004
8.0	-0.2000	0.80000	1.0000	0.0000

d.) $mz=0.3$

η	mzf_2'	$\frac{w}{w_\infty}$	$\frac{w}{w_\infty} = \frac{w}{w_\infty} - \frac{w}{w_\infty}$	$1 - \frac{w}{w_\infty}$
0	0.0000	0.00000	0.00000	1.00000
1.0	-0.2517	0.07757	0.01108	0.98892
2.0	-0.4101	0.21967	0.31380	0.68620
3.0	-0.4305	0.41555	0.59360	0.40640
4.0	-0.3717	0.58382	0.83400	0.16600
5.0	-0.3219	0.66965	0.95660	0.04340
6.0	-0.3039	0.69508	0.99290	0.00710
7.0	-0.3003	0.69962	0.99940	0.00060
8.0	-0.3000	0.70000	1.00000	0.00000

C. Boundary layer thickness.

mz	η_s	$\frac{\delta}{z} \sqrt{Re_z}$
0	4.960	4.960
0.1	5.500	5.500
0.2	5.774	5.774
0.3	5.920	5.920

Appendix II Adjustment of Interferometer

The Mach-Zender interferometer can be aligned to give good fringes by following the procedure outlined below.* The four mirrors must be positioned so that the path lengths are within two wave train lengths of each other. This can be accomplished with rule and square. A rectangular arrangement of the mirrors is preferred but is not necessary. This step insures that with proper angular rotation of the mirrors monochromatic fringes can be observed. It is suggested that the wave train length be determined using a Michelson interferometer by measuring the travel of the adjustable plane mirror from first fringe appearance to last. This distance is the wave train length. If the mirror is returned one half the wave train length the instrument should be adjusted so that the so called white fringe appears in the telescope. If the mercury source is now replaced by an ordinary light bulb, one set of fringes will appear. By adjusting the simpler Michelson instrument the operator can become familiar with features to look for in adjusting the Mach-Zender interferometer.

Now that the preliminary set-up has been made accurate alignment begins by collimation of the light. The diameter of the beam at various distances from the parabolic mirror is measured. An additional check can be made by reflecting

* This Appendix is a combination of techniques reported in References 11 and 12 as well as experiences of the author.

the beam back on itself with a plane mirror. When the light source and its reflected image coincide at the aperture, the beam is parallel. Next the collimating mirror is adjusted so light passes through the beam splitter and does not overlap any of mirror mount (M2) shown in Figure 56. This determines the position of the collimating mirror and is effectively independent of the angular orientation of the interferometer since any further adjustment is less than 1 degree. The first beam splitter (BS1) is rotated until the reflected beam of light strikes mirror (M1) without overlapping its mount. No further adjustment of BS1 is necessary. M1 is rotated so that the reflected beam does not overlap the mount of BS2. This insures maximum field size when the beams reunite at BS2.

The fringes may now be found by rotation of M2 and BS2 only. A telescope (a Civil Engineer's level was used and found satisfactory) was positioned in front of BS2 so that the image of the small mirror at the focus of the parabolic mirror was in view at infinite. Next a two dimensional object, such as a hook, was placed at the input to the interferometer BS1 so that it appears in the field of view by adjusting the focus of the telescope only. Due to the angular misalignment of mirrors M2 and BS2, two primary images of both hook and mirror will appear at their respective foci. Focusing on the hook, adjust BS2 until a single image is observed. Then the mirror is focused upon and M2 adjusted

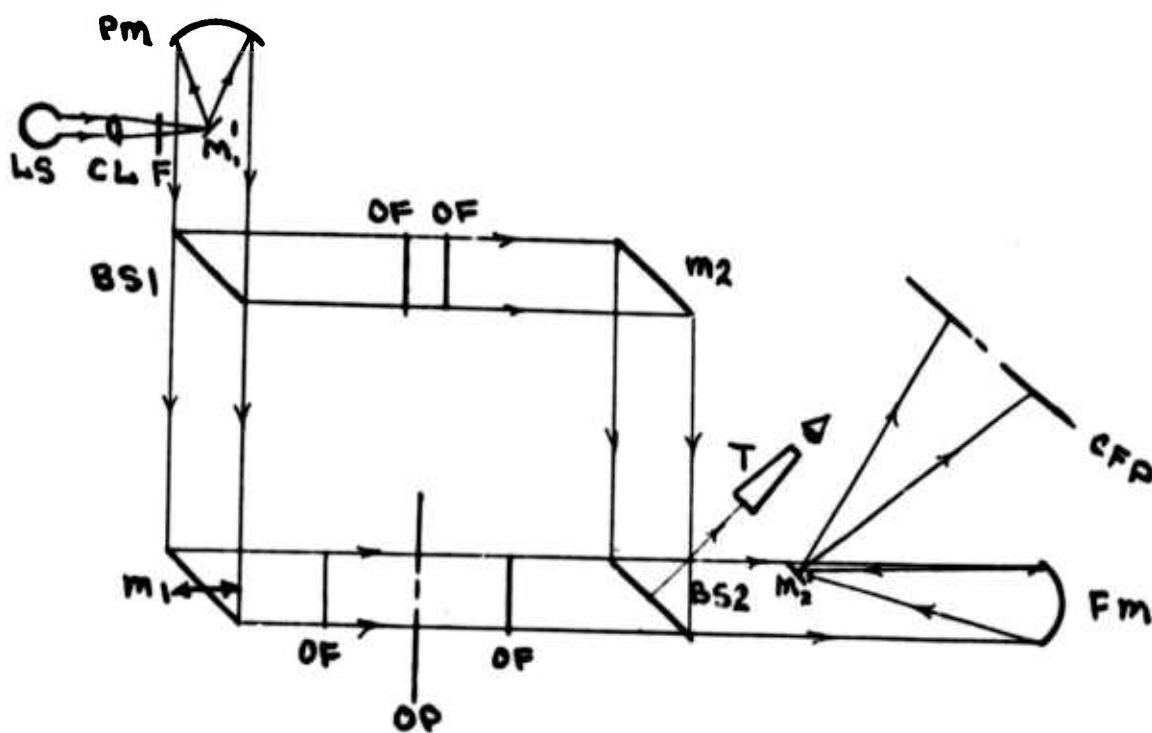


Fig. 56 . Schematic of interferometer optical system. LS) light source, CL) double-convex lens, F) monochromatic filter, M) mirror at focal point of parabolic mirror, PM) parabolic mirror, BS1) beam splitter 1, M1) mirror 1, OF) optical flat, OP) object plane in test section, M2) mirror 2, BS2) beam splitter 2, FM) focusing mirror, M) mirror to reflect light from focusing mirror to CFP, CFP) camera focal plane, T) telescope.

until one image appears. If when having refocused upon the hook, its two images are closer than before, the procedure is continued until both objects appear to have only one image. Fringes will now appear at infinite. If the images diverge, reverse the procedure. Adjust for coincident hook images with mirror M2 and mirror images with BS2. The method converges rapidly but requires care in the initial set-up. Since the light source has a finite size, the image of the test section must be focused on the camera screen. So that both the fringes and object plane are sharply defined, the fringes must now be focused at the object plane of the test section. If the fringes were initially observed on the mirror at the focus of the parabolic mirror, the focusing procedure can be determined by adjusting the telescope on a nearer object plane and rotating BS2 and M2 so that the fringes focus at this new plane. Continue until the fringes appear in focus within the test section.

Reasonably sharp fringes can now be observed, but to make them critically sharp, the path lengths must be equalized. Gebhart and Knowles (Reference 12) suggested equalization by a method reported by Bryon. The interference filter is removed so that gradually fading groups of fringes can be observed. These groups correspond to beats due to many spectral lines. Mirror M1 is translated until the most distinct group appears in a similar manner as the white fringe was found with the Michelson interferometer. A

particular group is then focused on the slit of a spectro-
scope with the fringes horizontal and slit vertical. The
fringes as viewed in the spectroscope appear at an angle
against the weak continuous spectrum of the hot glass of the
lamp and against the lamp lines. Mirror M1 is translated to
view different fringe groups and fringes within a group until
the spectroscope fringes are horizontal. At this transla-
tional position, the two optical path lengths are identically
the same and all wave lengths will interfere. This is the
white fringe adjustment. If a continuous spectrum light
source is substituted for the mercury lamp, the white fringe
appears on a screen at the position of the spectroscope.

The remaining adjustment is to focus the fringes exactly
at the test section to insure maximum sharpness for greater
resolution. For this purpose, a 60 power telescope is used.
A diffusing screen is placed over the collimating mirror and
a piece of exposed photographic film in front of the light
source aperture. Light intensity must be reduced to avoid
eye damage. The telescope is then focused through the beam
splitter on the test section. Using the low magnification
the depth of field of the telescope is sufficiently great
so that both fringes and test section are in focus. The
beam splitter is rotated slightly to bring the fringes closer
to the test section object plane. The magnification of the
telescope is increased, thereby reducing the depth of field,
to further localize the fringes. At maximum magnification

the fringes can be located to within 2 cm of the object plane insuring maximum fringe sharpness at the viewing screen.

Appendix III Analysis Method

Let A and B in Figure 57 be two adjacent monochromatic interference fringes.* If the temperature were uniform throughout, the center line of fringe A instead of the center line of fringe B would pass through the point P. The shift of one fringe at the point P indicates that there is one less wave of light in the path through P than would be if the temperature at P were the same as at Q. The temperature of the air is obtained from its density which is related to the refractive index by the Lorenz-Lorentz equation

$$\frac{\eta^2 - 1}{\eta^2 + 1} = C \rho \quad (1)$$

where η is the index of refraction, ρ the density, and C is a constant characteristic of the fluid.

Since the index of refraction of air under test conditions is about 1.0003, the above expression is approximated by

$$(\eta - 1) = \frac{3}{2} C \rho \quad (2)$$

If, under one set of conditions, N_1 , and η_1 are the number of light waves over a given path, and the index of refraction, respectively, and N_2 and η_2 are the same quantities under a second set of conditions then

$$\eta_1 = \frac{N_1}{N_0} \quad , \quad \eta_2 = \frac{N_2}{N_0} \quad (3)$$

* This Appendix was taken from Reference 6.

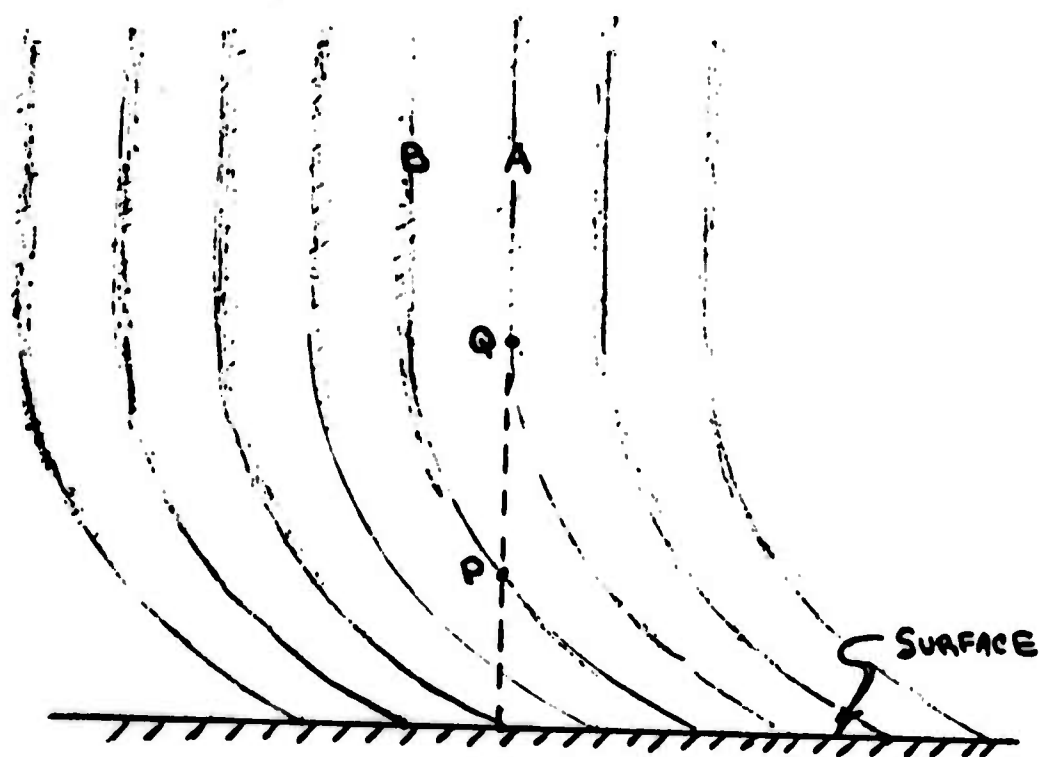


Fig. 57 . Schematic illustrating method used to analyze interference data.

where N_0 is the number of light waves in the same path in a vacuum. If L is the length of path under consideration, which is that of the heated surface, and if λ_0 is the wave length in a vacuum of the light used then

$$N_0 = \frac{L}{\lambda_0} \quad (4)$$

From equation (2) the change of index of refraction for a given density is

$$n_1 - n_2 = \frac{3}{2} C (\rho_1 - \rho_2) \quad (5)$$

Inserting the values in equation (3) and (4) and rearranging yields

$$\begin{aligned} N_1 - N_2 &= \frac{3}{2} C \rho_1 \frac{L}{\lambda_0} \left(1 - \frac{\rho_2}{\rho_1}\right) \\ &= (n_1 - 1) \frac{L}{\lambda_0} \left(1 - \frac{\rho_2}{\rho_1}\right) \end{aligned} \quad (6)$$

If the change in density is caused by a change in temperature only

$$\frac{\rho_2}{\rho_1} = \frac{T_1}{T_2} \quad (7)$$

then

$$N_1 - N_2 = (n_1 - 1) \frac{L}{\lambda_0} \frac{T_2 - T_1}{T_2} \quad (8)$$

Since in the interferometer the change in number of waves in a given path is equal to the fringe displacement Equation (8) gives the fringe displacement as measured in

fringe widths, that takes place when the temperature is changed from T_1 to T_2 °K. Letting T_1 and n_1 be the absolute temperature and index of refraction of room air, equation (8) may be solved explicitly for the temperature rise above the air of the room giving.

$$T_2 - T_1 = T_1 \frac{\Delta N}{(n_1 - 1) \frac{L}{\lambda_0} - \Delta N} \quad (9)$$

The quantity $(n_1 - 1)$ is given in the International Critical Tables (Reference 13) for standard conditions and may be calculated for any condition by using the gas laws, making proper corrections for humidity. For conditions during the tests reported here, the partial pressure of water vapor was small enough to be neglected for the accuracy wanted. Equation (10) was developed to correct index of refraction for test conditions

$$(n - 1) = \frac{9.812 P \times 10^{-6}}{0.935 + 0.002035 T} \quad (10)$$

P and T are the atmospheric pressure in inches of mercury and room temperature in °F respectively. Letting ΔN be called \mathcal{E} and the product $\frac{\mathcal{E} \lambda}{L(n-1)}$ be β^* equation (9) may be rewritten (Reference 14)

$$T_2 = T_1 \frac{1}{1 - \beta^*} \quad (11)$$

The quantity β^* is small compared to 1 so $\frac{1}{1 - \beta^*}$ may be ex-

panded in a series

$$\frac{1}{1-\beta^*} = 1 - \beta^* - \beta^{*2} - \beta^{*3} + \dots$$

Inserting into equation (11) and rewriting gives

$$\Delta T = T_1 (\beta^* + \beta^{*2} + \beta^{*3} + \dots) \quad (12)$$

Appendix IV Refraction Error

As a general rule the light will not appear to come from the point in the object plane at the distance from the surface at which the light entered the tunnel.* Instead, it will appear to originate at point y_a Figure 17. The location of the point is influenced by a.) the emergent height of the light y_e , b.) the emergent angle θ_e , c.) the thickness of the tunnel window γ , and d.) the location of the object plane. The indicated density is therefore an average along its curved path plus the additional path through the window.

Correction of the refraction error is possible by two methods. Using the indicated profile as a first approximation to the correct profile, calculation by numerical integration of the refraction equation will yield a more accurate profile. Such a process would be of doubtful accuracy if the indicated profile differs by more than 5 percent maximum error in density due to the sensitivity of the light path to values of density.

For steady test conditions a method using two photos at a given condition differing only in the location of the object plane of the camera can be used. In one case the camera was focused on the center of the plate and in the other at the edge nearest the light source. The indicated profiles

* This Appendix was taken from Reference 7.

calculated for the two photos differ only in that the apparent height above the surface at which each light ray appears to originate is shifted. The emergent angle θ_e of the light leaving the tunnel can be found at a given value of density ratio by taking the difference in the apparent heights indicated for that density ratio by the two profiles and then dividing the difference by the distance between the object planes for the two photographs. The angle θ_e is related to the density difference between the incident and emergent points on the light path by the equation

$$\theta_e = \sqrt{2 K \rho_1 \left[\left(\frac{\rho}{\rho_1} \right)_e - \left(\frac{\rho}{\rho_1} \right)_i \right]} \quad (1)$$

which was obtained by integrating the equation (2) (the equation for the path of light ray through a two dimensionally non-homogeneous media based on Fermat's principle of refraction.)

$$\frac{y''}{1+y'^2} = \frac{1}{n} \frac{\partial n}{\partial y} - \frac{1}{n} \frac{\partial n}{\partial z} y' \quad (2)$$

Two approximations were made in deriving the equation. They were $\tan \theta_e = \theta_e$ AND $n_e^2 - n_i^2 = 2 n_i (n_e - n_i)$

If the density is assumed to vary linearly in the direction between the incident and emergent points on the light path, the following relation that were found from the refraction equation for a constant density gradient and be applied;

$$\left(\frac{\rho}{\rho_1}\right)_{AVE} - \left(\frac{\rho}{\rho_1}\right)_i = \frac{K \rho_1 L^2}{6} \left[\frac{\left(\frac{\rho}{\rho_1}\right)_e - \left(\frac{\rho}{\rho_1}\right)_i}{y_e - y_i} \right]^2 \quad (3)$$

$$(y_e - y_i)^2 = \frac{1}{2} K \rho_1 L^2 \left[\left(\frac{\rho}{\rho_1}\right)_e - \left(\frac{\rho}{\rho_1}\right)_i \right] \quad (4)$$

substituting equations (1) and (4) in (3) yields

$$\left(\frac{\rho}{\rho_1}\right)_{AVE} - \left(\frac{\rho}{\rho_1}\right) = \frac{\theta_e}{6 \rho_1 K} \quad (5)$$

which is an expression for the averaging error. The window error can be found in terms of the fringe shift Nq (Reference 7)

$$\left(\frac{\rho}{\rho_1}\right)_{IND} - \left(\frac{\rho}{\rho_1}\right)_{AVE} = \frac{\Delta \rho}{\rho_1 K L} Nq \quad (6)$$

The value of the two errors, when subtracted from the indicated density, give a number approximately equal to the density ratio at the height y_i . An equation for y_i in terms of apparent height and emergent angle, both of which are known from the photographic data

$$y_i = y_a \theta_e \gamma \left(\frac{n_g - 1}{n_g} \right) + (FL - \frac{L}{2}) \theta_e \quad (7)$$

The factor F (Figure 17) determined by location of the object

-113-

plane is $\frac{1}{2}$ when y_a is read from the curve corresponding to the center-focus interferogram (Reference 7).

Unclassified
Security Classification

DOCUMENT CONTROL DATA - R&D		
(Security classification of title, body of abstract and indexing annotation must be entered when the overall report is classified)		
1. ORIGINATING ACTIVITY (Corporate author) The Ohio State University Research Foundation 1314 Kinnear Rd. Columbus, Ohio 43212		2a. REPORT SECURITY CLASSIFICATION Unclassified
		2b. GROUP
3. REPORT TITLE AN INTERFEROMETRIC STUDY OF THE EFFECTS OF CORONA DISCHARGE ON THE TEMPERATURE PROFILES ON A FLAT, UNIFORM TEMPERATURE PLATE IN FORCED CONVECTION		
4. DESCRIPTIVE NOTES (Type of report and inclusive dates) Technical		
5. AUTHOR(S) (Last name, first name, initial) Godfrey, Richard D. Velkoff, Henry R.		
6. REPORT DATE June 1967	7a. TOTAL NO. OF PAGES 126	7b. NO. OF REFS 15
8a. CONTRACT OR GRANT NO. DA-31-124-ARO-D-246	8b. ORIGINATOR'S REPORT NUMBER(S) Technical Report # 4	
a. PROJECT NO. 2001050B700, 1D12, 40A142		
c.	9b. OTHER REPORT NO(S) (Any other numbers that may be assigned this report)	
d.		
10. AVAILABILITY/LIMITATION NOTICES Distribution of this document is unlimited		
11. SUPPLEMENTARY NOTES Thesis	12. SPONSORING MILITARY ACTIVITY U. S. Army Research Office - Durham Box C.M., Duke Station Durham, North Carolina 27706	
13. ABSTRACT The purpose of this thesis was to study the effects of corona discharge on flow past a flat plate at zero incidence. In a previous exploratory investigation into the effects of ionization on the gas in channel flow, interesting results were observed. Pressure drops and heat transfer coefficients were found to double. The velocity profile was distorted. In an attempt to explain the phenomenon, Velkoff hypothesized an induced electric field component in opposition to the flow. An analytical solution for laminar flow with a uniform charge density in the boundary layer was developed by extending the Rossow solution for MHD flows. The corona effect was predicted to retard the flow and thicken the boundary layer. An experimental program was initiated to study this phenomenon by observing changes in the temperature profiles on a flat, uniform temperature plate in forced convection with a Mach-Zender interferometer. A series of tests were run with a constant plate to ambient temperature difference but different free stream velocities and corona currents. At a 62.5 foot per second free stream velocity, a 1000 ampere corona current did not effect the flow. At lower velocities, the effects observed were opposite to those predicted. It was found that the boundary layer was turbulent at the 62.5 foot per second test. Also it was noted that 5.9 foot per second test with corona discharge was similar to the 62.5 foot per second test. The body force hypothesized by Velkoff does not appear to describe the corona effect. A possible mechanism that would account for the observed result is that the corona discharge induces an instability in the flow.		

DD FORM 1473
1 JAN 64

Unclassified
Security Classification

14 KEY WORDS	LINK A		LINK B		LINK C	
	ROLE	WT	ROLE	WT	ROLE	WT
Corona discharge						
Electro Fluid Mechanics						
Electro Convection						

INSTRUCTIONS

1. **ORIGINATING ACTIVITY:** Enter the name and address of the contractor, subcontractor, grantee, Department of Defense activity or other organization (corporate author) issuing the report.

2a. **REPORT SECURITY CLASSIFICATION:** Enter the overall security classification of the report. Indicate whether "Restricted Data" is included. Marking is to be in accordance with appropriate security regulations.

2b. **GROUP:** Automatic downgrading is specified in DoD Directive 5200.10 and Armed Forces Industrial Manual. Enter the group number. Also, when applicable, show that optional markings have been used for Group 3 and Group 4 as authorized.

3. **REPORT TITLE:** Enter the complete report title in all capital letters. Titles in all cases should be unclassified. If a meaningful title cannot be selected without classification, show title classification in all capitals in parenthesis immediately following the title.

4. **DESCRIPTIVE NOTES:** If appropriate, enter the type of report, e.g., interim, progress, summary, annual, or final. Give the inclusive dates when a specific reporting period is covered.

5. **AUTHOR(S):** Enter the name(s) of author(s) as shown on or in the report. Enter last name, first name, middle initial. If military, show rank and branch of service. The name of the principal author is an absolute minimum requirement.

6. **REPORT DATE:** Enter the date of the report as day, month, year, or month, year. If more than one date appears on the report, use date of publication.

7a. **TOTAL NUMBER OF PAGES:** The total page count should follow normal pagination procedures, i.e., enter the number of pages containing information.

7b. **NUMBER OF REFERENCES:** Enter the total number of references cited in the report.

8a. **CONTRACT OR GRANT NUMBER:** If appropriate, enter the applicable number of the contract or grant under which the report was written.

8b, 8c, & 8d. **PROJECT NUMBER:** Enter the appropriate military department identification, such as project number, subproject number, system numbers, task number, etc.

9a. **ORIGINATOR'S REPORT NUMBER(S):** Enter the official report number by which the document will be identified and controlled by the originating activity. This number must be unique to this report.

9b. **OTHER REPORT NUMBER(S):** If the report has been assigned any other report numbers (either by the originator or by the sponsor), also enter this number(s).

10. **AVAILABILITY/LIMITATION NOTICES:** Enter any limitations on further dissemination of the report, other than those

imposed by security classification, using standard statements such as:

- (1) "Qualified requesters may obtain copies of this report from DDC."
- (2) "Foreign announcement and dissemination of this report by DDC is not authorized."
- (3) "U. S. Government agencies may obtain copies of this report directly from DDC. Other qualified DDC users shall request through _____."
- (4) "U. S. military agencies may obtain copies of this report directly from DDC. Other qualified users shall request through _____."
- (5) "All distribution of this report is controlled. Qualified DDC users shall request through _____."

If the report has been furnished to the Office of Technical Services, Department of Commerce, for sale to the public, indicate this fact and enter the price, if known.

11. **SUPPLEMENTARY NOTES:** Use for additional explanatory notes.

12. **SPONSORING MILITARY ACTIVITY:** Enter the name of the departmental project office or laboratory sponsoring (paying for) the research and development. Include address.

13. **ABSTRACT:** Enter an abstract giving a brief and factual summary of the document indicative of the report, even though it may also appear elsewhere in the body of the technical report. If additional space is required, a continuation sheet shall be attached.

It is highly desirable that the abstract of classified reports be unclassified. Each paragraph of the abstract shall end with an indication of the military security classification of the information in the paragraph, represented as (TS), (S), (C), or (U).

There is no limitation on the length of the abstract. However, the suggested length is from 150 to 225 words.

14. **KEY WORDS:** Key words are technically meaningful terms or short phrases that characterize a report and may be used as index entries for cataloging the report. Key words must be selected so that no security classification is required. Identifiers, such as equipment model designation, trade name, military project code name, geographic location, may be used as key words but will be followed by an indication of technical content. The assignment of links, rules, and weights is optional.